A LEGENDRE SPECTRAL ELEMENT METHOD FOR SIMULATION OF INCOMPRESSIBLE UNSTEADY VISCOUS FREE-SURFACE FLOWS

by

Lee-Wing Ho

S.B.M.E. Massachusetts Institute of Technology (1976)
S.M.M.E. Massachusetts Institute of Technology (1978)
M. Engr. Massachusetts Institute of Technology (1981)

SUBMITTED TO THE DEPARTMENT OF MECHANICAL ENGINEERING
IN PARTIAL FULFILLMENT OF THE REQUIREMENTS
FOR THE DEGREE OF

Doctor of Philosophy
at the
Massachusetts Institute of Technology

June 1989

Signature of Author _____
Department of Mechanical Engineering
May 18, 1989

Certified by _____
Professor Anthony T. Patera
Thesis Supervisor

Accepted by _____
Professor Ain A. Sonin
Chairman, Department Committee on Graduate Studies

A LEGENDRE SPECTRAL ELEMENT METHOD FOR SIMULATION OF INCOMPRESSIBLE UNSTEADY VISCOUS FREE-SURFACE FLOWS

by

Lee-Wing Ho

Submitted to the Department of Mechanical Engineering
in partial fulfillment for the requirements for the degree of
Doctor of Philosophy

ABSTRACT

Many fluid flow problems of fundamental and practical importance involve free surfaces, multi-fluid layers, fronts, and moving boundaries. In this study, a new Legendre spectral element method is presented for the solution of the time-dependent Navier-Stokes equations in domains defined by moving or free boundaries. For purposes of analysis and clarity of presentation, attention is focused on the problem of unsteady flow of a thin film down an inclined plane.

Spectral element methods are high-order weighted residual techniques which combine the rapid convergence rate of spectral techniques with the geometric flexibility of finite element methods. In the spectral element discretization, the computational domain is subdivided into macro-elements, and the dependent and independent variables are approximated by high-order tensor-product polynomial expansions within the subdomains. Variational projection operators and Gauss numerical quadrature are used to generate the discrete equations, which are efficiently solved by iterative procedures based on tensor-product sum-factorization techniques. The Legendre free-surface spectral element formulation is based on the following extensions of the fixed-domain spectral element method: the use of the full viscous stress tensor for natural imposition of traction and surface tension boundary conditions; the use of arbitrary-Lagrangian-Eulerian methods for accurate representation of moving boundaries and fronts; the use of elliptic mesh-velocity solvers to accomodate large domain deformations; and the use of a semi-implicit time-stepping procedure to partially decouple the free-surface evolution and interior Navier-Stokes equations. An analysis of the spectrum of the linear stability problem (Orr-Sommerfeld equation) associated with film flow reveals the presence of dissipative, oscillatory, and weakly unstable shear modes, and suggests optimal semi-implicit schemes for temporal

discretization of the spectral element equations.

Detailed results are presented for the linear and nonlinear stability of film flows. Comparison of direct simulation results for linear growth rate with the (exact) predictions of the Orr-Sommerfeld operator demonstrate that the effect of the free surface is properly accounted for in the spectral element treatment. The numerical prediction of finite-amplitude flows shows both qualitative and quantitative agreement with the experimental results.

The results presented for film flow are representative of other calculations possible with the spectral element free-surface formulation, such as the simulation of solidification fronts, multi-layer fluids and flows bounded by pulsating walls. Examples are presented to demonstrate the effectiveness of the method in some of these applications.

Thesis Supervisors: Professor Anthony T. Patera
Thesis Committee: Professor Robert Brown
Professor Roger Kamm
Professor Borivoje Mikić

ACKNOWLEDGEMENTS

I would like to express my deep gratitude towards my thesis supervisor, Professor Anthony T. Patera, for his inspiration, guidance and encouragement which he generously provided throughout the research. He is also responsible for making the research work very much enjoyable. I would like to thank members of my thesis committee, Professor Robert Brown, Professor Roger Kamm and Professor Borivoje Mikić, for their enthusiasm and their many helpful suggestions on this work.

I am indebted to Dr. Einar Rønquist for his help and collaboration in many aspects of the research. I would like to thank the other members of our research group, and in particular, Dr. Edward Bullister, Dr. Paul Fischer, Dr. Hamdi Kozlu and Dr. Cathy Mavriplis, for their collaboration and encouragement.

I am indebted to my parents for their continuous encouragement throughout my study. I am especially grateful to my wife Ivy, who supported my return to school with patience and understanding.

TABLE OF CONTENTS

CHAPTER 1

INTRODUCTION

Fluid flows in time-dependent deforming geometries are encountered in a large number of important engineering and natural systems. In these problems, the time dependence of the geometry is most often due to the presence of one or more dynamic boundaries, such as solid-liquid, liquid-liquid and liquid-gas interfaces, in the systems. Examples of practical applications in which moving boundaries are important include : heat exchangers, in which fluid-structure interactions and resonances are critical to system performance; ship hydrodynamics, in which (viscous and inviscid) free-surface phenomena determine overall drag and stability characteristics; materials processing systems such as coating and crsytal growth processes, in which free surfaces and solidification fronts play a central role in flow evolution; and biological flows in living organisms, in which time-dependent geometries that arise from flexible and pulsating walls play a vital role in the cardiovascular, respiratory and renal systems. Free-surface and moving boundary flows are also crucial in understanding fundamental aspects of multi-phase flow, change-of-phase heat transfer, cavitation, dynamics of bubbles and droplets, etc.

As the motion of a boundary significantly complicates the already intractable Navier-Stokes equations, analytical solution of moving boundary flows in practice is extremely difficult (if not virtually impossible), and these problems are typically treated either experimentally or numerically. The main objective of this study is to formulate a numerical method for the solution of moving boundary fluid-flow problems, a solution technique in which adequate modelling capabilities are properly formulated to address the complexity due to moving boundaries; and at the same time, fast and versatile algorithms are employed for the efficient computation of the

solution. Such a numerical method could serve as an effective tool for analysts and engineers to obtain accurate solution for various classes of moving boundary problems. For purposes of analysis and clarity of presentation, we focus our attention in the current study on free-surface flows.

In the past, a number of numerical methods have been proposed for the solution of free-surface problems. These methods can be categorized as regards to the treatment of the free surface, the discretization in space and in time, and finally the solution algorithms employed. We briefly discuss each of these in turn. First, as regards treatment of the free surface, the various methods can be classified as [1] : front-tracking techniques in which the computational domain (mesh) deforms in accordance with the time-evolution of the free surface; front-fixing techniques in which the computational domain is fixed, and the time-evolution of the free surface is incorporated via a time-dependent transformation between the mesh coordinates and the physical coordinates; and fixed-domain techniques in which the computational domain remains fixed, and the free-surface position is determined by a mesh-defined variable or by a supplementary integral equation. The front-tracking and front-fixing methods are, in fact, closely related; however, the former tends to involve local mappings and allows "non-single-valued profiles", whereas the latter is often based on global mappings that may require single-valueness.

The front-tracking approach appears to be the most attractive for not-too-convoluted free-surface problems, as the position of the interface can be determined to a high accuracy, and the geometry of the computational domain can be updated more naturally than the transformation relations required in the front-fixing approach. Among the formulations employed by front-tracking techniques, the purely Lagrangian description suffers, in general, from excessive mesh distortion in requir-

ing mesh points to follow the motion of the corresponding fluid particles; therefore, such techniques are not effective without additional rezoning operations which reduce the mesh distortion. Arbitrary-Lagrangian-Eulerian descriptions [2],[3],[4],[5] have been proposed to alleviate such a difficulty. Using the concept that the computational domain can deform independently of the fluid motion (that is, the mesh velocity is independent of the fluid velocity except at moving boundaries where appropriate kinematic conditions are applicable), arbitrary-Lagrangian-Eulerian descriptions combine both advantages of accurate free-surface tracking and acceptable mesh "convection". In the current study, our formulation is based on a new arbitrary-Lagrangian-Eulerian technique which, when combined with appropriate mesh-velocity kinematic conditions, result in minimal mesh convolution. Consequently, rezoning operations are not necessary in most of the applications.

As regards to spatial discretizations, various techniques such as finite difference methods [2],[6] finite element methods [7],[8] and boundary element methods [9] have been employed for the solution of free-surface flows. In this study, a new Legendre spectral element method, which is an extension of the method described in Ref.[10] and [11] for fixed domains, is proposed for the spatial discretization of the free-surface Navier-Stokes equations. The spectral element method [12] is a high-order finite element method (which is similar to the p-type finite element method [13],[14]) that combines the geometric flexibility of finite element methods (h-type) with the rapid convergence of spectral techniques. Previous investigations have shown that due to their nondispersive behavior and the fast convergence obtained for smooth solution, these methods are capable of accurate and efficient solution of a wide range of fluid flow and heat transfer problems [15],[16],[17],[18],[19]. In addition to the flexibility provided by spectral element method in terms of either h- or p-refinement, recent advances in adaptive techniques and non-conforming dis-

cretization methodology [20] (in which h-type and p-type elements with different orders of approximation can be joined compatibly in the same mesh) greatly enhance the versatility of the method. The selection of the spectral element method for spatial discretization is motivated by the desire to exploit the above advantages. We shall demonstrate below that spectral element discretization is indeed effective as long as proper care is taken in the formulation of the variational statement as regards the arbitrary-Lagrangian-Eulerian terms and the stress tensor.

The issues of temporal treatment and solution algorithm are clearly closely coupled. In particular, a method is characterized both by the choice of an implicit, semi-implicit, or fully explicit time-marching scheme, and by the "subsequent" choice of associated linear solver within the timestep. As regards the choice of time-marching scheme, it is clear that fully implicit methods (and closely related steady solvers) have the advantages of being accuracy- rather than stability-limited; the associated disadvantage is the necessity of a nonlinear solver, and perhaps worse, the appearance of nonsymmetric and anisotropic matrix operators that typically necessitate memory- and cycle-intensive direct solvers. In contrast, explicit-in-time solvers can be severely restricted by stability restrictions, however the linear equations to be solved in this case reduce to symmetric elliptic systems (for the pressure) which can be readily treated with fast iterative solvers. Semi-implicit schemes constitute a compromise between the implicit-in-time coupled with direct-solver and explicit-in-time coupled with fast-iterative-solver schemes, in which those components of the equations (that is, the Stokes problem) amenable to fast iterative solution are treated implicitly, and those components of the equations (that is, nonsymmetric, nonlinear, and implicitly coupled terms) not readily amenable to fast iterative solution are treated explicitly. Although semi-implicit procedures are clearly best suited for time-dependent problems, they are also appropriate (par-

ticularly in three space dimensions) for steady-state calculations. The free-surface semi-implicit procedures adopted here represent extensions of earlier fixed-domain semi-implicit techniques; efficient treatment of free-surface problems requires the development of maximally stable/accurate semi-implicit time-stepping schemes for the kinematic conditions, and accurate prediction of the "free-surface" critical time step.

In the present study of free-surface flows we focus our attention primarily on the numerical solution of the classical falling film problem even though the proposed free-surface spectral element solution method is entirely generic. The thin film problem is of interest both as an "unsolved" physical problem, and as a convenient vehicle for describing and illustrating our general numerical techniques. Although the emphasis in the current study is clearly on numerical issues, it is not possible to develop efficient, accurate, and stable numerical techniques for free-surface flows without due consideration of the underlying physics and mathematics (that is, spectrum). The extent to which the film flow problem and associated analysis is "generic" is demonstrated in latter chapters of this thesis by the presentation of solutions to a variety of free-surface and moving boundary problems.

The outline of this thesis is as follows. In Chapter 2, we introduce the problem of film flow down an inclined plane. We present a temporal linearized stability analysis of the falling film problem and in addition, we briefly describe the dynamics of nonlinear film flows. Next, we present in Chapter 3 the variational formulation for unsteady free-surface flows using an arbitrary-Lagrangian-Eulerian description; the resulting variational statements constitute the basis for both spatial and temporal discretization. In Chapter 4, we present the spatial discretization of the (variational) Navier-Stokes equations in a deformable domain using the Legen-

dre spectral element method. Next, in Chapter 5 we present the selection, analysis and application of optimal semi-implicit time-integration schemes for temporal discretization. At the end of the chapter, the fully discrete algebraic time-evolution equations governing free-surface flows are given. The solution of the fully discrete equations using fast iterative solvers is the subject of Chapter 6. Next, in Chapter 7 we present the spectral element solutions to the film flow stability problem for both infinitesimal and finite perturbations, and we give comparison with previous numerical and experimental investigations. Several other free-surface flow calculations are also presented in this chapter. In Chapter 8, we discuss briefly the application of the proposed free-surface spectral element method to two different classes of moving boundary problems. Sample analyses for each of these categories are also presented to demonstrate the effectiveness and generality of the proposed method. In the final chapter, we present the conclusions of the study and suggest several areas which merit future investigations.

CHAPTER 2

FLOW OF A THIN FILM DOWN AN INCLINED PLANE

In this chapter we present the analysis of the flow of a thin film down an inclined plane. The study of this problem is motivated by the following considerations: (i) this is geometrically the simplest problem that embodies a free surface; (ii) it is of significant interests in practical applications such as coating processes; (iii) the associated linearized stability analysis (Orr-Sommerfeld operator) of this problem provides information about the relationship between the flow parameters and the eigenvalue spectrum, from which optimal time-integration schemes for direct simulation can be selected and analysed (see Chapter 5); and (iv) the quantitative solution of the problem serves as a basis for comparison regarding accuracy, effectiveness and generality among various solution methods.

2.1 Problem Description

The film-flow problem under consideration is shown in Fig. 2-1(a). A two-dimensional liquid film flows down a plane (stationary wall) inclined at an angle β with respect to the horizontal under the action of gravity. The liquid is characterized by a constant density ρ, kinematic viscosity ν, and surface tension σ. The film is assumed to be unbounded in the streamwise direction (x_1), and of average thickness h in the cross-stream (x_2) direction. Scaling length by h, velocity by U_0, where $U_0 = gh^2/2\nu$ (g is the acceleration of gravity), time by h/U_0, and pressure by ρU_0^2, the governing equations describing the film flow are the Navier-Stokes equations :

$$u_{i,t} + u_j\, u_{i,j} = -p_{,i} + \frac{1}{R}\,(\,u_{i,jj} + 2\,e_i\,) \qquad \text{in } \Omega(t)\ , \qquad (2.1a)$$

and the continuity equation :

$$u_{l,l} = 0 \qquad \text{in } \Omega(t)\ , \qquad (2.1b)$$

where $u_i(x_j,t)$ is the velocity component in the x_i-direction, $e_i = (sin\beta, cos\beta)$; $p(x_i,t)$ is the pressure, t is time, R is the Reynolds number, $R = U_0 h/\nu$ and $\Omega(t)$ is the time-dependent flow domain. We use indical notation, in which a subscript comma denotes derivative, (e.g., $u_{i,t} = \partial u_i/\partial t$, $u_{i,j} = \partial u_i/\partial x_j$), and repeated indices indicate summation, (e.g., $u_{l,l} = u_{1,1} + u_{2,2}$). We note that all quantities in Eq.(2.1) are nondimensional.

In anticipation of a temporal stability analysis in which disturbance of a given (nondimensional) wavelength λ is imposed, we consider a flow domain of length λ in the streamwise direction and a domain boundary which consists of the following subsets : $\partial\Omega(t) = \partial\Omega_p \cup \partial\Omega_u \cup \partial\Omega_\sigma(t)$, as shown in Fig. 2-1(b). The appropriate boundary conditions are : (i) periodic boundary conditions on $\partial\Omega_p$

$$u_i(0,x_2,t) = u_i(\frac{2\pi}{\alpha},x_2,t)\ , \qquad (2.2a)$$

$$p(0,x_2,t) = p\,(\frac{2\pi}{\alpha},x_2,t)\ , \qquad (2.2b)$$

where $\alpha = 2\pi/\lambda$; (ii) no-slip boundary conditions on the wall $\partial\Omega_u$

$$u_i = 0\,; \qquad (2.3)$$

and (iii) surface-tension traction boundary conditions on th urface $\partial\Omega_\sigma(t)$

$$s_i\,[\,-p\delta_{ij} + \frac{1}{R}(\,u_{i,j} + u_{j,i}\,)\,]\,n_j = 0 \qquad (2.4a)$$

$$n_i\,[\,-p\delta_{ij} + \frac{1}{R}(\,u_{i,j} + u_{j,i}\,)\,]\,n_j = W\,\kappa\,. \qquad (2.4b)$$

In Eq.(2.4), δ_{ij} is the Kronecker delta, n_i and s_i are the unit normal and tangent vectors, respectively, κ is the curvature, W is the Weber number, $W = \sigma/\rho h U_0^2$. In summary, the film flow characteristics are determined by the nondimensional parameters α, β, R and W.

2.2 Brief Summary of Film-Flow Dynamics

2.2.1 Mean Flow

The steady-state solution for the film flow problem is first given by Nusselt [21] which corresponds to the case of a perfectly flat free surface for which the streamwise velocity profile is semi-parabolic :

$$\overline{U}_1 = (1 - x_2^2)\, sin\beta\,, \tag{2.5a}$$

$$\overline{U}_2 = 0\,, \tag{2.5b}$$

$$\overline{P} = \frac{2}{R}\, x_2\, cos\beta\,. \tag{2.5c}$$

$$\overline{\eta} = 0\,. \tag{2.5d}$$

Even though the steady-state solution satisfies both the Navier-Stokes equations and the continuity equation (together with all associated boundary conditions), this solution is not always physically realizable since it may be unstable under certain flow conditions. Thus, stability analysis is required to characterize the nature of the actual flow. There are two distinct "mechanisms" of instability based on linearized stability analysis of the film flow problem; the occurrence of the corresponding mode of instability depends on the angle of inclination [22]. For nearly vertical films, weakly unstable gravity-capillary waves occur at relatively low Reynolds numbers

($O(1)$) for disturbances of relatively long wavelengths. For nearly horizontal films, Tollmien-Schlichting (shear) waves associated with relatively small wavelengths occur at much higher Reynolds numbers ($O(10^3)$). In the present study, we focus our attention on the first type of instability; namely, the case of vertically falling films. In the next sections, we present the linearized stability analysis together with a brief qualitative discussion on the nonlinear film characteristics.

2.2.2 Linearized Stability Analysis

Many analytical and experimental studies have been performed on the linearized stability analysis associated with film flow down an inclined plane; see Ref. [23] to [32]. We refer to Ref.[22] and [29] for a more comprehensive review of the literature. In the temporal linearized stability analysis, the mean flow given in Eq.(2.5a-c) is perturbed with an infinitesimal disturbance of the form :

$$u_i(x_1, x_2, t) = U_i(x_2) + \epsilon \hat{u}_i(x_2) e^{i\alpha x_1} e^{\gamma t} , \tag{2.6a}$$

$$p(x_1, x_2, t) = \bar{P}(x_2) + \epsilon \hat{p}(x_2) e^{i\alpha x_1} e^{\gamma t} ; \tag{2.6b}$$

similarly, the free-surface perturbation is given by

$$\eta(x_1, t) = \epsilon \hat{\eta} e^{i\alpha x_1} e^{\gamma t} , \tag{2.7}$$

where $\epsilon \ll 1$ and γ is the complex frequency. We remark that the above perturbation corresponds to a Fourier decomposition of the solution using separation of variables [33].

Substituting Eq.(2.6) into Eq.(2.1), retaining terms that are $O(\epsilon)$ and eliminating $\hat{p}$ and $\hat{u}_1$, we arrive at the Orr-Sommerfeld equation which is expressed in

terms of the cross-stream velocity $\hat{u}_2$ and the complex frequency λ :

$$\{(D^2-\alpha^2)^2 - i\alpha R[\overline{U}_1(D^2-\alpha^2) - D^2\overline{U}_1]\}\hat{u}_2 = \gamma R(D^2-\alpha^2)\hat{u}_2 \quad \text{in } \Lambda\ , \quad (2.8)$$

where D denotes d/dy and Λ=]0,1[. The following boundary conditions are applicable in conjunction with Eq.(2.8). At the wall, the no-slip condition is

$$\hat{u}_2(1) = D\hat{u}_2(1) = 0\ ; \quad (2.9)$$

and, at the free surface, the zero-shear boundary condition is

$$D^2\hat{u}_2(0) + \alpha^2\hat{u}_2(0) - i\alpha D^2\overline{U}_1(0)\hat{\eta} = 0\ , \quad (2.10a)$$

and the normal-traction bounadary condition is

$$D^3\hat{u}_2(0) - [i\alpha R\overline{U}_1(0) + 3\alpha^2 + \gamma R]D\hat{u}_2(0) = -(2\alpha^2 cos\beta + \alpha^4 WR)\hat{\eta}\ . \quad (2.10b)$$

Finally, the kinematic condition for the free surface is

$$\hat{u}_2(0) - i\alpha\overline{U}_1(0)\hat{\eta} = \gamma\hat{\eta}\ . \quad (2.11)$$

We remark here that the solution of the Orr-Sommerfeld equation is useful to verify the spectral element (direct simulation) calculations of the growth rate and wave speed for various combinations of flow parameters (see Chapter 7). In addition, a more in-depth understanding of the flow characteristics can be obtained by exploring the underlying mathematical structure (that is, spectrum) of the Orr-Sommerfeld operator, which is important in the temporal discretization of the governing equations used in direct simulation (see Chapter 5). For the solution of the Orr-Sommerfeld equation, we follow the approach given in the work by Kozlu and Patera [34]. First, we formulate an equivalent variational (weak) form of the Orr-Sommerfeld operator given in Eq.(2.8), together with the natural boundary

conditions given in Eq.(2.10). Next, we perform a finite-element discretization by subdividing the domain Λ into elements of equal length Δx_2. For each element, we select Hermit cubics as elemental interpolants for both the solution and the test function. The elemental coefficient matrices are then calculated using numerical integration, and we perform a direct stiffness summation operation, augmenting the resulting matrix equation with the kinematic condition given in Eq.(2.11), to arrive at the global discrete system of equations. This takes the form of an algebraic eigenvalue problem in which the eigenvalue γ and the eigenvector which consists of the nodal degrees-of-freedom for $\hat{u}_2$, $D\hat{u}_2$ and $\hat{\eta}$ are the solution sought (we actually need to compute only γ). We express the complex eigenvalue as $\gamma = \gamma_r + i\gamma_i$ where γ_r and γ_i are real. The stability of the film flow can now be determined from the eigenvalue which has the largest real part which we denote as γ_r^* ; namely,

$$\gamma_r^* \equiv (\gamma_r)_{max} \begin{cases} < 0 & \text{stable} \\ = 0 & \text{neutrally stable} \\ > 0 & \text{unstable} \end{cases} \tag{2.12}$$

We remark that the growth/decay rate of the disturbance is given by the maginutude of γ_r^*. We show in Fig. 2-2 and 2-3, as representative solutions for linearized stability analysis of vertically falling films, the growth/decay rate γ_r^* versus the wave number for various Reynolds and Weber numbers. We note from Fig. 2-2 that in the case of an unstable (growing) disturbance, the growth rate at fixed wave number and Weber number increases with increasing Reynolds number. This suggests that the instability is due to inertia effect. Moreover, the cut-off wave number is insensitive to the Reynolds number, which suggests that this cut-off phenomenon is of vortical rather than viscous nature. In Fig. 2-3, we observe that the growth rate at fixed wave number and Reynolds number decreases with increasing Weber number, which suggests that surface tension has a stabilizing effect on the instability. These

results agree closedly with those reported in earlier works [29].

2.2.3 Nonlinear Film Dynamics

Owing to the complexity associated with nonlinear stability analysis, the film flow characteristics associated with finite-amplitude perturbation are first established mainly from experimental work. In the case of vertically falling films with disturbance of relatively short wavelength, the unstable mode will continue to grow until the flow becomes turbulent [22],[35],[36],[37]. However, for fluids with relatively strong surface tension and for disturbance of sufficiently long wavelengths, the unstable (growing) mode predicted by linearized theory is stabilized by nonlinear effects as observed in the experimental investigations performed by Kapitza [38]. In this case, the flow remains laminar as the disturbance evolves and increases in amplitude until finally, a steady-periodic state is reached. Two types of supercritically stable steady-periodic finite-amplitude waves associated with vertical film flows are reported by Kapitza. The first type takes the form of periodic ripples, see Fig. 2-4, and can be generated experimentally by disturbing the falling film with weak periodic air pulses. For this type of ripples, the film profile is completely regular and, at small flowrates, resembles a sinusoid. At larger flowrates, however, the superposition of higher harmonics can be observed as the ripples becomes steepened at the front. The second type of supercritically stable finite-amplitude waves (termed single wave by Kaptiza) are of even longer wavelengths and the wave profile resembles a train of non-interacting "droplets", see Fig. 2-5. This type of waves can be generated experimentally by using stronger air pulses applied at longer periodic intervals. We observe that in this case the film profile is more irregular and consists of a dominant crest with a steepened front, which is preceeded by a

number "dimples" that are progressively smaller the further they are ahead of the single crest, and a essentially flat region behind the dominant crest and ahead of the smallest dimple. Additional experimental studies of the wave profiles and the velocity distributions of these two types of nonlinear waves are given in Ref.[45].

There exist a number of analytical studies on finite-amplitude waves in falling films. Atherton et.al. [39] derived the general evolution equations for both planar and axisymmetric films. For the periodic waves, Lin [42],[43], Nakaya [40], Gjevik [41] investigated the existence of supercritically stable states based on various simplified models, and evaluated the wave amplitude as a function of various flow parameters. In Ref.[41] and [44], the authors used a one-dimensional series expansion approach and computed the wave speeds of the periodic ripples; the periodic wave profiles were also plotted. For the single-waves, Tsvelodub et.al. [46] and Demekhlin et.al. [47] computed (stationary) wave profiles for vertically falling films; Demekhlin et.al. also presented incomplete plots of stationary streamlines evaluated from matching different solitary-wave solutions.

With regards to the goal that we set forth for the study of the film-flow problem, the numerical simulations of both of these two types of nonlinear waves using the proposed spectral element scheme are particularly important, both in providing quantitative solutions (which are highly nontrivial) to the nonlinear problem, and in demonstrating the effectiveness of the solution capability of the proposed scheme for free-surface flows. The presentation of the spectral element results and comparison with the available solutions are given in Chapter 7.

CHAPTER 3

VARIATIONAL FORMULATION USING ARBITRARY-LAGRANGIAN-EULERIAN DESCRIPTION

The variational statement which constitute the basis for spatial and temporal discretization is formulated in this chapter. For completeness we present in Section 3.1 the incompressible Navier-Stokes equations (the strong form) for free-surface flows. Next, the variational (weak) form is presented in Section 3.2. The manipulations which remove the ambiguity of reference configuration in the unsteady term of the weak form are given in detail. The role and the determination of the mesh velocity which is a key ingredient in the arbitrary-Lagrangian-Eulerian technique are also discussed.

3.1 Navier-Stokes Equations

The governing equations for incompressible free-surface flow are the Navier-Stokes and the continuity equations which can be expressed in the following strong form :

$$\rho \left(u_{i,t} + u_j \, u_{i,j} \right) = \tau_{ij,j} + f_i \qquad in \ \Omega(t) \,, \tag{3.1a}$$

$$u_{l,l} = 0 \qquad in \ \Omega(t) \,; \tag{3.1b}$$

where τ_{ij} is the stress tensor, u_i is the velocity, f_i is the body force, ρ is the fluid density, and $\Omega(t)$ is the time-dependent domain. The notation for derivatives and the summation convention are the same as in Section 2.1. For a Newtonian fluid, the constitutive relation is given by

$$\tau_{ij} = -p \, \delta_{ij} + \mu \left(u_{i,j} + u_{j,i} \right) , \tag{3.2}$$

where δ_{ij} is the Kronecker delta, p is the pressure, and μ is the viscosity. We remark that in the consitutive relation given in Eq.(3.2), the full viscous stress tensor (rather than the usual Laplacian operator) is used in anticipation of the variational statement for which traction boundary conditions are to be imposed consistently at the free surface.

At the boundary where the fluid velocity is precribed, we have the following Dirichlet boundary condition :

$$u_i = \overline{u}_i \qquad \text{on } \partial\Omega_u(t) \; ; \tag{3.3}$$

where $\overline{u}_i$ is the prescribed velocity. At the boundary where traction is prescribed, we have the following Neumann boundary condition :

$$\tau_{ij}\, n_j = \bar{t}_i \; , \qquad \text{on } \partial\Omega_\sigma(t) \; ; \tag{3.4}$$

where n_j is the outward unit normal vector on $\partial\Omega_\sigma(t)$ and $\bar{t}_i$ is the imposed traction. For free-surface problems, the traction boundary condition at the free surface is given by

$$\tau_{ij}\, n_j = \sigma\kappa n_i \; , \qquad \text{on } \partial\Omega_\sigma(t) \; ; \tag{3.5}$$

where σ is the surface tension and κ is the curvature of the free surface. In the following we shall assume, for simplicity of presentation, that the free surface is the only boundary on which traction conditions are imposed. We emphasize that the solutions for the free-surface flow problem are the velocity $u_i(x_k, t)$, the pressure $p(x_k, t)$, and the flow domain $\Omega(t)$.

3.2 Variational Formulation

The variational (weak) form can be derived from the strong form using the following procedures. Multiplying the momentum equations and the continuity equation by the test functions v_i and q, respectively, integrating the resulting equations over the domain and applying integration by parts to the momentum equations, we obtain the following equivalent variational statement : find the solution (u_i, p), $u_i \in \mathcal{H}_0^1[\Omega(t)]$ and $p \in \mathcal{L}^2[\Omega(t)]$, such that :

$$\int_{\Omega(t)} \{ \rho\, v_i\, (u_{i,t} + u_j\, u_{i,j}) \; + \; v_{i,j}\, [\, -p\delta_{ij} + \mu(u_{i,j} + u_{j,i})\,] \; - \; v_i\, f_i \}\, dV \; +$$

$$\int_{\partial\Omega_\sigma(t)} \sigma\kappa\, v_i\, n_i\, dA = 0 \qquad \forall v_i \in \mathcal{H}_0^1[\Omega(t)]\,, \quad (3.6a)$$

$$\int_{\Omega(t)} q\, u_{l,l}\, dV = 0 \qquad \forall q \in \mathcal{L}^2[\Omega(t)]\,; \quad (3.6b)$$

where $\mathcal{H}_0^1[\Omega(t)]$ and $\mathcal{L}^2[\Omega(t)]$ are the Sobolev spaces defined for the time-dependent domain $\Omega(t)$. We remark that $\mathcal{L}^2[\Omega(t)]$ is the space of all functions which are square integrable in $\Omega(t)$, and $\mathcal{H}_0^1[\Omega(t)]$ is the space of all functions which are square integrable, and whose first derivatives are also square integrable in $\Omega(t)$; and which satisfy the boundary conditions in Eq.(3.3) but not Eq.(3.5). We further note that in Eq.(3.6a), the boundary integral is introduced so that the inhomogeneous Neumann boundary condition given in Eq.(3.5) is satisfied in the natural (weak) sense.

Before we embark on the discretization of the above variational form, we anticipate that the unsteady term (the first term in Eq.(3.6a)) will give rise to ambiguity regarding the reference configuration when time differencing is being performed; that is,

$$u_{i,t} \cong \frac{u_i^{n+1} - u_i^n}{\Delta t} \; ;$$

where the subscripts (n+1) and n refer to the current time step and the previous time step, respectively. Thus, if Eq.(3.6a) is used directly for temporal discretization, the product "$v_i u_{i,t}$" in the integrand will give rise to contributions which are defined on different time configurations. In order to avoid this inconsistency which can lead to unduly large discretization error, it is imperative that the time derivative be moved outside the integral. This is achieved using the following procedures. First we perform integration by parts on the first term of Eq.(3.6a) to obtain

$$\int_{\Omega(t)} v_i \, u_{i,t} \, dV = \int_{\Omega(t)} [\, (v_i \, u_i)_{,t} - u_i \, v_{i,t} \,] \, dV \; . \tag{3.7}$$

The first term on the right hand side of Eq.(3.7) can now be rewritten using the Reynolds transport theorem and the divergence theorem as

$$\int_{\Omega(t)} (v_i \, u_i)_{,t} \, dV = \frac{d}{dt} \int_{\Omega(t)} v_i \, u_i \, dV - \int_{\Omega(t)} (v_i \, u_i \, w_j)_{,j} \, dV \; , \tag{3.8}$$

where w_j is some Lagrangian velocity which describes the motion of each material point in the domain $\Omega(t)$ and therefore defines the deformation of the domain. Note that w_j is in general independent of u_j and hence can be selected to minimize the domain deformation; this is the one of the major advantages of the arbitrary-Lagrangian-Eulerian description. In order to treat the last term on the right-hand-side of Eq.(3.7), we use the fact that the time derivative of the test function v_i following the motion of the material points (denoted as X_i) of the domain is zero; that is,

$$(\, dv_i/dt \,)\,|_{X_k} \; = \; v_{i,t} + w_j \, v_{i,j} \; = 0 \; .$$

Using the above equation, we can express the time derivative $v_{i,t}$ in terms of the

spatial derivative $v_{i,k}$ as

$$\int_{\Omega(t)} u_i \, v_{i,t} \, dV = - \int_{\Omega(t)} u_i \, v_{i,j} \, w_j \, dV \; . \tag{3.9}$$

Using Eq.(3.7) to (3.9), the final variational form that replaces Eq.(3.6a) as a basis for temporal and spatial discretizations takes the following form : find the solution (u_i, p), $u_i \in \mathcal{H}_0^1[\Omega(t)]$ and $p \in \mathcal{L}^2[\Omega(t)]$, such that

$$\begin{aligned} \frac{d}{dt} \int_{\Omega(t)} \rho \, v_i \, u_i \, dV \; = & \int_{\Omega(t)} \{ \, v_{i,j} \, \delta_{ij} \, p - \mu \, v_{i,j} \, (u_{i,j} + u_{j,i}) + v_i \, f_i - \\ & \qquad \rho \, [\, v_i \, u_j \, u_{i,j} - v_i \, (u_i \, w_j \,)_{,j} \,] \, \} \, dV \; + \\ & \int_{\partial \Omega_\sigma(t)} \sigma \, \kappa \, v_i \, n_i \, dA \qquad \forall v_i \in \mathcal{H}_0^1[\Omega(t)] \; . \end{aligned} \tag{3.10}$$

For two-dimensional planar geometry, the curvature that appears in the integrand of the surface-tension integral in Eq.(3.10) is given by

$$\kappa = s_{i,\zeta} \; ,$$

where s_i is the unit tangent vector , ζ is the curvilinear coordinate defined along the free-surface segment $\overline{ab}$, and $s_{i,\zeta} = \partial s_i / \partial \zeta$. The contact angles θ_a , θ_b at the end points "a" and "b" of the segment are assumed to be specified ; see Fig. 3-1. We next apply the treatment proposed by Ruschak [48] for the surface-tension integral given in Eq.(3.10) by first rewritting the integral as

$$\int_{\partial \Omega_\sigma(t)} \sigma \, \kappa \, v_i \, n_i \, dA = \int_a^b \sigma \, v_i \, s_{i,\zeta} \, d\zeta \; . \tag{3.11}$$

Upon integration by parts of the right hand side of Eq.(3.11) and noting that

$$v_{i,\zeta} \; = \; v_{i,j} \, s_j \; ,$$

the final form of the surface integral becomes

$$\int_{\partial\Omega_{e(t)}} \sigma \kappa v_i n_i \, dA = -\int_a^b \sigma v_{i,j} s_i s_j \, d\zeta + (\sigma v_i s_i)\Big|_a^b \ . \qquad (3.12)$$

We note that in the last term of Eq.(3.12), $s_i|_a$ and $s_i|_b$ are given by the specified contact angle between the free surface and the solid boundary at "a" and "b", respectively. In addition, for adjacent segments on the free surface, these boundary contributions impose, as a natural boundary condition, C^0 continuity of the slope of the segments at the adjoining points.

For axisymmetric geometry (see Fig. 3-2), similar procedures can be applied to obtain an equivalent form for the surface integral. We thus have

$$\int_{\partial\Omega_{e(t)}} \sigma \kappa v_i n_i \, dA = -\int_a^b \sigma (R v_i)_{,j} s_i s_j R \, d\zeta + (\sigma R v_i s_i)\Big|_a^b + \int_a^b \sigma v_i n_i n_2 \, d\zeta \ . \qquad (3.13)$$

We remark that in three-dimensional analysis, the above integration-by-parts procedure becomes nontrivial since the mean curvature at a point on the free surface will involve derivatives of the unit tangent vectors defining the tangent plane at that point. The use of an auxiliary variational statement to enforce C^0 continuity of the slope (in the weak sense) at interelmental boundaries will be the subject of future investigation.

At the free surface, the kinematic condition that no fluid particles can cross over the liquid-air interface [49] requires that on $\partial\Omega_e(t)$

$$w_i n_i = u_i n_i \ . \qquad (3.14a)$$

We note that by imposing the above kinematic condition, the position of the free surface can be tracked continuously in time via the time integration of the mesh velocity at the free surface. There are no kinemtic condition on $w_i s_i$; however, the

requirement that

$$w_i \, s_i = 0 \tag{3.14b}$$

will typically result in minimization of the domain deformation which is computationally advantageous. On the other boundaries that are fixed in time, we have

$$w_i = 0 \, . \tag{3.14c}$$

Once the mesh velocity on the entire boundary is determined, it can be extended into the interior domain using various techniques [50],[51]. One effective approach is the use of an elliptic operator $\mathcal{D}$ in the form

$$\mathcal{D} \, w_i = 0 \, ; \tag{3.15}$$

where Eq.(3.15) and (3.14) constitute an elliptic boundary value problem. We propose the use of second order elliptic operators such as the linear elastostatic operator (which is also used in ref. [51]) or the steady-Stokes operator for this extension procedure. The derivations for both of these operators are given in Chapters 4. Using the Lagrangian coordinate X_i which defines the location of the material points in the time-dependent domain $\Omega(t)$, we have the following kinematic conditions

$$X_{i,t} = w_i \, . \tag{3.16}$$

from which the time evolution of the domain geometry can be evaluated.

CHAPTER 4

SPATIAL DISCRETIZATION USING LEGENDRE SPECTRAL ELEMENTS

The numerical methods used in the treatment of the Navier-Stokes equations are premised on a layered approach, in which the discretizations and solvers are constructed on the basis of a hierarchy of nested operators : from the highest to the lowest spatial derivatives. For free-surface fluid flow problems, additional operations are required for the update of the geometry of the time-dependent domain. However, this can be considered as a zeroth order operator (no spatial derivatives are required) and, according to our construction, corresponds to the outermost layer. This approach is motivated by the fact that the highest derivatives govern the continuity requirement, conditioning and stability of the system; and, it is particularly well-suited to the viscous incompressible flow equations, in which the highest derivatives correspond to linear symmetric elliptic or saddle operators for which optimal discretizations and solvers are readily available.

Following this hierarchial construction, we first present in Section 3.1 the spectral element discretization for the innermost layer, the elliptic kernel, in order to illustrate the spectral element methodology. We consider a linear elastostatic problem as our elliptic kernel (which is of interest since it can be used according to Eq.(3.15) for the solution of the interior mesh velocity). This is followed by the steady-Stokes problem in Section 3.2 which corresponds to the next layer. The staggered mesh approach which is crucial in preventing spurious pressure modes is also introduced in this section. Lastly, in Section 3.3, we present the treatment of the remaining contributions in the unsteady free-surface Navier-Stokes equations that correspond to the outer layer. At the conclusion of this chapter, the semi-

discrete governing equations for incompressible viscous free-surface flows are given.

4.1 Basic Discretization

In order to illustrate the Legendre spectral method for spatial discretization of an elliptic problem, we consider a two-dimensional linear elastostatic problem. We note that this problem is analogous to the steady-Stokes problem except that in the elastostatic problem, the incompressibility constraint is relaxed, which leads to an elliptic rather than a saddle problem. Moreover, the treatment of the deviatoric stress contribution in the variational statements for the Navier-Stokes problem and the elastostatic problem is entirely analogous. We further remark that the extension of the mesh velocity to the interior as given by Eq.(3.15) can be performed effectively using the elastostatic operator.

The governing equation for the elastostatic problem defined in a fixed curvilinear domain Ω is

$$\tau_{ij,j} + f_i = 0 \qquad \text{in } \Omega\,, \tag{4.1}$$

where τ_{ij} is the stress tensor, f_i is the body force. We assume the following Dirichlet boundary conditions

$$u_i = \overline{u}_i \qquad \text{on } \partial\Omega\,, \tag{4.2}$$

where u_i is the displacement solution and $\overline{u}_i$ is the prescribed displacement. For a linear isotropic elastic material, the constitutive relation is given by

$$\tau_{ij} = \lambda_1\, \delta_{ij} u_{l,l} + \lambda_2 \left(u_{i,j} + u_{j,i} \right)\,, \tag{4.3}$$

where λ_1 and λ_2 are the elastic (Lamé) coefficients. The equivalent variational for-

mulation that corresponds to Eq.(4.1) to (4.3) is : find the solution $u_i \in \mathcal{H}_0^1(\Omega)$ such that

$$\int_\Omega v_{i,j} \left[\lambda_1 \delta_{ij} u_{l,l} + \lambda_2 (u_{i,j} + u_{j,i}) \right] dV = \int_\Omega v_i f_i \, dV \qquad \forall v_i \in \mathcal{H}_0^1(\Omega) , \quad (4.4)$$

where $\mathcal{H}_0^1(\Omega)$ is the Sobolev space defined for the fixed domain Ω. The above variational statement will serve as the basis for the spatial discretization given below.

We proceed with the spectral element discretization by subdividing the domain into K disjoint quadrilateral elements

$$\bar{\Omega} = \bigcup_{k=1}^{K} \bar{\Omega}_k , \quad (4.5)$$

such that the intersection of two adjoining elements is either a whole edge or a vertex. We shall require Eq.(4.4) to be satisfied for a piecewise-polynomial approximation space defined for the Ω_k. In order to facilitate the definition of this spectral element approximation space, we first define the space $\mathcal{P}_{N,K}$ as

$$\mathcal{P}_{N,K}(\Omega) = \{ \Phi \in \mathcal{L}^2(\Omega) ; \Phi|_{\Omega_k} \in \mathcal{P}_N(\Omega_k) \} , \quad (4.6)$$

where $\mathcal{P}_N(\Omega_k)$ denotes the tensor-product space of all polynomials of degree less than or equal to N with respect to the spatial coordinates. The spectral element approximation space $\mathcal{X}_k$ is then defined as

$$\mathcal{X}_k = \mathcal{H}_0^1(\Omega) \cap \mathcal{P}_{N,K}(\Omega) . \quad (4.7)$$

We remark that the use of variational formulation will result in C^1-continuity of the solution generated naturally (that is, in a weak sense) at the interelemental boundaries. Using the above approximation space, the elastostatic problem becomes : find the solution $(u_i)_k \in \mathcal{X}_k$ such that :

$$\sum_{k=1}^{K} \left[a_{1,h}^{k}(v_i, u_j) + a_{2,h}^{k}(v_i, u_j) \right] = \sum_{k=1}^{K} (v_i, f_i)_h^k \qquad \forall v_i \in \mathcal{X}_h \; ; \qquad (4.8)$$

where

$$a_{1,h}^{k}(v_i, u_j) = \int_{\Omega_k} \lambda_1 \, v_{i,j} \delta_{ij} (u_{l,l})_h \, dV \; , \qquad (4.9a)$$

$$a_{2,h}^{k}(v_i, u_j) = \int_{\Omega_k} \lambda_2 \, v_{i,j} \left[(u_{i,j})_h + (u_{j,i})_h \right] dV \; , \qquad (4.9b)$$

$$(v_i, f_i)^k = \int_{\Omega_k} v_i \, f_i \, dV \; . \qquad (4.9c)$$

The evaluation of the elemental integrals given in Eq.(4.9) for general curvilinear elements is facilitated by a mapping of the physical (x_1, x_2)-system into a local (r,s)-system, see Fig. 4-1 ; this mapping is given by

$$(x_1 \, , \, x_2)^k \in \Omega_k \Rightarrow (r \, , \, s) \in \Lambda \times \Lambda \; ; \qquad \Lambda =]-1, 1[\; . \qquad (4.10)$$

The derivatives in the elemental integrals can be expressed in tems of the local r,s coordinates using the following Jacobian transformation

$$\frac{\partial}{\partial x_i} = J_{i\alpha}^{-1} \frac{\partial}{\partial r_\alpha} \; , \qquad (4.11)$$

where summation is performed for α=1,2; $r_1 \equiv r$, $r_2 \equiv s$; and the Jacobian, its inverse and its determinant are given by

$$J = \begin{bmatrix} x_{1,r} & x_{2,r} \\ x_{1,s} & x_{2,s} \end{bmatrix} \; , \qquad (4.12a)$$

$$J^{-1} = \frac{1}{|J|} \begin{bmatrix} x_{2,s} & -x_{2,r} \\ -x_{1,s} & x_{1,r} \end{bmatrix} \; , \qquad (4.12b)$$

$$|J| = x_{1,r} x_{2,s} - x_{2,r} x_{1,s} \; . \qquad (4.12c)$$

Using Eq.(4.11), the elemental integrals given in Eq.(4.9) can be rewritten as

$$a^k_{1,h}(v_i,u_j) = \int_{-1}^{1}\int_{-1}^{1} \lambda_1\, v^k_{i,\alpha}\,(J^{-1}_{j\alpha})^k\,\delta_{ij}\,(u_{l,\alpha})^k_h\,(J^{-1}_{l\alpha})^k\,|J|^k\,drds\,, \tag{4.13a}$$

$$a^k_{2,h}(v_i,u_j) = \int_{-1}^{1}\int_{-1}^{1} \lambda_2\, v^k_{i,\alpha}(J^{-1}_{j\alpha})^k[(u_{i,\alpha})^k_h(J^{-1}_{j\alpha})^k + (u_{j,\alpha})^k_h(J^{-1}_{i\alpha})^k]|J|^k drds\,, \tag{4.13b}$$

$$(v_i,f_i)^k_h = \int_{-1}^{1}\int_{-1}^{1} v^k_i\, f^k_i\,|J|^k\,drds\,. \tag{4.13c}$$

The numerical evaluation of these integrals is performed by employing tensor product of the Gauss-Lobatto formulas as the integration rule, for which the local Gauss-Lobatto points and weights [52] are denoted as (ξ_m,γ_m). The resulting integration rule is :

$$\int_{\Omega_k} g\,dV\,\Big|_{GL} \;=\; \gamma_m\gamma_n\,|J^k(\xi_m,\xi_n)|\,g^k(\xi_m,\xi_n) \qquad \forall g^k \in C^0(\bar{\Omega}_k)\,, \tag{4.14}$$

where summation is performed for m,n=0,1,...,N. We remark that the (N+1)-point Gauss-Lobatto quardrature integrates exactly polynomials of degree (2N-1) or less. Using the Gauss-Lobatto formulas and Eq.(4.14), the integrals given in Eq.(4.13) become

$$\begin{aligned} a^k_{1,h-GL}(v_i,u_j) \;=\; & \gamma_m\gamma_n\,|J^k(\xi_m,\xi_n)|\;\; \lambda_1\, v^k_{i,\alpha}(\xi_m,\xi_n)\,[J^{-1}_{j\alpha}(\xi_m,\xi_n)]^k \\ & \delta_{ij}\,[u_{l,\alpha}(\xi_m,\xi_n)]^k_h\,[J^{-1}_{l\alpha}(\xi_m,\xi_n)]^k\,, \end{aligned} \tag{4.15a}$$

$$\begin{aligned} a^k_{2,h-GL}(v_i,u_j) \;=\; & \gamma_m\gamma_n\,|J^k(\xi_m,\xi_n)|\;\; \lambda_2\, v^k_{i,\alpha}(\xi_m,\xi_n)\,[J^{-1}_{j\alpha}(\xi_m,\xi_n)]^k \\ & \{\,[u_{i,\alpha}(\xi_m,\xi_n)]^k_h\,[J^{-1}_{j\alpha}(\xi_m,\xi_n)]^k \;+ \\ & [u_{j,\alpha}(\xi_m,\xi_n)]^k_h\,[J^{-1}_{i\alpha}(\xi_m,\xi_n)]^k\,\}\,, \end{aligned} \tag{4.15b}$$

$$(v_i,f_i)^k_{h-GL} \;=\; \gamma_m\gamma_n\,|J^k(\xi_m,\xi_n)|\;\; f^k_i(\xi_m,\xi_n)\,v^k_i(\xi_m,\xi_n)\,; \tag{4.15c}$$

where summation is performed for m=0,1,...,N and α=1,2.

We now introduce an interpolant Gauss-Lobatto-Legendre basis for the spectral element approximation space X_h defined in Eq.(4.7). The mapping given in Eq.(4.10) can be expressed in terms of the following tensor-product form

$$(x_i)^k(r,s) = (x_i)^k_{pq}\, h_p(r) h_q(s) \,, \tag{4.16}$$

where $(x_i)^k_{pq}$ is the physical x_i-coordinate of local collocation point (p,q) of element k, $h_p(z)$ is the Nth order elemental Lagrangian interpolant through the Gauss-Lobatto-Legendre points; that is

$$h_p(z_m) = \delta_{mp} \,, \tag{4.17}$$

and summation is performed for p,q=0,1,...,N. The local collocation points z_0, z_1, ..., z_N are given by [11]

$$\begin{aligned} z_0 &= -1 \,, \\ z_N &= 1 \,, \\ P_N'(z_m) &= 0 \qquad\qquad \text{for m=1,...,N-1 ;} \end{aligned}$$

where $P_N(z)$ is the Legendre polynomial of degree N and a prime denotes differentiation with respect to z. In addition, the nodal interpolant derivative operator, defined as [11]

$$D_{ij} = \frac{dh_j(z_i)}{dz} \,, \tag{4.18}$$

is given by

$$\begin{aligned} D_{00} &= -N(N+1)/4 \,; \\ D_{ii} &= 0 \,, \qquad\qquad \text{for i} \neq 0,\text{N ;} \end{aligned}$$

$$D_{NN} \;=\; N(N+1)/4\;;$$

$$D_{ij} \;=\; P_N(z_i)\,/\,[\,P_N(z_j)(z_i - z_j)\,]\;, \qquad \text{for i} \neq \text{j}.$$

Using the isoparametric approach, the solution u_i, the test function v_i, and the data f_i are expanded in the same manner as given in Eq.(4.16). Next, we proceed to treat the local-coordinate derivatives of the test function v_i and the solution u_i in Eq.(4.15). A typical derivative at a collocation point (m,n) can be expressed as

$$(v_{i,\alpha}\, J^{-1}_{j\alpha})^k_{mn} \;=\; (G_j)^k_{mnpq}\,(v_i)^k_{pq}\;; \tag{4.19}$$

where

$$(G_j)^k_{mnpq} \;=\; (J^{-1}_{j1})^k_{mn}\, D_{mp}\,\delta_{nq} \;+\; (J^{-1}_{j2})^k_{mn}\,\delta_{mp}\, D_{nq}\;, \tag{4.20}$$

$$(J^{-1}_{11})^k_{mn} \;=\; D_{nq}\,(x_2)^k_{mq}\;/\;|J|^k_{mn}\;, \tag{4.21a}$$

$$(J^{-1}_{12})^k_{mn} \;=\; -D_{mp}\,(x_2)^k_{pn}\;/\;|J|^k_{mn}\;, \tag{4.21b}$$

$$(J^{-1}_{21})^k_{mn} \;=\; -D_{nq}\,(x_1)^k_{mq}\;/\;|J|^k_{mn}\;, \tag{4.21c}$$

$$(J^{-1}_{22})^k_{mn} \;=\; D_{mp}\,(x_1)^k_{pn}\;/\;|J|^k_{mn}\;, \tag{4.21d}$$

and

$$|J|^k_{mn} \;=\; D_{mp}\,(x_1)^k_{pn}\, D_{nq}\,(x_2)^k_{mq} \;-\; D_{nq}\,(x_1)^k_{mq}\, D_{mp}\,(x_2)^k_{pn}\;, \tag{4.21e}$$

with no summation on the repeated indices "m" and "n" in Eq.(4.20) and (4.21). Using Eq.(4.19), the expressions given in Eq.(4.15) can be rewritten entirely in terms of nodal variables (at the collocation points) as

$$\begin{aligned} a^k_{1,h-GL}(v_i,u_j) \;=\; & \gamma_m\gamma_n\,|J|^k_{mn}\lambda_1\,(G_j)^k_{mnpq}\,(v_i)^k_{pq} \\ & \delta_{ij}\,(G_l)^k_{mnrs}\,(u_l)^k_{rs}\;, \end{aligned} \tag{4.22a}$$

$$a^k_{2,h-GL}(v_i,u_j) \;=\; \gamma_m\gamma_n\,|J|^k_{mn}\lambda_2\,(G_j)^k_{mnpq}\,(v_i)^k_{pq} \\ [\,(G_j)^k_{mnrs}\,(u_i)^k_{rs} \;+\; (G_i)^k_{mnrs}\,(u_j)^k_{rs}\,]\,, \qquad (4.22b)$$

$$(v_i,f_i)^k_{h-GL} \;=\; \gamma_m\gamma_n\,|J|^k_{mn}\,(f_i)^k_{mn}\,(v_i)^k_{mn}\,. \qquad (4.22c)$$

We remark here that the choice of the expansion in tensor-product form as given in Eq.(4.16) is advantageous since it permits the use of the tensor-product-sum-factorization techniques, which is discussed in more detail in Chapter 6. The final discrete algebraic system of equations are obtained by substituting Eq.(4.22) into the variational statement given in Eq.(4.8) and choosing the test function v_i successively to be unity at only one *global* collocation point, and zero at all other collocation points. The resulting global system of equilibrium equations are

$$\sum_{k=1}^{K}{}' \,(A^E_{ij})^k_{pqrs}\,(u_j)^k_{rs} \;=\; \sum_{k=1}^{K}{}' \,B^k_{pqrs}\,f^k_{rs}\;; \qquad (4.23)$$

where

$$(A^E_{ij})^k_{pqrs} \;=\; \gamma_m\gamma_n\,|J|^k_{mn}\,[\lambda_2\,\delta_{ij}\,(G_l)^k_{mnpq}\,(G_l)^k_{mnrs} \;+ \\ \lambda_1(G_i)^k_{mnpq}(G_j)^k_{mnrs} + \lambda_2(G_j)^k_{mnpq}(G_i)^k_{mnrs}]\,, \qquad (4.24a)$$

$$B^k_{pqrs} \;=\; \gamma_p\gamma_q\,|J|^k_{pq}\,\delta_{pr}\,\delta_{qs}\;; \qquad (4.24b)$$

and $\sum'$ denotes direct stiffness summation operation. A more convenient way to express the equilibrium equations is to rewrite Eq.(4.23) in matrix form

$$\mathbf{A}^E_{ij}\,\mathbf{U}_j \;=\; \mathbf{B}\,\mathbf{F}_i\,, \qquad (4.25)$$

where $\mathbf{A}^E_{ij}$ is the global stiffness matrix and $\mathbf{B}$ is the global mass matrix (without the factor of density) which, for the present Legendre spectral element formulation, is diagonal, and $\mathbf{U}_j$ and $\mathbf{F}_i$ store u_j and f_i, respectively, at all the collocation

points. We emphasize that the global matrix notation in Eq.(4.25) is used only as a convenient mean to describe the governing equations. In the actual solution using fast iterative solvers such as conjugate gradient iteration, the global matrices are never assembled; instead matrix-vector product is performed at the element level, see Chapter 6.

In applying the elastostatic solver to the extension of the mesh velocity w_i into the interior domain (see Eq.(3.15)), we substitute w_i for u_i and select f_i to be identically zero; and, on the boundary $\partial\Omega$, we employ w_i given in Eq.(3.14) for $\overline{u}_i$ in Eq.(4.2). It can be shown that the solution w_i will only depend on *one* material constant [53]. Thus, if we express λ_1 and λ_2 in terms of Young's modulus E and Poisson's ratio ν :

$$\lambda_1 = \frac{E\nu}{(1+\nu)(1-2\nu)} , \tag{4.26a}$$

$$\lambda_2 = \frac{E}{2(1+\nu)} ; \tag{4.26b}$$

where $0 \leq \nu < 0.5$, then the solution will depend only on ν. In the case of a nearly incompressible constitutive relation (i.e., $\nu \cong 0.5$), the stiffness matrix will become singular. Thus, if it is desired that the spectral elements maintain their original volume as they deform, then the incompressible steady Stokes solver described in the next section will be more appropriate for the extension operation.

4.2 Steady Stokes Problem

We present in this section the steady Stokes problem using the discretization procedure described in the last section. The key consideration for the steady Stokes problem is the use of different solution spaces for the velocity and the pressure

solutions in order to avoid spurious pressure modes that contaminate the solution. Another consideration is the use of the full viscous stress tensor for the consistent imposition of inhomogeneous Neumann boundary conditions; in addition, it allows a consistent treatment of variable viscosity; the derivation is given in Appendix A. These considerations are, of course, applicable to the unsteady Navier-Stokes problem with moving boundaries.

We consider the solution of the two-dimensional steady Stokes problem in a domain Ω which is fixed in time, with Dirichlet boundary condition defined on $\partial\Omega_u$ and Neumann boundary condition defined on $\partial\Omega_\sigma$. The variational statement for this problem is : find the solution $u_i \in \mathcal{H}_0^1(\Omega)$, $p \in \mathcal{L}^2(\Omega)$ such that

$$\int_\Omega v_{i,j}[\,-\delta_{ij}p \,+\, \mu\,(u_{i,j}+u_{j,i})\,]\,dV \;=\; \int_\Omega v_i\, f_i\, dV \;+\; \int_{\partial\Omega_\sigma} v_i\,\bar{t}_i\, dV \qquad \forall v_i \in \mathcal{H}_0^1(\Omega)\,, \qquad (4.27a)$$

$$\int_\Omega -q\,u_{l,l}\,dV \qquad \forall q \in \mathcal{L}^2(\Omega)\;; \qquad (4.27b)$$

where the various variables and solution spaces are defined in Section 3.2 (the steady Stokes problem is an important subset of the unsteady Navier-Stokes problem). Note that for the steady Stokes problem, we do not consider any free surfaces, and the generic applied traction on the Neumann boundary is denoted as $\bar{t}_i$.

Following similar procedures presented in the last section for the elastostatic problem, we first subdivide the domain into K spectral elements as given in Eq. (4.5). We shall now require that the variational statement given in Eq.(4.27) be satisfied for the piecewise-polynomial approximation spaces $\mathcal{X}_h$ for the velocity and $\mathcal{M}_h$ for the pressure, both spaces are defined in Ω_h. These spectral element approximation spaces are given by :

$$\mathcal{X}_h = \mathcal{H}_0^1(\Omega_k) \cap \mathcal{P}_{N,K}(\Omega_k) \,, \tag{4.28a}$$

$$\mathcal{M}_h = \mathcal{L}^2(\Omega_k) \cap \mathcal{P}_{N-2,K}(\Omega_k) \,; \tag{4.28b}$$

where $\mathcal{P}_{N,K}(\Omega_k)$ is given in Eq.(4.6) and $\mathcal{P}_{N-2,K}(\Omega_k)$ is similarly defined. It is shown in [54],[55] that the above choice of approximate solution spaces are compatible in the sense that spurious pressure modes are not present in the solution. We note that based on the choice of the above spaces, the degree of the polynomial in the pressure solution is *two* orders lower than that of the velocity solution.

For numerical evaluation of the elemental integrals, we define two integration rules, the first one by taking the tensor product of Gauss-Lobatto formulas for which we denote the collocation points and weights as (ξ_m, γ_m) for m=0,1,2,...,N. The second rule is obtained by taking the tensor product of the Gauss formulas, and we denote the collocation points and weights as $(\tilde{\xi}_m, \tilde{\gamma}_m)$ for m=1,2,...,N-1. The Gauss-Lobatto integration rule is given in Eq.(4.14), and the Gauss integration rule is

$$\int_{\Omega_k} g \, dV \;\Big|_G \;=\; \tilde{\gamma}_m \tilde{\gamma}_n \, |J^k(\tilde{\xi}_m, \tilde{\xi}_n)| \;\; g^k(\tilde{\xi}_m, \tilde{\xi}_n) \qquad \forall g^k \in C^0(\overline{\Omega}_k) \,,$$

where $J^k(\tilde{\xi}_m, \tilde{\xi}_n)$ is the Jacobian given in Eq.(4.12a), evaluated at the Gauss points. We remark that the N-point Gauss quardrature can be used to integrate exactly polynomials of degree (2N-1) or less [52].

Using the above quadrature, the discrete form of the variational statement given in Eq.(4.27) is : find the solution $(u_i)_h \in \mathcal{X}_h$ and $p_h \in \mathcal{M}_h$ such that

$$\sum_{k=1}^{K} \left[- a^k_{1,h-G}(v_i, p) + a^k_{2,h-GL}(v_i, u_j) \right] = \sum_{k=1}^{K} (v_i, f_i)^k_{h-GL} + \sum_l (v_i, \bar{t}_i)^l_{h-GL}$$
$$\forall v_i \in \mathcal{X}_h \,, \tag{4.29a}$$

$$\sum_{k=1}^{K} (q, u_{l,l})^k_{h-G} \;=\; 0 \qquad\qquad \forall q \in M_h \;; \qquad (4.29b)$$

where

$$a^k_{1,h-G}(v_i, p) \;=\; \tilde{\gamma}_m \tilde{\gamma}_n \, |J^k(\tilde{\xi}_m, \tilde{\xi}_n)| \;\; v^k_{i,\alpha}(\tilde{\xi}_m, \tilde{\xi}_n) [J^{-1}_{j\alpha}(\tilde{\xi}_m, \tilde{\xi}_n)]^k \\ \delta_{ij} \, p^k_h(\tilde{\xi}_m, \tilde{\xi}_n) \;, \qquad (4.30a)$$

$$a^k_{2,h-GL}(v_i, u_j) \;=\; \gamma_m \gamma_n \, |J^k(\xi_m, \xi_n)| \;\; \mu \, v^k_{i,\alpha}(\xi_m, \xi_n) \, [J^{-1}_{j\alpha}(\xi_m, \xi_n)]^k \\ \{ \, [u_{i,\alpha}(\xi_m, \xi_n)]^k_h \, [J^{-1}_{j\alpha}(\xi_m, \xi_n)]^k \;\; + \\ [u_{j,\alpha}(\xi_m, \xi_n)]^k_h \, [J^{-1}_{i\alpha}(\xi_m, \xi_n)]^k \, \} \;, \qquad (4.30b)$$

$$(v_i, f_i)^k_{h-GL} \;=\; \gamma_m \gamma_n \, |J^k(\xi_m, \xi_n)| \;\; f^k_i(\xi_m, \xi_n) \, v^k_i(\xi_m, \xi_n) \;, \qquad (4.30c)$$

$$(v_i, \bar{t}_i)^l_{h-GL} \;=\; \gamma_m \, |J^l_\zeta(\xi_m, \xi_N)| \;\; \bar{t}^l_i(\xi_m, \xi_N) \, v^l_i(\xi_m, \xi_N) \;, \qquad (4.30d)$$

$$(q, u_{l,l})^k_{h-G} \;=\; \tilde{\gamma}_m \tilde{\gamma}_n \, |J^k(\tilde{\xi}_m, \tilde{\xi}_n)| \, q^k(\tilde{\xi}_m, \tilde{\xi}_n) \, u^k_{l,\alpha}(\tilde{\xi}_m, \tilde{\xi}_n) \, [J^{-1}_{l\alpha}(\tilde{\xi}_m, \tilde{\xi}_n)]^k \;. \qquad (4.30e)$$

We note that the last summation in Eq.(4.29a) is performed over all spectral element l where $\partial\Omega_l \subset \partial\Omega_\sigma$. Also, in Eq.(4.30d) the traction boundary is assumed, for simplicity of presentation, to be at local coordinates s=1 (that is, at collocation points (ξ_m, ξ_N)). In addition, J_ζ in Eq.(4.30d) is the surface Jacobian which is given by

$$J^l_\zeta(\xi_m, \xi_N) \;=\; \{ \, [D_{mp}(x_1)^l_{pN}]^2 \;+\; [D_{mp}(x_2)^l_{pN}]^2 \, \}^{1/2} \;, \qquad (4.31)$$

where D_{mp} is defined in Eq.(4.18).

Next, we expand the coordinate (x_i), data (f_i), velocity (u_i) and test function (v_i) in the tensor-product form given by Eq. (4.16), and we expand the pressure (p) as

$$p_h^k(r,s) \;=\; \tilde{p}_{mn}^k \, \tilde{h}_m(r)\tilde{h}_n(s) \;, \tag{4.32}$$

where $\tilde{h}_m$ denotes the (N-2)th order elemental Lagrangian interpolants through the Gauss points, $\tilde{p}_{mn}^k$ is the pressure of element k, local collocation point (m,n), and the indices m and n are summed from 1 to N-1. The test function q is also expanded as given in Eq. (4.32).

We note that the polynomial order used in the interpolation for the geometry and velocity is N while that for the pressure is N-2, which corresponds to a staggered-mesh discretization. We remark that if all boundary conditions are of the Dirichlet type (which is not applicable to free-surface problems), then the pressure solution is determined to within an arbitrary constant (the hydrostatic mode), and a polynomial order of (N-2) will be required in the coordinate interpolation so that the hydrostatic mode can be represented correctly for deformed geometry [11].

Using the above expansions, the expressions given in Eq.(4.30) can be rewritten as

$$a_{1,h-G}^k(v_i,p) \;=\; \tilde{\gamma}_m\tilde{\gamma}_n \, |\tilde{J}|_{mn}^k \, (\hat{G}_j)_{mnpq}^k \, (v_i)_{pq}^k \, \delta_{ij} \, \tilde{p}_{mn}^k \;, \tag{4.33a}$$

$$\begin{aligned} a_{2,h-GL}^k(v_i,u_j) \;=\; & \gamma_m\gamma_n \, |J|_{mn}^k \, \mu \, (G_j)_{mnpq}^k \, (v_i)_{pq}^k \\ & [\, (G_j)_{mnrs}^k \, (u_i)_{rs}^k \;+\; (G_i)_{mnrs}^k \, (u_j)_{rs}^k \,] \;, \end{aligned} \tag{4.33b}$$

$$(v_i,f_i)_{h-GL}^k \;=\; \gamma_m\gamma_n \, |J|_{mn}^k \, (f_i)_{mn}^k \, (v_i)_{mn}^k \;, \tag{4.33c}$$

$$(v_i,\bar{t}_i)_{h-GL}^l \;=\; \gamma_m \, |J_\xi|_{mN}^l \, (\bar{t}_i)_{mN}^l \, (v_i)_{mN}^l \;, \tag{4.33d}$$

$$(q,u_{l,l})_{h-G}^k \;=\; \tilde{\gamma}_m\tilde{\gamma}_n \, |\tilde{J}|_{mn}^k \, \tilde{q}_{mn}^k \, (\hat{G}_l)_{mnpq}^k \, (u_l)_{pq}^k \;; \tag{4.33e}$$

where

$$(\hat{G}_j)^k_{mnpq} = (\tilde{J}^{-1}_{j1})^k_{mn} \widehat{D}_{mp} \hat{h}_{nq} + (\tilde{J}^{-1}_{j2})^k_{mn} \hat{h}_{mp} \widehat{D}_{nq} ; \tag{4.34}$$

and

$$\widehat{D}_{mp} = \frac{dh_p(\tilde{\xi}_m)}{dz} , \tag{4.35a}$$

$$\hat{h}_{mp} = h_p(\tilde{\xi}_m) ; \tag{4.35b}$$

$\tilde{J}_{mn}$ denotes $J(\tilde{\xi}_m, \tilde{\xi}_n)$, and $(G_i)^k_{mnpq}$ is given in Eq. (4.20). The final discrete system of algebraic equations for the steady Stokes problem are obtained by substituting Eq.(4.33) into Eq.(4.29), choosing the test functions v_i and q which are unity at one global collocation point while zero at others, and repeating this procedure successively through all collocation points. We then arrive at

$$\sum_{k=1}^{K}{}' (A_{ij})^k_{pqrs} (u_j)^k_{rs} - \sum_{k=1}^{K}{}' (D_i)^k_{rspq} \tilde{p}^k_{rs} = \sum_{k=1}^{K}{}' B^k_{pqrs} (f_i)^k_{rs} + \sum_{l}{}' (B_\zeta)^l_{pqrs} (\bar{t}_i)^l_{rs} , \tag{4.36a}$$

$$\sum_{k=1}^{K}{}' - (D_i)^k_{pqrs} (u_i)^k_{rs} = 0 ; \tag{4.36b}$$

where

$$(A_{ij})^k_{pqrs} = \gamma_m \gamma_n |J|^k_{mn} \mu [\delta_{ij} (G_l)^k_{mnpq} (G_l)^k_{mnrs} + (G_j)^k_{mnpq} (G_i)^k_{mnrs}] , \tag{4.37a}$$

$$(D_i)^k_{rspq} = \tilde{\gamma}_r \tilde{\gamma}_s |\tilde{J}|^k_{rs} (\hat{G}_i)^k_{rspq} , \tag{4.37b}$$

$$(B_\zeta)^l_{pqrs} = \gamma_p |J_\zeta|^l_{pq} \delta_{qN} \delta_{pr} \delta_{qs} ; \tag{4.37c}$$

and B^k_{pqrs} is given in Eq.(4.24b). We note that Eq.(4.36) can be expressed in matrix form as

$$\mathbf{A}_{ij}\,\mathbf{U}_j \;-\mathbf{D}_i^T\,\mathbf{P} \;=\; \mathbf{B}\,\mathbf{F}_i \;+\mathbf{B}_{\zeta}\,\overline{\mathbf{T}}_i \quad , \tag{4.38a}$$

$$-\,\mathbf{D}_i\,\mathbf{U}_i \;=\; 0 \quad ; \tag{4.38b}$$

where $\mathbf{A}_{ij}$ is the discrete viscous coefficient matrix, $\mathbf{B}$ is the mass matrix, $\mathbf{B}_{\zeta}$ is the surface-mass matrix, $\mathbf{D}_i$ is the discrete gradient matrix, and $\mathbf{U}_j$, $\overline{\mathbf{T}}_i$ and $\mathbf{P}$ store u_j, $\bar{t}_i$ and p, respectively, at all the collocation points.

4.3 Unsteady Navier-Stokes Problem

We consider in this section the spatial discretization of the variational form for the unsteady Navier-Stokes equations given in Eq.(3.10). A comparison of Eq.(3.10) and Eq.(4.27a) shows that the following contributions are not treated in the steady Stokes problem :

$$\frac{d}{dt}\sum_{k=1}^{K}(v_i,u_i)^k \;=\; \frac{d}{dt}\sum_{k=1}^{K}\int_{\Omega_k(t)}\rho\,v_i u_i\,dV \quad , \tag{4.39}$$

$$\sum_{k=1}^{K}c^k(v_i,u_j,w_l) \;=\; \sum_{k=1}^{K}\int_{\Omega_k(t)}\rho\,v_i\,[(u_i w_j)_{,j}-u_j u_{i,j}]\,dV \quad . \tag{4.40}$$

In addition, the generic Neumann boundary term given in Eq.(4.27a) takes the following form at the free surface :

$$\sum_{l}(v_i,\bar{t}_i)^l \;=\; \int_{\partial\Omega_l(t)}\sigma\,\kappa\,v_i^l\,n_i^l\,dA \quad . \tag{4.41}$$

In the following we briefly describe the Legendre spectral element discretization of these contributions, using the procedures presented in the last two sections. We remark that the variables in all of these expressions are defined on the velocity mesh; thus, we shall employ below the approximation space $\mathcal{X}_h$ given in Eq.(4.28a),

the Gauss-Lobatto quadrature formula given in Eq.(4.14), and the Gauss-Lobatto-Legendre basis given in Eq.(4.16).

We consider first the unsteady contribution given in Eq.(4.39). The elemental inner product can be expressed as

$$(v_i, u_i)^k_{h-GL} \;=\; (v_i)^k_{pq}\, \delta_{mp}\delta_{nq}\, \rho\, \gamma_m\gamma_n |J|^k_{mn}\, \delta_{mr}\delta_{ns} (u_i)^k_{rs} \,. \tag{4.42}$$

Thus, the corresponding discrete form for Eq.(4.39) is

$$\frac{d}{dt}\sum_{k=1}^{K} (v_i, u_i)^k_{h-GL} \;=\; \frac{d}{dt}\sum_{k=1}^{K} \rho\, (v_i)^k_{pq}\, B^k_{pqrs} (u_i)^k_{rs} \;; \tag{4.43}$$

where B^k_{pqrs} is given in Eq.(4.24b).

Next, we consider the nonlinear convective contributions given in Eq.(4.40) which can be expressed as

$$\begin{aligned} c^k_{h-GL}(v_i, u_j, w_l) \;=\; & (v_i)^k_{pq}\, \delta_{mp}\delta_{nq}\, \rho\, \gamma_m\gamma_n |J|^k_{mn} \\ & [(G_j)^k_{mnrs} (u_i w_j)^k_{rs} - (u_j)^k_{pq} (G_j)^k_{mnrs} (u_i)^k_{rs}] \,. \end{aligned} \tag{4.44}$$

Thus, the discrete form corresponding to Eq.(4.40) is

$$\sum_{k=1}^{K} c^k_{h-GL}(v_i, u_j, w_l) \;=\; \sum_{k=1}^{K} (v_i)^k_{pq} (C_i)^k_{pq} \;; \tag{4.45}$$

where

$$(C_i)^k_{pq} = \rho\gamma_p\gamma_q |J|^k_{pq}\, [(G_j)^k_{pqrs} (u_i w_j)^k_{rs} - (u_j)^k_{pq} (G_j)^k_{pqrs} (u_i)^k_{rs}] \;; \tag{4.46}$$

and $(G_j)^k_{pqrs}$ is given in Eq.(4.20).

Lastly, the free-surface boundary traction contribution given in Eq.(4.41) can be rewritten, considering planar geometry, as

$$\sum_{l} (v_i, \bar{t}_i)^l = \int_a^b -\sigma\, v_{i,j}\, s_i s_j\, d\zeta + \sigma\, v_i\, s_i \Big|_a^b . \qquad (4.47)$$

Assuming that for element l, the free surface is located at s=1 and the end point "b" (see Fig. 3-1) of the free surface is located at r=s=1. The discrete form of the traction boundary term for element l can then be expressed as

$$(v_i, \bar{t}_i)^l_{h\text{-}GL} = -\gamma_m |J_l|^l_{mN}\, \sigma (s_i)^l_{mN} (s_j)^l_{mN} (G_j)^l_{mN,pN} (v_i)^l_{pN} + \sigma (v_i)^l_{NN} (s_i)^l_{NN} ; \qquad (4.48)$$

where J_l is given in Eq.(4.31).

Thus, the discrete form corresponding to Eq.(4.47) is

$$\sum_{l} (v_i, \bar{t}_i)^l_{h\text{-}GL} = \sum_{l} (v_i)^l_{pq} (F_i^l)^l_{pq} ; \qquad (4.49)$$

where

$$(F_i^l)^l_{pq} = -\sigma\gamma_m |J_l|^l_{mn} (G_j)^l_{mnpq} (s_i)^l_{mn} (s_j)^l_{mn} \delta_{nN} \delta_{qN} + \sigma (s_i)^l_{pq} \delta_{pN} \delta_{qN} - \sigma (s_i)^l_{pq} \delta_{p0} \delta_{qN} . \qquad (4.50)$$

In Eq.(4.50), the last two terms is applicable only if the end points b and a, respectively, of the free surface are located in element l .

The discrete system of equations that correspond to the unsteady Navier-Stokes equations can now be put in the following form :

$$\frac{d}{dt} \sum_{k=1}^{K}{}' \rho B^k_{pqrs} (u_i)^k_{rs} = \sum_{k=1}^{K}{}' (D_i)^k_{rspq} \bar{p}^k_{rs} - \sum_{k=1}^{K}{}' (A_{ij})^k_{pqrs} (u_j)^k_{rs} + \sum_{k=1}^{K}{}' B^k_{pqrs} (f_i)^k_{rs} + \sum_{k=1}^{K}{}' (C_i)^k_{pq} + \sum_{l}{}' (F_i^l)^l_{pq} . \qquad (4.51)$$

We now combine the body force and the surface traction contributions as follows

$$\sum_{k=1}^{K}{}' (F_i)^k_{pq} = \sum_{k=1}^{K}{}' B^k_{pqrs}(f_i)^k_{rs} + \sum_{l}{}' (F^f_i)^l_{pq} .$$

The algebraic system of equations given in Eq.(4.51) can now be written in the following matrix equation

$$\frac{d}{dt}(\mathbf{B}\,\mathbf{U}_i) = \mathbf{D}_i^T\,\mathbf{P} - \mathbf{A}_{ij}\,\mathbf{U}_j + \mathbf{F}_i + \mathbf{C}_i . \tag{4.52}$$

We note that for free-surface flows, the coefficient matrices in Eq.(4.52) are implicit functions of time through their dependence on the current coordinates. The nodal point coordinates are updated using the mesh velocity as given in Eq.(3.16) which, in matrix form, is

$$\frac{d}{dt}\mathbf{X}_i = \mathbf{W}_i . \tag{4.53}$$

In summary, the semi-discrete equations that govern the unsteady Navier-Stokes free-surface flow are given by the momentum equation, Eq.(4.52); the domain time-evolution equation, Eq.(4.53); and the incompressibility condition, Eq.(4.38b).

CHAPTER 5

TEMPORAL DISCRETIZATION USING SEMI-IMPLICIT SCHEMES

Before we embark on the temporal discretization of the semi-discrete unsteady free-surface Navier-Stokes equations formulated in the last section, we discuss briefly below the motivations behind the use of semi-implicit schemes for the integration of the governing equations. The main advantage in using such schemes is the decoupling of the nonlinear contributions, namely the convective terms which involve low-order spatial derivatives and the free-surface update which involve no spatial derivatives, via explicit treatment. At the same time implicit treatment of the linear viscous contribution, which involves highest spatial derivatives, avoids severe stability restriction on the size of the time-step increment. Using such semi-implicit schemes, the step-by-step governing equations are effectively linear; thus, work- and/or storage-intensive equilibrium iteration procedures such as Newton-Raphson iteration are not required in their solution. Moreover, the coefficient matrices in these equations are symmetric, and the equations can easily be rewritten (using for example the Uzawa algorithm, see Chapter 6) such that the matrices are also positive definite. Such equations are effectively treated using well-developed, efficient and robust solution techniques such as preconditioned conjugate gradient iteration and multigrid techniques [56], for which convergence is extremely fast, and storage requirement is minimal (which is of significant importance in three-dimensional analysis). In addition, these solution techniques are easily amenable to parallelization and thus, all the advantages associated with parallel processing can be fully exploited [57],[58]. However, as in the case of fully explicit schemes, the size of the time-step increment for a semi-implicit scheme will be limited by both stability as well as accuracy considerations. Since the explicit treatment of the

convection contribution which leads to the Courant condition is well-documented [59],[11] we shall focus our attention below on the stability condition related to explicit treatment of the time evolution (update) of the free surface, as well as the selection of maximally stable (optimal) schemes.

In Section 5.1, we return to the Orr-Sommerfeld operator associated with the film-flow stability analysis which has already been introduced in Section 2.2.2. In this section, we consider the full eigenvalue spectrum from which we identify that capillary effect, when it dominates all other efects, is the limiting factor (for stability of numerical integration) when an explicit scheme is used for the free surface update. Next, we proceed to identify optimal combinations of implicit and explicit integration formulas such that the resulting semi-implicit schemes are maximally stable under the condition of dominant capillary action. In order to facilitate the determination of such optimal schemes, we present in Section 5.2 a system of two scalar ordinary differential equations that models the limiting eigenvalue composition in the Orr-Sommerfeld spectrum. Various combinations of implicit and explicit linear multi-step formulas are considered for the integration of the model equations and combinations that yield maximum critical step sizes are identified. In Section 5.3, we present the application of the resulting schemes to the inertia-free Orr-Sommerfeld equation associated with the film flow, with the purpose of verifying the optimality of the schemes when applied to the fluid-flow perturbation problem with its full spectrum of eigenvalues. Furthermore, the resulting discrete Orr-Sommerfeld operator can be used to provide critical step size estimate for direct flow simulation using spectral elements. Lastly, we present in Section 5.4 the application of the optimal schemes for temporal discretization of the semi-discrete spectral element equations from which the fully discrete system of step-by-step governing equations for viscous free-surface flows are derived.

5.1 Film Flow Stability Spectrum

In Section 2.2.2 we described the use of the most unstable eigenvalue in the solution of the Orr-Sommerfeld equation to determine the temporal stability of falling films. Although only one single eigenvalue is sufficient to determine linearized stability of the film flow problem, a deeper understanding of the underlying physics of the flow and the mathematical structure of the governing equations is provided by a study of the full eigenvalue spectrum. We start by presenting in Fig. 5-1 the eigenvalue spectrum for the case of Reynolds number R=1, Weber number W=100 and wave number $\alpha = 0.05$; the number of Hermitian elements used in the spatial discretization is 10. We recall that the real part (γ_r) of the complex eigenvalue corresponds to the growth rate, while the imaginary part (γ_i) is related to the wave speed (c) via the relation $\gamma_i = \alpha c$. Based on a study of the eigenvalue spectrum, we can identify below the various physical effects that affect the composition of the eigenvalues in the spectrum.

- Viscous dissipation — all the eigenvalues that lie on the left-half complex plane correspond to decaying eigenmodes due to viscous dissipation, the decay rate is proportional to the magnitude of γ_r. We remark that the fastest decaying rate is related to the mesh spacing Δl (which is inversely proportional to the number of Hermitian elements) as $(\gamma_r)_{min} \sim (\Delta l)^{-2}$.

- Physically unstable mode — this corresponds to the single eigenvalue located in the lower right corner in Fig. 5-1 for which $\gamma_r > 0$. The growth rate of this eigenmode is, however, several orders of magnitude smaller than the decay rate of the slowest decaying eigenmode; this makes the unstable character of the mode not easily discernable from the figure. This eigenvalue is associated with the vortical instability at the free surface, and the growth rate versus

Reynolds number relation given in Fig. 2-2 suggests that the instability is due to inertia effect which corresponds to a balance of gravity effect to viscous effect.

- Convective wave — the eigenvalues that lie on the lower-half complex plane correspond to a right-travelling (positive x_1) wave with wave speed equal to γ_i/α. We observe from Fig. 5-1 that all eigenvalues except two travel at approximately the same wave speed which is equal to the average streamwise velocity in the film; that is $\gamma_i = (2/3)\alpha$.

- Capillary wave — the single eigenvalue that lies on the top-half complex plane corresponds to a left-travelling (negative x_1) wave. We note that the wave speed of this eigenvalue and that of the physically unstable eigenvalue are distinctively different from the common wave speed of all other eigenvalues. Based on analyses using different numbers of Hermitian elements, the wave speeds of these two eigenvalues are found to be insensitive to the spatial discretization (Δl).

Further studies of the eigenvalue spectrum for varying flow parameters show that at very large values of Weber number (for example $W = 10^7$), we reach a limiting case in which the strong capillary effect manifests itself in the eigenvalue spectrum with the formation of a *standing wave*; that is, a complex conjugate eigenpair located approximately on the imaginary axis, see Fig. 5-2. In addition, the physically unstable eigenmode that occurs at low Weber numbers becomes stabilized, and the convective wave (in the capillary dominant frequency scale) becomes negligible, as all the eigenvalues (except the complex conjugate pair) can be observed to lie on the real axis.

In summary, based on the study of the eigenvalue spectrum associated with

the linearized film-flow stability analysis, we have identified various effects that affect the composition of the eigenvalue spectrum; namely, viscous effect, which is responsible for all decaying modes; inertia effect, which is responsible for the (physically) unstable mode; and surface-tension effect, which is responsible to the capillary standing wave mode. Therefore, the composition of the spectrum reveals the dominant effects for any given set of flow parameters. The link between the spectrum composition (and hence the dominant physical effects) and the stability of the integration scheme employed in the numerical simulation of the flow under the same physical effects can be established by examining the eigenvalue spectrum together with stability diagrams for explicit time integration schemes. We show in Fig. 5-3 the stability region for the integration of the ordinary differential equation

$$U_{,t} = \gamma U$$

using the (explicit) Adams-Bashforth scheme of orders one, two and three [60],[61]. Thus, the eigenvalues in the film flow spectrum (with proper scaling) which are nearest to the boundary of a stability region will be limiting for that particular integration formula. The eigenvalue spectrum as given in Fig. 5-2 suggests that when capillary effect is dominating (that is, at large Weber numbers), it will be a limiting factor which governs the size of the time-step increment (due to stability consideration) in the explicit update of the free surface. On the other hand, viscous effect (which is always present) will always be a limiting factor if the viscous contribution is treated explicitly. With the identification of all the relevant "stability-limiting" physical effects, effective integration schemes can then be selected judiciously based on the given flow parameters to achieve optimal stability.

In the numerical simulation of free-surface flows, the implicit treatment of

the dissipative contribution eliminates the severe restriction imposed on the critical step size (Δt_{cr}) by explicit schemes; namely, Δt_{cr} is proportional to $(\Delta L)^2$ where ΔL the mesh spacing. In contrast, explicit treatment of the convective contribution results in restriction on Δt_{cr} that is proportional to ΔL. The capillary standing wave mode is slightly dissipative, and it will be shown in Section 5.3 that the restriction on Δt_{cr} associated with explicit update of the free surface is proportional to $(\Delta L)^{3/2}$ in the limit that α approaches zero. Based on study of the eigenvalue spectrum, the step-size restriction due to explicit update of the free surface will be limiting when capillary effect is dominant (large Weber numbers). Hence, it is important to analyse this particular case and determine maximally stable semi-implicit schemes to treat this case effectively. This is achieved with the use of a model problem described in the next section.

5.2 Model Problem

The study of the model problem is motivated by the need to simulate the case of strong capillary effect, the limiting eigenvalues of the associated spectrum correspond to a pair of lightly damped complex conjugates. In addition, in determining the stability region (in the complex plane) for semi-implicit schemes, the effect of step size are implicitly coupled with the problem parameters; thus, generalized stability diagrams such as those given in Fig. 5-3 are not available.

We consider the following system of two scalar ordinary differential equations :

$$\frac{dv}{dt} = -k^2 v - f^2 \eta \,, \tag{5.1a}$$

$$\frac{d\eta}{dt} = v \; ; \tag{5.1b}$$

where the problem parameters k and f are real. We note that these two scalar equations are analogous to the Orr-Sommerfeld equation and its associated kinematic free-surface boundary condition in which inertia/gravity effect is negligible. In this analogy, dominant capillary effect in the physical problem is simulated in the model problem by appropriate selection of the numerical values for k^2 and f^2; thus, $k^2 \ll 2f$ in the model problem simulates dominant surface tension effect in the analogous physical problem.

We seek solution to Eq.(5.1) in the form

$$v(t) = \overline{v} e^{\gamma t} \tag{5.2a}$$

$$\eta(t) = \overline{\eta} e^{\gamma t} \tag{5.2b}$$

where γ is in general complex and is expressed as $\gamma = \gamma_r + i\gamma_i$, γ_r and γ_i being real; and $\overline{v}$ and $\overline{\eta}$ are the given initial conditions. Upon substitution of Eq.(5.2) into Eq.(5.1), we obtain

$$\frac{d}{dt}(e^{\gamma t}) \begin{bmatrix} \overline{v} \\ \overline{\eta} \end{bmatrix} = e^{\gamma t} \begin{bmatrix} -k^2 & -f^2 \\ 1 & 0 \end{bmatrix} \begin{bmatrix} \overline{v} \\ \overline{\eta} \end{bmatrix}$$

from which we obtain

$$\gamma_1 \, , \, \gamma_2 = -\frac{k^2}{2} \pm \sqrt{\left(\frac{k^2}{2}\right)^2 - f^2} \, .$$

We remark that *continuous* time derivative is taken in the evaluation of the above solutions, which have the following properties : (i) γ_1 and γ_2 are both real when $k^2 > 2f$ (monotonically decaying modes in the analogous physical problem) ; (ii) γ_1 and γ_2 form a complex conjugate pair when $k^2 < 2f$ (damped oscillatory capillary

mode in the analogous physical problem) ; and (iii) $\gamma_r \geq 0$ (no unstable modes in the analogous physical problem).

In order to use this model problem to identify maximally stable semi-implicit schemes, we follow the semi-implicit temporal discretization strategy by integrating Eq.(5.1a) using an implicit scheme and Eq.(5.1b) using an explicit scheme. For implicit formulas, we consider both the Adams-Moulton (AMI) formulas which are optimal in accuracy for a given number of steps (I) and the Backward Differentiation (BDI) formulas which are A-Stable for $I \leq 6$ [60]. For explicit formulas, we consider the Adams-Bashforth (ABJ) formulas which are optimal in accuracy among all the J-step explicit methods. We remark that the AM1 and BD1 formulas correspond to the familiar Euler backward formula, the AM2 formula corresponds to the trapezoidal rule which is also A-stable, and the AB1 formula corresponds to the Euler forward formula. For practical purposes, we consider only one- to three-step semi-implicit schemes, since higher-order explicit schemes have more stringent stability restriction.

In the following, we illustrate the semi-implicit time discretization procedures by presenting the discrete equations generated using the Euler backward/ Euler forward combinations. The procedure for higher-order schemes is analogous, and we describe the temporal discretization using the BD2/AB2 combination in Appendix B. Applying the Euler backward and Euler forward formulas to Eq.(5.1a) and (5.1b), respectively, we obtain

$$\frac{v^{n+1} - v^n}{\Delta t} = -k^2 v^{n+1} - f^2 \eta^{n+1} , \tag{5.3a}$$

$$\frac{\eta^{n+1} - \eta^n}{\Delta t} = v^n ; \tag{5.3b}$$

where n is a generic time-step number and Δt is the step size. Upon the substitution of Eq.(5.2) into the above equation, we arrive at the following eigenvalue problem

$$\begin{bmatrix} 1 & 0 \\ \Delta t & 1 \end{bmatrix} \begin{bmatrix} \bar{v} \\ \bar{\eta} \end{bmatrix} = e^{\hat{\gamma}\Delta t} \begin{bmatrix} 1 + k^2\Delta t & f^2\Delta t \\ 0 & 1 \end{bmatrix} \begin{bmatrix} \bar{v} \\ \bar{\eta} \end{bmatrix} \tag{5.4}$$

from which the eigenvalue $\hat{\gamma}$ can be solved for any given value of Δt. We remark that although Eq.(5.3) can easily be solved in closed-form, for higher-order schemes the resulting eigenvalue problem will be quadratic or cubic; thus, the formulation given in Eq.(5.4) and Appendix B is more effective.

The property of the solution that $\gamma_r \leq 0$ (obtained when continuous time derivative is taken) can now be used as a criterion to determine the critical step size. Since the continuous eigenvalues are never unstable, unstable discrete eigenvalues ($\hat{\gamma}_r$) in the finite time-difference solution of the same problem must due to the use of a step size which is larger than the critical step size (Δt_{cr}) for that particular problem; that is,

$$(\hat{\gamma}_r)_{max}\,|_{\Delta t > \Delta t_{cr}} \quad > \quad 0 \ . \tag{5.5}$$

Hence, the critical step size can be evaluated using the following condition

$$0 \ < \ (\hat{\gamma}_r)_{max}\,|_{\Delta t = \Delta t_{cr}} \ < \epsilon \ ;$$

where ϵ is an arbitrarily small positive number (a tolerance). One method of evaluating the critical step size is presented in the following. We first choose a step-size interval, and then we use a bisection method to successively reduce the size of the interval based on the sign of $(\hat{\gamma}_r)_{max}$ (that is, using the condition given in Eq.(5.5)), until an arbitrarily small sub-interval is reached. An example of the application of

the bisection method is schematically illustrated in Fig. 5-4, where typically a final subinterval size of 10^{-6} is used.

Since we are interested in the performance of the semi-implicit schemes for surface-tension dominant flows, we select for our model problem the following parameters : $k^2 = 0.2$ and $f^2 = 100.01$ for which the continuous solution is $\gamma_1, \gamma_2 = -0.1 \pm 10i$. We show in Table 5-1(a) and (b) the values of Δt_{cr} obtained using the various combinations of implicit/explicit multi-step formulas. We note from the results that the BDI/ABJ combinations, with I=J , are optimal since they yield the largest values of Δt_{cr} . Moreover, the critical step size is somewhat insensitive to the number of steps used in the scheme. We also present in Table 5-1(c) critical step-size results using *fully* explicit schemes, which demonstrate that even for nearly non-dissipative modes, the fully explicit schemes are less stable than the above optimal semi-implicit schemes. We also present in Table 5-2, for completeness, the results of Δt_{cr} for the case $k^2 = 12$ and $f^2 = 20$ for which the eigenvalues are real (dissipation dominant). We note that in this case the critical step size is limited by the performance (order) of the explicit scheme.

We conclude from the above study that the BDI/ABI semi-implicit formulas are optimal among those considered for explicit updating of the free surface when surface-tension effect is dominant and hence limiting. In addition, the critical step size for this case is insensitive to the number of steps (and hence the order) of the scheme; this implies that the more accurate higher-order schemes are advantageous. In the case of negligible surface-tension effect, the critical step-size is limited by the stability characteristics of the explicit scheme and therefore a low-order semi-implicit scheme is preferrable. However, in such a case explicit treatment of the convection contribution (the Courant condition) will most likely be limiting.

5.3 Discrete Orr-Sommerfeld Operator

We have identified in the last section that the combination of the implicit Backward Differentiation scheme and the explicit Adams-Bashforth scheme is optimal (i.e., maximally stable) for the integration of the model problem, the solution of which involves two eigenvalues. We now return to the Orr-Sommerfeld equation presented in Section 2.2.2 and evaluate the stability performance of these semi-implicit schemes when applied to the solution of the film-flow problem (and the full spectrum of eigenvalues), with the purpose of confirming that these schemes remain optimal.

Assuming that the stability requirement due to explicit treatment of convection can be superimposed onto the requirement due to explicit free-surface update, we shall neglect convection effect in the Orr-Sommerfeld equation and focus our attention on the stability conditions imposed by the explicit treatment of the free-surface evolution in the presence of strong capillary effect. Thus, we reformulate the Orr-Sommerfeld equation for the limiting case of zero Reynolds number, the spectrum of which will embody only the dissipative modes and the capillary standing-wave mode. Apart from the simplification enabled by the elimination of the convective terms, this limiting case has the important advantage that there is no physically unstable mode when *contiuous* time derivative is being taken. Consequently, if the continuous time derivative is replaced by a discrete time difference and if an unstable mode is present, this instability must due to the use of a step size which is larger than the critical step size (the same condition as given in Eq.(5.5)). Following this approach, a procedure similar to that used for the model problem can be employed to evaluate Δt_{cr} for any set of flow parameters.

The Orr-Sommerfeld equation for the limiting case R=0 is obtained by using

a viscous time scaling in the nondimensionalization of the Navier-Stokes equation, in which terms that are $O(R)$ are deleted. Thus, we scale length by h, time by h^2/ν, velocity by ν/h and pressure by σ/h, which result in the following equation

$$(D^2 - \alpha^2)^2 \hat{u}_2 \, e^{\gamma t} \;=\; (D^2 - \alpha^2)\hat{u}_2 \, \frac{d}{dt}(e^{\gamma t}) \qquad \text{in A ;} \tag{5.6}$$

subject to the boundary conditions :

$$\hat{u}_2 \;=\; D\hat{u}_2 \;=\; 0 \qquad \text{on } x_2 = 1 \,, \tag{5.7a}$$

$$(D^2 + \alpha^2)\hat{u}_2 \;=\; 0 \qquad \text{on } x_2 = 0 \,, \tag{5.7b}$$

$$(D^3\hat{u}_2 - 3\alpha^2 D\hat{u}_2 + \alpha^4 Fe^2 \hat{\eta}) \, e^{\gamma t} \;=\; D\hat{u}_2 \, \frac{d}{dt}(e^{\gamma t}) \qquad \text{on } x_2 = 0 \,, \tag{5.7c}$$

$$\hat{u}_2 \, e^{\gamma t} \;=\; \hat{\eta} \, \frac{de^{\gamma t}}{dt} \qquad \text{on } x_2 = 0 \,, \tag{5.7d}$$

where the notation and variables are defined in Section 2.2.2 , except that in Eq.(5.7c), the nondimensional parameter (Fe) corresponds to the Ohnesorge number, which is defined as

$$Fe \;=\; \sqrt{\frac{\sigma h}{\rho \nu^2}} \,.$$

We remark that in this limiting case, the nondimensional parameters that characterize the flow are the wave number and the Ohnesorge number. When capillary effect is large compared with viscous effect, we have $Fe \gg 1$.

For the solution of the eigenvalue γ, we rewrite Eq.(5.6), (5.7b) and (5.7c) in the following equivalent variational form : find a $\hat{v} \in \mathcal{H}_0^2(\mathrm{A})$ and a $\gamma \in C$, such that

$$\Big\{ \int_0^1 [\, D^2\hat{\phi} \, D^2\hat{u}_2 + 2\alpha^2 \, D\hat{\phi} \, D\hat{u}_2 + \alpha^4 \, \hat{\phi} \, \hat{u}_2 \,] \, dy - \alpha^2 \, \hat{\phi}(0) \, \hat{u}_2(0) -$$

$$\alpha^2\, D\hat{\phi}(0)\, \hat{u}_2(0) + \alpha^4\, Fe^2\, \hat{\phi}(0)\, \hat{\eta} \Big\}\; e^{\gamma t}$$

$$= -\left\{ \int_0^1 \left[\, D\hat{\phi}\, D\hat{u}_2 + \alpha^2\, \hat{\phi}\, \hat{u}_2 \,\right] dy \right\} de^{\gamma t}/dt \qquad \forall\, \hat{\phi} \in \mathcal{H}_0^2(\Lambda) \qquad (5.8)$$

where $\hat{\phi}$ is the test function, $\mathcal{H}_0^2(\Lambda)$ is the Sobolev space defined for the domain Λ and C is the set of complex numbers.

Next, we perform a Hermitian finite element discretization as described in Section 2.2.2 to arrive at the following algebraic eigenvalue problem

$$\mathbf{A}\, \mathbf{V}\, e^{\gamma t} = -\mathbf{B}\, \mathbf{V}\, de^{\gamma t}/dt\,; \qquad (5.9)$$

where $\mathbf{V}$ stores the nodal degrees-of-freedom of $\hat{u}_2$ and $D\hat{u}_2$ and $\mathbf{A}$ and $\mathbf{B}$ are the coefficient matrices generated from the Hermitian element discretization. We remark that Eq.(5.9) should be solved in conjunction with the kinematic free-surface condition given in Eq.(5.7d).

In order to formulate a procedure for critical step size determination, we need to replace the time derivative in Eq.(5.9) and (5.7d) with finite time differences. Using the semi-implicit approach given in the last section, we discretize the matrix equation given in Eq.(5.9) using implicit formulas, and the kinematic conditions given Eq.(5.7d) using explicit formulas. As an illustration, we consider the Euler backward/Euler forward combination. Applying the Euler backward formula to Eq.(5.9), we have

$$\mathbf{A}\, \mathbf{V}\, e^{\hat{\gamma}(n+1)\Delta t} = -\left(e^{\hat{\gamma}(n+1)\Delta t} - e^{\hat{\gamma} n \Delta t}\right) \frac{1}{\Delta t}\, \mathbf{B}\, \mathbf{V}\,,$$

where $\hat{\gamma}$ is the discrete eigenvalue solution and n is the time step number; viz., $t = n\Delta t$. The above equation can be simplified as

$$\frac{1}{\Delta t}\,\mathbf{B}\,\mathbf{V} \;=\omega\,(\mathbf{A}+\frac{1}{\Delta t}\,\mathbf{B})\mathbf{V}\;; \tag{5.10}$$

where $\omega \equiv e^{\hat{\gamma}\Delta t}$. Applying the Euler forward formula to the kinematic condition given in Eq.(5.7d), we have

$$\hat{u}_2(0) + \frac{1}{\Delta t}\,\hat{\eta} \;=\omega\,\frac{1}{\Delta t}\,\hat{\eta}\;. \tag{5.11}$$

By augmenting Eq.(5.10) with Eq.(5.11) as the last row, the final discrete eigenvalue problem is :

$$\widehat{\mathbf{A}}\,\widehat{\mathbf{V}} \;=\; \omega\,\hat{\mathbf{B}}\,\widehat{\mathbf{V}}\,, \tag{5.12}$$

where $\widehat{\mathbf{V}}$ now stores additionally the $\hat{\eta}$ degree-of-freedom. For any given set of flow parameters Fe^2 and α, we solve Eq.(5.12) for ω, from which $\hat{\gamma}$ can be determined using

$$\hat{\gamma} \;=\; \frac{1}{\Delta t}\,\ln\,\omega\,.$$

Once we have formulated an algorithm for the computation of $\hat{\gamma}$, the critical step size evaluation is again similar to that of the model problem. For any given set of flow parameters α and Fe^2 , we select an interval of step size and repeatedly bisect the interval until an arbitrarily small subinterval is reached. We present in Table 5-3 the crtical step sizes using BDI/ABJ and AMI/ABJ semi-implicit formulas for the following flow parameters : $\alpha = 9.24$ and Fe^2=$1, 10^4$ and 10^7. We observe from the results that the conclusions drawn from the model problem remain valid for the discrete Orr-Sommerfeld operator. Namely, in case of dominant capillary effect $(Fe^2 = 10^7)$, the BDI/ABJ schemes with I=J are distinctively superior to the other combinations, and that the critical step size is insensitive to the number of steps in

the scheme. In the case of negligible surface-tension effect ($Fe^2 = 1$), the explicit scheme is the limiting factor and thus low order semi-implicit scheme (that is, Euler backward/Euler forward) performs the best.

We can also apply the above critical-step-size procedure to obtain an estimate of Δt_{cr} for the spectral element simulation. This is achieved by noting that in the numerical simulation, the computational domain is truly two-dimensional and hence the effective wave number that should be used in the discrete Orr-Sommerfeld operator corresponds to

$$\alpha_{eff} = \frac{\pi h}{\Delta L} \tag{5.13}$$

where ΔL is the minimum spacing in the mesh.

It is of interest to determine the relation between Δt_{cr} and α_{eff} when α_{eff} is large since in the spectral element simulation, either h- or p-refinement will result in smaller mesh spacing. This relationship can be obtained through the use of the discrete Orr-Sommerfeld operator. For the case of dominant capillary effect (we choose $Fe^2 = 10^7$), we solve Eq.(5.12) and for $\alpha = 10^{-1}, 10^0, \ldots, 10^3$. The critical step size is plotted as a function of wave number in Fig. 5-5. We observe from the results that Δt_{cr} scales according to $\alpha^{-3/2}$ for large α. This is consistent with the result obtained from a capillary-versus-inertia force balance, which gives the following scaling relation as the wave number (α) and the capillary effect (Fe^2) go to infinity:

$$\Delta t_{cr} \sim \sqrt{\frac{\rho h^3}{\sigma \alpha^3}}\,. \tag{5.14}$$

Lastly, we remark for the case of negligible surface-tension effect, the Δt_{cr} that results from the Courant condition is, of course, more restrictive and hence will be

limiting.

In summary, we conclude that the BDI/ABI semi-implicit family which is found to be optimal for the scalar equations given in Section 5.2 is also optimal for the film flow problem. Thus, we shall select the BD1/AB1 and BD2/AB2 schemes for the temporal discretization of the spectral element equations. Secondly, explicit treatment of the free-surface evolution will result in critical step sizes whose dependence on the flow parameters can be estimated using the discrete Orr-Sommerfeld operator. This criterion should now supplement the Courant condition in the determination of stable time-step increments for direct simulation of free-surface flows using spectral element.

5.4 Discretization of the Spectral Element Equations

We present in this section temporal discretization of the semi-discrete spectral element equations for unsteady free-surface Navier-Stokes flows formulated in Section 4.3. Based on the conclusions presented in the last section, we apply the BDI family for the discretization of Eq.(4.52) and the ABI family for the discretization of Eq (4.53). We illustrate this procedure with the BD2/AB2 scheme.

Applying the BD2 formula for the temporal discretization of Eq.(4.52), we have

$$\frac{1}{\Delta t}\left[\frac{3}{2}\mathbf{B}^{n+1}\mathbf{U}_i^{n+1} - 2\mathbf{B}^{n}\mathbf{U}_i^{n} + \frac{1}{2}\mathbf{B}^{n-1}\mathbf{U}_i^{n-1}\right] =$$

$$(\mathbf{D}_i^{n+1})^T\mathbf{P}^{n+1} - \mathbf{A}_{ij}^{n+1}\mathbf{U}_j^{n+1} + \mathbf{F}_i^{n+1} + \sum_{l=0}^{2}\beta_l\,\mathbf{C}_i^{n-l}, \qquad (5.15a)$$

where the various matrices are defined in Sections 4.2 and 4.3, and the superscript

(n+1) denotes the current time step number for which the solution is sought, and n,(n-1),(n-2) denotes previous time steps at which the solution is known. The last term (which involves summation) in Eq.(5.15a) corresponds to explicit treatment of the nonlinear convection contributions using a modified third-order Adams-Bashforth scheme, where β_l are the modified AB3 coefficients : $\beta_0 = 8/3$, $\beta_1 = -7/3$ and $\beta_2 = 2/3$. These coefficients are different from the standard AB3 coefficients since the left-hand-side of Eq.(5.15a) involves BD2 coefficients. The modified AB3 coefficients are derived via Taylor series expansions in which the coefficients are selected such that terms that are of order $(\Delta t)^2$ or lower on both sides of the formula cancel each other. The stability region of the modified AB3 formula is slightly improved over the standard formula; a comparison is shown in Fig. 5-6. The incompressibility condition given in Eq.(4.38b) does not involve temporal derivative, and we have

$$\mathbf{D}_i^{n+1}\,\mathbf{U}_i^{n+1} \;=\; 0\,. \tag{5.15b}$$

Next, we apply the AB2 formula to Eq.(4.53) which yields

$$\frac{1}{\Delta t}\left[\,\mathbf{X}_i^{n+1} \;-\; \mathbf{X}_i^{n}\,\right] \;=\; \frac{3}{2}\mathbf{W}_i^{n} \;-\; \frac{1}{2}\mathbf{W}_i^{n-1}\,. \tag{5.16}$$

We have thus derived a set of fully discrete system of equations : Eq.(5.16) and Eq.(5.15) which can be solved (in that order) for each time step to obtain the response of the free-surface flow. The solution of such equations is discussed in the next section.

CHAPTER 6

EQUATION SOLVERS

In this chapter we present techniques which are effective for solution of the algebraic systems of equations derived in the previous chapters. We shall employ the conjugate gradient iteration method as our basic elliptic solver. The preconditioned conjugate gradient method [62] has emerged in the past decade as a robust and efficient algebraic equation solvers for positive definite and self-adjoint systems. Recent development of resolution-independent techniques such as the intra-element multigrid method for unsteady Navier-Stokes problem [56],[64] provides potentially even more efficient solvers for our application. This is one of the motivation in formulating the free-surface problem in such a way that these fast solvers can be employed in the solution.

Before we describe solution techniques applicable to the various problems formulated in earlier chapters, we discuss briefly below the advantages of effective iterative solvers (such as preconditioned conjugate gradient iteration) over more "traditional" direct solvers (such as Gauss elimination). Some of the advantages are pertained to our particular application; namely, unsteady solution of viscous free-surface flows.

- Memory requirement — the need to assemble a *global* coefficient matrix in direct method (even with static condensation [15],[16]) imposes severe memory requirement in the solution process. This requirement scales according to $O(K_1^d N^{2d})$ for direct solver and $O(K_1^d N^d)$ for iterative solver; where N is the polynomial degree of each spectral element, K_1 is the number of elements in a typical spatial direction and d is the number of spatial dimensions [11]. In

practical solution of three-dimensional problems, the memory requirement for direct solvers is so acute that even on the latest supercomputers, the number of elements that can be employed is often restricted.

- Operation counts — the number of operations required to obtain the solution depends largely on the number of space dimensions of the problem and the properties of the coefficient matrices (such as sparsity and conditioning). For two-dimensional analysis, the operation counts for direct solver and iterative solver are comparable, whereas in three-dimensional analysis, iterative solver requires less operations [63].

- Flexibility with variable solution parameters — direct method expends a relatively large initial cost in the factorization of the coefficient matrix. Hence, the method can be effective for unsteady problems in which the fluid properties, the flow geometry and the time-step increment are fixed. In this case the factorization is performed (initially) only once, and the factors are stored and used repeatedly during subsequently time steps. However, in our application the geometry of the flow domain changes at every time step; moreover, it is often desirable to adjust the step size (based on stability considerations). Consequently, if a direct solver is used, the cost involves in frequent refactorization of the coefficient matrix can be prohibitively expensive.

- Flexibility with the mesh construction — direct solvers often relies on judicious numbering of the elements in the mesh in order to achieve minimum bandwidth for the global coefficient matrix. Therefore, additional operations (which may be quite complex) are required to handle *local* mesh refinement which is essential in adaptive techniques. In contrast, local refinement is easily treated using iterative solvers without requiring any extra operations to achieve this flexibility [20].

- Parallel processing — recent advances in parallel computation enable slower (and thus cheaper) processors be used to achieve supercomputer speeds. The same concept can also be applied to fast processors to obtain drastic increase in computational speed. Iterative methods which are globally unstructured are highly efficient when adapted to parallel processing [58]; whereas the effectiveness of direct methods in a parallel environment is, due to their inherent global structure, compromised because of the need of extensive communication.

In Section 6.1 below, we present solution of the basic elliptic (elastostatic) problem using conjugate gradient iteration. We also introduce in that section tensor-product sum-factorization technique which is essential for efficient spectral element calculations. Next, in Section 6.2, we present solution of the steady-Stokes problem using the Uzawa algorithm, in which nested conjugate gradient iterations are employed for treatment of the saddle problem. Lastly, in Section 6.3, we present solution of the step-by-step free-surface Navier-Stokes equations. In the last two sections, we focus on appropriate preconditioners to improve the speed of convergence.

6.1 Elasticity Solver

We consider solution of the linear elastostatic problem formulated in Section 4.1 as an illustration of application of the conjugate gradient iteration for elliptic self-adjoint positive-definite systems. The two key considerations for effective application of the technique to the spectral element equations are the use of appropriate preconditioners, and effective computation of matrix-vector products.

The governing equations for the elastostatic problem are given in Eq.(4.23) or (4.25). The conjugate gradient iteration algorithm for the solution of this system of equations as adapted Ref. [62] is given in the following.

For $m = 1$ (initial calculations) :

$$(\mathbf{R}_i)_0 = \mathbf{BF}_i - (\mathbf{A}^E_{ij}\mathbf{U}_j)_0$$

$$(\mathbf{Q}_i)_1 = (\mathbf{R}_i)_0 .$$

For subsequent iterations $m > 1$:

$$\beta_m = (\mathbf{R}_i^T\mathbf{R}_i)_{m-1} / (\mathbf{R}_i^T\mathbf{R}_i)_{m-2}$$

$$(\mathbf{Q}_i)_m = (\mathbf{R}_i)_{m-1} + \beta_m (\mathbf{Q}_i)_{m-1}$$

For all iterations $m \geq 1$:

$$\alpha_m = (\mathbf{R}_i^T\mathbf{R}_i)_{m-1} / (\mathbf{Q}_i^T \mathbf{A}_{ij} \mathbf{Q}_j)_m$$

$$(\mathbf{R}_i)_m = (\mathbf{R}_i)_{m-1} - \alpha_m (\mathbf{A}_{ij} \mathbf{Q}_j)_m$$

$$(\mathbf{U}_i)_m = (\mathbf{U}_i)_{m-1} + \alpha_m (\mathbf{Q}_i)_m . \qquad (6.1)$$

We remark that in the iteration calculations, the matrices $\mathbf{A}_{ij}$ are never assembled, and the matrix-vector product $\mathbf{A}_{ij}\,\mathbf{Q}_j$ are instead computed element by element as $\sum_{k=1}^{K}{}' (A^E_{ij})^k_{pqrs} (q_j)^k_{rs}$.

We can show that the convergence rate of the conjugate gradient iteration

method depends on the condition number of the global coupled coefficient matrix **A** (which is assembled from $\mathbf{A}_{ij}$; i,j=1,...,d); that is, on $\kappa_A = (\lambda_A)_{max}/(\lambda_A)_{min}$ where λ_A denotes an eigenvalue of **A**. Hence, the convergence rate can be increased effectively by the use of appropriate preconditioner **M** such that $\mathbf{M}^{-1}\mathbf{A}\mathbf{M}^{-1}$ has improved condition number. Previous investigations have shown that for Laplacian operators, the Incomplete-Cholesky-factoriztion techniques [62] is not particularly effective and is difficult to adapt to parallel processing; and that a diagonal preconditioner (very inexpensive to invert) can increase the convergence rate by a factor of two [57],[64]. However, unlike the Laplacian operator, the $\mathbf{U}_j$ degrees-of-freedom are coupled and must be solved simultaneously in the elastostatic problem; these implies that the use of a diagonal preconditioner will not be satisfactory if the submatrices in various spatial directions have vastly different condition numbers (due, for example, to aspect ratio). The investigation of an appropriate preconditioner for the "coupled" problem will be an important topic for future study. In all our computation, we use the standard conjugate gradient technique given in Eq.(6.1).

The other consideration for effective solution is efficient computation of matrix-vector products, as we note from Eq.(6.1) that the most costly operation in the conjugate gradient scheme is the evaluation of $\mathbf{A}_{ij}\mathbf{Q}_j$. This cost obviously depends on N, the order of the polynomial expansion. For spectral element method N is relatively large; thus, it is imperative that these products be computed efficiently. This is achieved through use of the tensor-product sum-factorization technique due to Orszag [65]. We illustrate this technique using the following scalar example which is analogous to one of the elastostatic expression in, for example, Eq.(4.19). Consider the expansion of a scalar function Φ in three space dimensions :

$$\Phi_h(x_1, x_2, x_3) \;=\; \Phi_{lmn} G_{lmn}(x_1, x_2, x_3)\;, \tag{6.2}$$

where the repeated indices l,m,n are summed from 0 to N. If Eq.(6.2) is used directly, then the compution of Φ at all N^3 collocation points will require $O(N^6)$ operations. However, by choosing the space and basis expansions in tensor-product form (see Eq.(4.20)), we have

$$\Phi_h(x_1, x_2, x_3) = \Phi_{lmn} G_l(x_1) G_m(x_2) G_n(x_3) ,$$

which can be factorized into the following form:

$$\Phi_h(x_1, x_2, x_3) = [\,[\,[\,\Phi_{lmn} G_l(x_1)]\, G_m(x_2)]\, G_n(x_3)] . \tag{6.3}$$

We observe that using Eq.(6.3), $(\Phi_h)_{lmn}$ can be evaluated in $O(N^4)$. It is this efficient technique which enables the spectral element method to compete with lower order methods for which the same matrix-vector product will require $O(N^3)$ operations.

6.2 Steady Stokes Solver

The steady-Stokes problem as formulated in Section 4.2 corresponds to a saddle problem, the solution of which is not directly amenable to conjugate gradient iteration technique since the matrices of such equations are not positive definite. However, using an algorithm proposed by Uzawa, the saddle problem can be decomposed into two elliptic problems — a maximization problem for the pressure and a minimization problem for the velocity. This aproach has been employed successfully in previous steady-Stokes solvers in which Laplacian viscous operator is considered [11],[55].

In applying the Uzawa algorithm we multipy both sides of Eq.(4.38a) by

$\mathbf{D}_i\mathbf{A}_{ij}^{-1}$, and, using the continuity equation given in Eq.(4.38b), we obtain

$$(\mathbf{D}_i\,\mathbf{A}_{ij}^{-1}\,\mathbf{D}_j^T)\,\mathbf{P} \;=\; -\,\mathbf{D}_i\,\mathbf{A}_{ij}^{-1}\,\mathbf{B}\,\mathbf{F}_j \tag{6.4}$$

from which the pressure $\mathbf{P}$ can be solved using conjugate gradient technique (the coefficient matrix $\mathbf{D}_i\mathbf{A}_{ij}^{-1}\mathbf{D}_j^T$ is both self-adjoint and positive-definite). Once the pressure is solved, the velocity is obtained using

$$\mathbf{A}_{ij}\,\mathbf{U}_j \;=\; \mathbf{B}\,\mathbf{F}_i \;+\; \mathbf{D}_i^T\,\mathbf{P}\,. \tag{6.5}$$

We remark that in the solution of Eq.(6.4), each conjugate gradient iteration for the pressure solution involves the inversion of $\mathbf{A}_{ij}$ which is also performed using conjugate gradient iteration. Thus, a nested conjugate gradient algorithm is required for Eq.(6.4). We also note if the pressure solution is nontrivial, then most of the computation work will be performed on Eq.(6.4) since Eq.(6.5) involves only a single inversion.

A study of the viscous operator $\mathbf{A}_{ij}$ formulated in Eq.(4.37a) shows that its eigenvalue spectrum is similar to the Laplacian viscous operator. Hence, the mass matrix $\mathbf{B}$ which is an efficient preconditioner for the Laplacian viscous operator [11] is also appropriate for the solution of Eq.(6.4).

6.3 Unsteady Navier-Stokes Solver

The use of semi-implicit time-integration scheme as discussed Chapter 5 allows the formulation of step-by-step free-surface Navier-Stokes equations in which the matrices are self-adjoint and positive-definite. Thus the Uzawa algorithm and

nested conjugate gradient iteration can be used effectively as in the case of the steady-Stokes solver. In the rest of this section, we present the Uzawa decomposition of the unsteady free-surface Navier-Stokes equations, and appropriate preconditioners for effective solution. We remark that in solution of free-surface problems, the extension operation for the mesh velocity involves either the elastostatic solver or the steady-Stokes solvers which are described above; and, the explicit mesh update operation as given by Eq.(5.16) does not require solution of equations.

Applying the Uzawa algorithm to Eq.(5.15), we have for the pressure equation

$$
\begin{aligned}
(\mathbf{D}_i \, \widetilde{\mathbf{A}}_{ij}^{-1} \, \mathbf{D}_j^T)^{n+1} \, \mathbf{P}^{n+1} \;=\; & (\mathbf{D}_i \, \widetilde{\mathbf{A}}_{ij}^{-1})^{n+1} \left\{ \frac{2}{\Delta t} (\mathbf{B} \, \mathbf{U}_j)^n - \right. \\
& \left. \frac{1}{2\Delta t} (\mathbf{B} \, \mathbf{U}_j)^{n-1} + \mathbf{F}_j^{n+1} + \sum_{l=0}^{2} \beta_l \, \mathbf{C}_j^{n-l} \right\} . \qquad (6.6)
\end{aligned}
$$

and once the pressure solution is obtained, the velocity is computed using the equation

$$
\begin{aligned}
\widetilde{\mathbf{A}}_{ij}^{n+1} \, \mathbf{U}_j^{n+1} \;=\; & (\mathbf{D}_i^T \, \mathbf{P})^{n+1} + \mathbf{F}_i^{n+1} + \sum_{l=0}^{2} \beta_l \, \mathbf{C}_i^{n-l} + \\
& \frac{2}{\Delta t} (\mathbf{B} \, \mathbf{U}_i)^n - \frac{1}{2\Delta t} (\mathbf{B} \, \mathbf{U}_i)^{n-1} ; \qquad (6.7)
\end{aligned}
$$

where $\widetilde{\mathbf{A}}_{ij}$ is defined as

$$
\widetilde{\mathbf{A}}_{ij} \;=\; \mathbf{A}_{ij} + \frac{3}{2\Delta t} \delta_{ij} \, \mathbf{B} .
$$

Following the previous investigation by Rønquist [11], the appropriate preconditioner for Eq.(6.6) is given by

$$\mathbf{M}^{-1} = \mu \tilde{\mathbf{B}}^{-1} + \frac{\rho}{\Delta t} (\mathbf{D}_i \mathbf{B}^{-1} \mathbf{D}_i^T)^{-1}$$

where $\tilde{\mathbf{B}}$ is the mass matrix defined on the Gauss-Legendre (pressure) mesh. Recent investigation by Rønquist [66] shows that a more effective preconditioner can be constructed in which a intra-element multigrid technique is used in the inversion. The adaptation of such fast iterative solver for the present free-surface Navier-Stokes calculation will potentially produce a fivefold decrease in computational work to achieve convergence.

CHAPTER 7

SPECTRAL ELEMENT SOLUTION OF FREE-SURFACE FLOWS

In this section we present spectral element solution of several free-surface flow problems. First, We present the analysis of a stick-slip problem for which we apply the steady-Stokes formulation and solver. Next, we analyse the die-swell problem which corresponds to an example of steady-Stokes flow with a free surface. We then present numerical simulation (unsteady Navier-Stokes calculation) of film flow down a vertical plane for both infinitesimal and finite perturbations, which have been discussed in some detail in Chapter 2. Lastly, we consider film flow in axisymmetric geometry, and we present both linearized stability analysis of external film flow down a cylinder, and analysis of closure of a tube due to capillary instability (collapse) of an internal liquid film. We remark that although we do not present solution of any elastostatic problem (the formulation is given in detail in Section 4.1), most of the deformed geometry computations in the fluid-flow problems are performed using the elastostatic mesh solver.

7.1 Stick-Slip Problem

We consider steady Stokes flow of a Newtonian fluid in a straight planar channel, the wall of which consists of a "stick" section where the no-slip condition is applicable, and a "slip" section where the zero shear and zero normal velocity conditions are applicable. This problem is analyzed analytically by Richardson [67], and numerically in many investigations [68],[69]. The channel geometry, boundary conditions and spectral element model, in which eight fourth-order elements (K=8 and N=4) are used to model half the channel, are shown in Fig. 7.1. A parabolic

velocity distribution is imposed at the inflow boundary and the outflow boundary is assumed to be stress free. We compare in Fig. 7.2 and 7.3 the pressure distribution along the line of symmetry and the normal-traction distribution along the slip boundary, respectively, with the analytical solutions. It can be observed that the numerical prediction for the pressure distribution agrees quite closely with the analytic solution. In the case of the traction distribution, we note that wiggles are present in the numerical solution near the stick-slip junction, a location at which both the pressure and the shear stress are singular. The wiggles are, however, limited to the element immediately adjacent to the junction and the numerical solution is smooth downstream. This suggests that in order to obtain a more accurate solution, more elements (h-refinement) rather than higher order elements (p-refinement) should be used near the singularity.

7.2 Die-Swell Problem

This problem is similar to the last example, except that the slip boundary is replaced by a true free surface. The spectral element mesh employed is identical to the one used in the last example. To obtain the steady-state solution, we assume that the free surface is initially flat, and that the initial velocity distribution everywhere in the channel is the same as that at the inflow boundary, and we perform an unsteady Stokes calculation with a step size $\Delta t = 0.01$ until a steady state is reached. We show in Fig. 7.4 the velocity field at steady state predicted by the spectral element model, and we compare in Fig. 7.5 the numerical prediction of the free-surface position at steady-state with experimental solution [69]. Good agreement between the two solutions is observed. We remark that a surface tension of $\sigma = 0.001$ is used in the analysis to ensure that the free-surface problem

is well-posed; however, based on analyses with different values of surface tension (including $\sigma = 0$), the final solution is insensitive to σ as long as its numerical value is small compared with the viscosity. We further remark that at the junction "b" of the free surface and the stress-free boundary, we impose a zero contact angle that corresponds to $s_1|_b = 1$ and $s_2|_b = 0$ in Eq. (3.12).

7.3 Linearized Stability Analysis of Falling Films

We now present spectral element simulation of the planar falling film problem which has been discussed in some detail in Chapter 2. We consider the following set of flow parameters : R=1.935, W=0.844 and $\beta = 90°$ and we select the following four cases of wave number : α=0.196, 0.393, 0.628 and 0.785 in our numerical simulation. In each case, we model one wavelength of the film using a four-element mesh with polynomial order N=6, and we impose an initial sinusoidal perturbation of the free-surface position with an amplitude equal to 0.1 percent of the average film thickness to simulate the infinitesimal disturbance; see Fig. 7.6. The steady-state solution given in Eq.(2.5) is used as initial conditions, and we perform an unsteady Navier-Stokes calculation until the transient effect due to the imposed initial conditions become negligible; that is, the exponential growth/decay rate reaches a constant value. In Fig. 7.7(a) and (b) we plot the time history of the logarithm of the $\mathcal{L}^2$-norm of the perturbed velocity (which is defined in Eq.(2.6a)) and the height of the free surface at a fixed x_1 location, respectively, from which the growth rate and the wave speed can be evaluated. The growth/decay rate and wave speed for the above cases of α are compared in Fig. 7.8 with the solution evaluated from the Orr-Sommerfeld equation presented in Section 2.2.2. Excellent agreement between the Orr-Sommerfeld solutions and the numerical-simulation predictions can be ob-

served. These solutions are also in close agreement with those reported in previous investigations [29]. In order to achieve the accuracy as shown in the figures, we used a step size $\Delta t = 0.01$ which is smaller than the critical step size Δt_{cr} based on stability considerations. We remark that the discrete Orr-Sommerfeld operator formulated in Section 5.3 is used to provide critical step size estimates for the spectral element simulations; these estimates are found to be fairly accurate.

7.4 Nonlinear Stability Analysis of Falling Films

The spectral element simulation procedures used in nonlinear stability analysis of falling films are identical to those used in linearized stability analysis, with the exception that the amplitude of the perturbation is no longer small compared with the thickness. In addition, since we expect the free surface profile to be more complex than that of a sinusoid, more elements per wavelength of film are required to resolve the free-surface geometry. As discussed in Section 2.2.3, two types of laminar supercritically stable finite-amplitude steady periodic flow patterns were observed by Kapitza [38]. In the numerical simulation of the first type of flow (periodic ripples), we consider the following flow parameters: R=30.0, W=14.7, $\beta = 90°$ and α = 0.14. The average height of the film is computed using :

$$\bar{Q} = \frac{2}{3} h U_0 ;$$

where $\bar{Q}$ is the average volume flow rate given by Kapitza and U_0 is defined in Section 2.1. We remark that U_0 corresponds to the steady-state x_1-velocity at the free surface. The amplitude of perturbation is obtained using the reported value of $(h_{max} - h_{min})/(h_{max} + h_{min})$ given by Kapitza where h_{max} and h_{min} are the maximum and minimum film thicknesses at steady-periodic state, respectively. In the numerical simulation we perform an unsteady Navier-Stokes solution, using an

eight-element model (order N=6) for one wavelength of the film and a step size of $\Delta t = 2 \times 10^{-5}$, until a steady-periodic state is reached. This state is indicated by a time-invariant $\mathcal{L}^2$-norm of the velocity of the entire computational domain. We present in Fig. 7.9 the free-surface profile at steady-periodic state predicted by the spectral element simulation. For comparison purposes, we also show in the same figure the free-surface profile obtained experimentally by Kapitza, from which qualitative resemblance can be noted. The wave speed is computed in the numerical simulation by plotting the wave profile at two instants of time and noting the distance traversed along the x_1 direction by a particular point of fixed identity on the free surface. The numerical prediction of the wave speed for this case is c=22.8 cm/s, which compares favorably with the experimental value of c=21.7 cm/s.

The next type of supercritically stable finite-amplitude laminar film flow corresponds to single waves which occur at longer wavelengths than periodic ripples. The flow parameters for the case under consideration are : R=9.1, W=16.8, α=0.07 and $\beta = 90°$. For this type of wave we use a 16-element mesh (order N=6) to model one wavelength of the film and a step size $\Delta t = 2 \times 10^{-5}$ is used. The numerial prediction of the free-surface profile is compared with experimental results in Fig. 7.10. We observe that qualitatively, the dominant crest with its steepening front and the flat region between the crests are captured quite accurately; however, the smaller "dimples" are less accurately predicted. A comparison of the numerical wave speed of c=24.7 cm/s with the experimental value c=19.7 cm/s indicates that substantial discrepancy exists between the two solutions. This suggests that a more refined mesh may be required so that the wave profile is better resolved.

7.5 Linearized Stability Analysis of Cylindrical Falling Films

In this example we perform a spectral element simulation of linearized stability of a falling film on the external surface of a cylinder. In this case, the geometric parameters are the radius of the cylinder (R_i), the average radius of the film surface (R_o), and we define $\phi = R_i/R_o$ and h=$R_o - R_i$. The Reynolds number, Weber number and wave number are defined in the same way as in the case of planar geometry. The steady solution for cylindrical falling film is

$$\overline{U}_1 = \frac{\phi^2 - (x_2/R_o)^2 - 2\ \ln(R_i/x_2)}{\phi^2 - 2\ \ln\phi - 1} \tag{7.1a}$$

$$\overline{U}_2 = 0 \tag{7.1b}$$

$$\overline{P} = 0 \tag{7.1c}$$

$$\overline{\eta} = 0 \tag{7.1d}$$

and the scaling for velocity is

$$U_0 = \frac{gR_o^2}{4\nu}\ (\phi^2 - 2\ \ln\phi - 1)\ .$$

For linearized stability analysis we consider the following flow parameters : R_i=1, R_o=2, wave number $\alpha = 0.4$ and Weber number $W = 1$, and we perform the analysis for two cases of Reynolds number : R=1 and 10. In the spectral element discretization, we use four elements per wavelength of the film with order N=6, and we use a step size $\Delta t = 0.01$. The steady-state solutions given in Eq.(7.1a) to (7.1c) are used as initial conditions, and the spectral element simulation procedures are identical to those presented in Section 7.4. The growth rates for the above cases of Reynolds numbers are compared in Fig. 7.11 with the Orr-Sommerfeld solution given in Ref. [70] , and we note the good agreement between the two solutions.

7.6 Closure of a Tube due to Capillary Instability

In this problem we consider a thin film of liquid attached to the inner wall of a tube. When the free surface is perturbed, a pressure gradient in the longitudinal direction will be created due to imbalance of the surface-tension forces created by the curvature in both the longitudinal and circumferential directions. Based on the geometry of the tube and the film, such perturbation can be stable, supercritically stable or unstable. In this example we consider a case in which collapse of the film is predicted by a one-dimensional numerical model [71], and we apply our spectral element technique to confirm the collapse of the film and predict the closure time. This analysis is important in the study of the mechanism responsible for airway closure in the human lung [72]. The film geometry, boundary conditions, and fluid properties are given in Fig. 7.12. For this analysis we use an eight-element mesh (order N=6) to model one wavelength of the film, and we impose zero initial velocity and a free-surface perturbation amplitude equal to 1 percent the initial average film radius. An unsteady Navier-Stokes solution of the flow is performed using and a step size $\Delta t = 2 \times 10^{-7}$, until the center peak of the film reaches the axis of symmetry, at which point the closure time is obtained. In Fig. 7.13, we present the film configuration together with the velocity distribution at several instants of time, including the instant just before total collapse shown in Fig. 7.13(d). The closure time is found to be 0.0451 sec which is about 20 percent higher than that obtained using the one-dimensional model. This is, however, consistent with the assumptions used in the one-dimensional model, and with the fact that the flow becomes two-dimensional during the latter part of the solution. We remark that the initial growth rate of γ=94.6 sec^{-1} compared very closely with the analytical solution given by Goren [73] for axisymmetric films.

CHAPTER 8

OTHER TYPES OF MOVING BOUNDARY PROBLEMS

We have so far focused our attention on the treatment of one particular type of moving boundary problems, namely, free-surface fluid flows; and we have described in the previous chapters a new Legendre spectral element formulation and solver for effective analysis of such flows. We shall discuss in this chapter two other types of moving boundary problems which are amenable to treatment using the free-surface spectral element technique.

In Section 8.1, we consider fluid flows in domain bounded by a moving boundary, the velocity of which is prescribed as a function of time. Prominent examples include flows bounded by moving or pulsating walls which are commonly encountered in pumping of various fluids. This is followed by Section 8.2, in which we describe the treatment of multi-dimensional Stefan problems based on the Legendre spectral element formulation developed by Rønquist and Patera [74]. In the present study, the earlier formulation is extended to incorporate the arbitrary-Lagrangian-Eulerian description and elliptic mesh velocity solvers, which allow for more general and robust solution of the domain deformation due to the motion of the solidification/melting front. Examples are presented at the end of each section to illustrate the application of the free-surface spectral element technique to these types of analyses.

8.1 Prescribed-Boundary-Velocity Flows

We present in this section the analysis of a class of moving-boundary fluid-flow problems for which the time evolution of the velocity at the boundary is pre-

scribed. Such moving-boundary fluid-flow problems are, from a numerical simulation point of view, much simpler to treat than free-surface flows, since the moving boundary (and hence the domain configuration) is a known function of time. As a result, the boundary as well as the entire flow domain can be updated at each time step using implicit schemes which, unlike the explicit free-surface update, will not introduce any restriction on the size of the time-step increment due to stability considerations. We shall present both the formulation and some examples for this type of flow in the following sections.

8.1.1 Formulation

In order to adapt the free-surface algorithm to prescribed-boundary-velocity flows, we apply the following modifications to the boundary conditions formulated for free-surface flows. Since there are no free surfaces, the surface-tension boundary condition given in Eq.(3.5) and hence the boundary integral that appears in the variational statement given in Eq.(3.10) is no longer applicable. We assume that on the time-dependent boundary $\partial\Omega_u(t)$, the prescribed velocity is $\overline{u}_i(x_k,t)$. Thus, the Dirchlet boundary conditions given by Eq.(3.3) is still appropriate. For the mesh velocity computation, the kinematic conditions that no fluid particle can penetrate the moving wall is

$$w_i\, n_i \;=\; \overline{u}_i\, n_i \;, \tag{8.1}$$

and we retain Eq.(3.14b) in order to minimize mesh deformation. On the other non-moving boundaries, Eq.(3.14c) remains applicable. The extension of the mesh velocity in the interior domain as given by Eq.(3.15) is still appropriate. In the fully discrete equations presented in Section 5.4, these modifications imply that Eq.(5.15) is still applicable, except that the surface-tension contribution must be deleted in

the force vector $\mathbf{F}_i^{n+1}$. In addition, we use implicit integration scheme such as the trapezoidal rule to update the geometry; thus, Eq.(5.16) is replaced by

$$\frac{1}{\Delta t}\left[\mathbf{X}_i^{n+1} - \mathbf{X}_i^n\right] = \frac{1}{2}\left(\mathbf{W}_i^{n+1} + \mathbf{W}_i^n\right).$$

Lastly, we remark that even though the restriction on the step size due to geometry update is relaxed, the stability restriction due to explicit treatment of the convection contribution is still to be satisfied in the analysis.

8.1.2 Sample Analyses

We illustrate the solution of flows with prescribed boundary velocity by applying the free-surface spectral element method, with the above modifications incorporated, to the analysis of peristalic flows. Peristalsis is an important transport mechanism which is responsible for the pumping of liquid in the human urethra, and many investigations in the past have been devoted to this subject [75],[76],[77].

As our first example we consider planar peristaltic flows in which a travelling wave of given amplitude η, wave speed σ and period T propagates along the outer wall of an otherwise straight channel, the width of which is $2h$. We assume periodic boundary conditions in the longitudinal (x_1) direction and we consider a channel length equal to λ; see Fig. 8.1(a). The height of the moving wall as a function of time is given by

$$x_2(x_1,t) = h + \eta \cos l(x_1 - \sigma t)\ ;$$

and the velocity of the moving wall is given by

$$u_1 = 0$$

$$u_2 = l\,\sigma\,\eta\,sin\,l(x_1 - \sigma t)\,.$$

This problem is solved analytically by Burns and Parkes [75] for the case of Stokes flow, for which the Womersley number defined as

$$W_m = \frac{h^2}{\nu T}\,,$$

is small and therefore, the steady Stokes solution in a frame moving with the velocity σ is applicable. The spectral element mesh and boundary conditions employed in the numerical simulation are shown in Fig. 8.1(b). Note that only half of the channel is modelled based on symmetry considerations. We perform a transient Stokes calculation with zero initial conditions using a step size $\Delta t = 0.02$, until a steady-periodic state is reached (that is, the $\mathcal{L}^2$ norm of the velocity is time-invariant). We compare in Fig. 8.2 the spectral element solution of the velocity at steady-periodic state with the analytic solution (streamlines) for the case h=0.25 , $\eta = 0.025$, $l = 1$ and W_m=0.01. We note the excellent agreement between the two solutions. In Fig. 8.3, we compare the spectral element prediction of the net flux per period through a channel section with the analytical solution for various combinations of h and η, and again good agreement is observed.

As our second example, we consider peristalsis in a planar channel for large Womersley number, a case for which the steady Stokes solution in the moving reference frame is no longer applicable. The spectral element mesh used is the same as the last example and the flow parameters are : h=0.5, η=0.15 and W_m=25. We compare in Fig. 8.4 the velocity distribution in a typical section of the channel at large and small Womersley numbers. We observe that when W_m is small, the x_1-velocity distribution is parabolic along the channel section; and when W_m is large, a layer (Stokes layer) of rapidly moving fluid is formed near the wavy wall, while the

velocity in the center core is notably smaller and resembles a slug-flow distribution. This is consistent with the consideration that at large Womersley number, the time of excitation (due to the wavy wall) is much faster than the time of viscous diffusion and hence the periodic disturbance generated near the moving wall cannot diffuse all the way to the center of the channel.

Our last example corresponds to peristaltic flow at small Wormesley number in a circular tube. Even though an axisymmetric spectral element model is appropriate for this analysis, we employ three-dimensional spectral elements to demonstrate the three-dimensional solution capability of the algorithm. The spectral element mesh consists of 30 elements with N=6 and a step size $\Delta t = 0.02$ is used in the analysis. We show in Fig. 8.5 the geometry of the tube at several instants of time and we compare in Fig. 8.6 the average flux per period predicted using the spectral element model with the analytical solution given by Burns and Parkes [75].

8.2 Stefan Problem

The Legendre spectral element formulation for the Stefan problem is given in detail in Ref. [74]. In the following, we briefly describe the variational statement formulated using the arbitrary-Lagrangian-Eulerian description presented in Chapter 3, and the new *dynamic* condition for the mesh velocity at the solid-liquid interface. We also re-analyse one example in Ref. [74] to demonstrate the successful application of the current method.

8.2.1 Variational Formulation

In this section, we shall skip the presentation of the differential equations governing the heat transfer problem in the presence of a moving solid/liquid interface (the Stefan problem), and we refer to Ref. [74] for such details. The variational statement with the arbitrary-Lagrangian-Eulerian method incorporated is : find the temperature $\theta \in \mathcal{H}_0^1(\Omega(t))$, such that

$$\frac{d}{dt}\int_{\Omega(t)} \rho c\phi\theta \, dV \;=\; \int_{\Omega(t)} [-\phi_{,i}(k\theta)_{,i} + \phi q_B + \rho c\phi(\theta w_j)_{,j}] \, dV \tag{8.2}$$

for all $\phi \in \mathcal{H}_0^1(\Omega(t))$; where ϕ is the test function, k is the conductivity, ρc is the heat capacity, q_B is the heat generation per unit volume and w_j is the mesh velocity. Note that for simplicity of presentation we consider only Dirichlet boundaries on which the prescribed temperature is $\overline{\theta}$. At the solid-liquid interface, the temperature is assumed to be constant (θ_m), and the velocity at the interface is given by the following condition

$$\int_\Sigma \rho L\psi w_i n_i \, dS \;=\; \int_\Sigma \psi n_i \, [(k\theta)^s_{,i} - (k\theta)^l_{,i}] \, dS \tag{8.3}$$

where Σ is the solid-liquid interface, ρL is the latent heat of solidification, ψ is a test function, n_i is a unit vector normal to Σ and points towards the solid, and the superscripts "s" and "l" stand for solid and liquid, respectively. The spatial discretization of the above formulation is entirely analogous to the procedures given in Chapter 4. And, following our semi-implicit approach, we perform temporal discretization of Eq.(8.2) using implicit schemes and the interface (and hence the computational domain) time evolution, which is similar to Eq.(3.16), using explicit schemes. We remark that a linearized stability analysis similar to the discrete Orr-Sommerfeld operator (see Section 5.3) can be formulated to obtain a procedure for estimation of

the critical step size; however, such an investigation is not performed in the current study.

8.2.2 Sample Analysis

We perform a spectral element analysis of the two-dimensional Stefan problem given in Section 5.3 of Ref. [74] using the new formulation briefly discussed in the above section. The spectral element mesh, the material properties and the boundary conditions are given in Fig. 8.7(a). We perform a transient heat transfer analysis using a step size $\Delta t = 0.0025$, until a steady-state is reached. We present in Fig. 8.7(b) the temperature distribution and the position of the solid/liquid interface at steady state, which are essentially the same as the solutions given in the above reference. This example demonstrates that the free-surface spectral element technique (which is more general in the treatment of the domain deformation than the technique used in Ref. [74]) is also effective for treatment of heat transfer analysis with dynamic fronts.

CHAPTER 9

CONCLUSIONS

In this thesis, we have developed a new variational formulation for flow of incompressible viscous fluid in time-dependent domain as a result of the presence of a free surface. This formulation employs the full viscous stress tensor for treatment of (natural) traction boundary conditions and the Arbitrary-Lagrangian-Eulerian description for accurate tracking of the free-surface position.

The Legendre spectral element method which is effective for fixed domain fluid-flow problems has been extended for spatial discretization of the variational statement formulated for free-surface flows. In the temporal discretization, based on the existence of fast and efficient iterative equation solvers and effective parallel-processing algorithms, semi-implicit time-integration schemes have been selected to exploit these advantages. Using the physical insights obtained from the study of a typical free-surface fluid-flow problem (the stability of falling films), optimal semi-implicit integration formulas were identified for temporal discretization of the variational statement, and the stability of the time-integration scheme was also analysed.

Application of the resulting free-surface spectral element technique to the simulation of several free-surface fluid-flow problems demonstrated that the method is both accurate and effective. New results for several practically important free-surface fluid-flow problems were also generated.

The free-surface spectral element methodology is also applicable to other types of moving boundary problems. The method was successfully applied, first, to the class of problems in which the time-evolution of the velocity at the mov-

ing boundary is prescribed; and secondly, to the Stefan problem in which a time-dependent solid-liquid interface (dynamic solidification front) is present.

The extension of the surface-tension treatment in the variational formulation for three-dimensional analysis is obviously an important area for future investigation. In addition, efficient time-integration schemes which allow the use of larger step sizes are obviously advantageous for steady-state analysis of many free-surface problems; successful development of such schemes will therefore enhance the effectiveness of the present solution technique.

Finally, based on the performance of the proposed free-surface spectral element method in the solution of various moving boundary problems presented in this thesis, the proposed method represents a potentially effective approach for analysis of many other types of interesting moving boundary problems such as multi-fluid systems, fluid-structure interaction, two-phase flow and heat transfer, etc.

Bibliography

[1] J. Crank, *Free and Moving Boundary Problems*, Clarendon Press, Oxford, 1984.

[2] C.W. Hirt, A.A. Amsden and J.L. Cook, An Arbitrary Lagrangian-Eulerian Computing Method for All Flow Speeds, *J. Comp. Phy.*, **14**:227, 1974.

[3] J. Donea, Arbitrary Lagrangian-Eulerian Finite Element Methods, in T. Belytschko and T.J.R. Hughes, editors, *Computational Methods for Transient Analysis*, Ch.10, North-Holland, Amsterdam, 1983.

[4] T.J.R Hughes, W.K. Liu and T.K. Zimmermann, Lagrangian-Eulerian Finite Element Formulation for Incompressible Viscous Flows, *U.S.-Japan Seminar on interdisciplinary Finite Element Analysis*, Cornell Univ., Ithaca, 1978.

[5] B. Ramaswamy, Numerical Simulation of Unsteady Viscous Free Surface Flow, *J. Comp. Phy.*, submitted.

[6] J. Liu and D.B. Spalding, Numerical Simulation of Flows with Moving Interfaces, *PCH*, to appear.

[7] B. Ramaswamy and M. Kawahara, Lagrangian Finite Element Analysis Applied to Viscous Free Surface Fluid Flow, *Int. J. Num. Meth. Fluids*, **7**:953, 1987.

[8] H.S. Khesghi and L.E. Scriven, Penalty Finite Element Analysis of Unsteady Free Surface Flows, in R.H. Gallagher et.al., editors, *Finite Elements in Fluids*, **5**, J. Wiley, New York, 1984.

[9] T. Nakayama and K. Washizu, The Boundary Element Method Applied to the Analysis of Two-Dimensional Nonlinear Sloshing Problems, *Int. J. Num. Meth. Eng.*, **17**:1631, 1981.

[10] Y. Maday and A.T. Patera, Spectral Element Methods for the Navier-Stokes Equations, in A.K. Noor, editor, *State-of-the-art Surveys in Computational Mechanics*, ASME, New York, 1988.

[11] E.M. Rønquist, *Optimal Spectral Element Methods for the Unsteady Three-dimensional Incompressible Navier-Stokes Equations*, Ph.D. Thesis, Massachusetts Institute of Technology, 1988.

[12] A.T. Patera, A Spectral Element Method for Fluid Dynamics; Laminar Flow in a Channel Expansion, *J. Comp. Phy.*, **54**:468, 1984.

[13] I. Babuška and M.R. Dorr, Error Estimates for the Combined h- and p-Version of the Finite Element Method, *Num. Math.*, **37**:257, 1981.

[14] I. Babuška and B. Szabo, On the Rates of Convergence of the Finite Element Method, *Int. J. Num. Meth. Eng.*, **18**:323, 1982.

[15] E.T. Bullister, *Development and Application of High Order Numerical Methods for Solution of the Three-Dimensional Navier-Stokes Equations*, Ph.D. Thesis, Massachusetts Institute of Technology, 1986.

[16] K.Z. Korczak and A.T. Patera, An Isoparametric Spectral Element Method for Solution of the Navier-Stokes Equations in Complex Geometry, *J. Comp. Phy.*, **62**:361, 1986.

[17] G.E. Karndiadakis, *The Spectral Elements Method Applied to Heat Transport Enhancement by Flow Destabilization*, Ph.D. Thesis, Massachusetts Institute of Technology, 1987.

[18] C.H. Amon, *Heat Transfer Enhancement and Three-Dimensional Transitional Flows by a Spectral Element-Fourier Method*, Ph.D. Thesis, Massachusetts Institute of Technology, 1988.

[19] P. Fischer, L.W. Ho, G.E. Karndiadakis, E.M. Rønquist and A.T. Patera, Recent Advances in Parallel Spectral Element Simulation of Unsteady Incompressible Flows, In A.K. Noor, editor, *Proceedings of the Symposium on Fluid Dynamics and Structural Mechanics, Comp. and Struct.*, **30**:217, 1988.

[20] C.A. Mavriplis, *Nonconforming Discretizations and a Posteriori Error Estimators for Adaptive Spectral Element Techniques*, Ph.D. Thesis, Massachusetts Institute of Technology, 1989.

[21] W. Nusselt, *Verh. Deut. Ung. Z*, **60**:549, 1916.

[22] S.P. Lin, Film Waves, in *Waves on Fluid Interfaces*, Academic Press, 1983.

[23] P.L. Kapitza, Wave Flow of Thin Layers of a Viscous Fluid, in D.Ter Haar, editor, *Collected Papers of P.L. Kapitza*, 662, Pergamon Press, Oxford, 1965.

[24] C.S. Yih, Stability of Parallel Laminar flow with a Free Surface, *Proc. 2nd U.S. Congr. Appl. Mech.*, ASME, 623, 1954.

[25] C.S. Yih, Stability of Liquid Flow down an Inclined Plane, *Phy. Fluids*, **6**:321, 1963.

[26] C.S. Yih, *Dynamics of Nonhomogeneous Fluids*, Ch. 8, MacMillan, New York.

[27] T.B. Benjamin, Wave Formation in Laminar Flow down an Inclined Plane, *J. Fluid Mech.*, **2**:554, 1957.

[28] B.E. Anshus and S.L. Goren, A Method of Getting Approximate Solutions to the Orr-Sommerfeld Equation for Flow on a Vertical Wall, *A.I.Ch.E.*, **12**:1004, 1966.

[29] W.B. Krantz and S.L. Goren, Stability of Thin Liquid Films Flowing down a Plane, *Ind. Eng. Chem. Fundam.*, **10**:91, 1971.

[30] F.W. Pierson and S. Whitaker, Some Theoretical and Experimental Observations of the Wave Structure of Falling Liquid Films, *Ind. Eng. Chem. Fundam,*, **16**:401, 1977.

[31] R.W. Chin, F.H. Abernathy and J.R. Berstschy, Gravity and Shear Wave Stability of Free Surface Flows, Part I, Numerical Calculations, *J. Fluid Mech.*, **168**:501, 1986.

[32] H.S. Kheshgi and L.E. Scriven, Disturbed Film Flow on a Vertical Plate, *Phy. Fluids*, **30**:990, 1987.

[33] P.G. Drazin and W.H. Reid, *Hydrodynamic Stability*, Cambridge Univ. Press, 1981.

[34] H. Kozlu and A.T. Patera, Solution of the Free-Surface Orr-Sommerfeld Equation of Hydrodynamic Stability Theory by a Hermitian Finite-Element Method, *App. Num. Math.*, submitted.

[35] G.D. Fulford, The Flow of Liquids in Thin Films, *Adv. Chem. Eng.*, 5:151, 1964.

[36] A.T. Kirkpatrick, *Wave Mechanics of Inclined and Rotating Liquid Films*, Ph.D. Thesis, Massachusetts Institute of Technology, 1981.

[37] S.H. Hwang and H.C. Chang, Turbulent and Inertia Roll Waves in Inclined Film Flow, *Phy. Fluids*, 30:1259, 1987.

[38] P.L. Kapitza, Experimental Study of Undulatory Flow Conditions, in D.Ter Haar, editor, *Collected Papers of P.L. Kapitza*, 690, Pergamon Press, Oxford, 1965.

[39] R.W. Atherton and G.M. Homsy, On the Derivation of Evolution Equations for Interfacial Waves, *Chem. Eng. Comm.*, 2:57, 1976.

[40] C. Nakaya, Long Waves on a Thin Fluid Layer Flowing down an Inclined Plane, *Phy. Fluids*, 18:1408, 1975.

[41] B. Gjevik, Occurrence of Finite-Amplitude Surface Waves on Falling Liquid Films, *Phy. Fluids*, 13:1918, 1970.

[42] S.P. Lin, Finite-Amplitude Stability of a Parallel Flow with a Free Surface, *J. Fluid Mech.*, 36:113, 1968.

[43] S.P. Lin, Roles of Surface Tension and Reynolds Stresses on the Finite Amplitude Stability of a Parallel Flow with a Free Surface, *J. Fluid Mech.*, 40:307, 1969.

[44] S.P. Lin, Profile and Speed of Finite Amplitude Waves in a Falling Liquid Layer, *Phy. Fluids*, 14:263, 1971.

[45] V.E. Nakoryakov, B.G. Pokusaev, S.V. Alekseenko and V.V. Orlov, Instantaneous Velocity Profile in a Wavy Fluid Film, *J. Eng. Phy.*, **33**:1012, 1977.

[46] O.Yu. Tsvelodub, Steady-State Traveling Waves on a Vertical Liquid Film, *Fluid Mech. - Soviet Research*, **10**:1, 1981.

[47] E.A. Demekhin, M.A. Kaplan and V. Ya. Shkadov, Mathematical Models of the Theory of Viscous Liquid Films, *Izves. Akadem. Nauk SSSR*, **22**:885, 1987.

[48] K.J. Ruschak, A Method for Incorporating Free Boundaries with Surface Tension in Finite Element Fluid-Flow Simulation, *Int. J. Num. Meth, Eng.*, **15**:639, 1980.

[49] E.B. Dussan V., On the Difference between a Bounding Surface and a Material Surface, *J. Fluid Mech.*, **75**:609, 1976.

[50] W.J. Gordan and C.A. Hall, Transfinite Element Method. Blending Function Interpolation over Arbitrary Curved Element Domains, *Num. Math,*, **21**:109, 1973.

[51] G.L.D, Sidén and D.R. Lynch, Wave Equation Hydrodynamics on Deforming Elements, *Int. J. Num. Meth. Fluids*, to appear.

[52] A.H. Stroud and D. Secrest, *Gauss Quadrature Formulas*, Prentice-Hall, New Jersey, 1966.

[53] L.D. Landau and E.M. Lifshitz, *Theory of Elasticity*, 3rd ed., Pergamon Press, Oxford, 1986.

[54] C. Bernardi and Y. Maday, Analysis of a Staggered Grid Algorithm for the Stokes Equations, *Int. J. Num. Meth. Fluids*, **8**:537, 1988.

[55] Y. Maday, A.T. Patera and E.M. Rønquist, A Well-Posed Optimal Spectral Element Approximation for the Stokes Problem, *ICASE Report*, **87-48**, 1987.

[56] E.M. Rønquist and A.T. Patera, Spectral Element Multigrid I. Formulation and Numerical Results, *J. Sci. Comp.*, **2**:389, 1987.

[57] P.F. Fischer and A.T. Patera, Parallel Spectral Element Solution of the Stokes Problem, *J. Comp. Phy.*, to appear.

[58] P.F. Fischer, *Spectral Element Solution of the Navier-Stokes Equations on High Performance Distributed-Memory Parallel Processors*, Ph.D. Thesis, Massachusetts Institute of Technology, 1989.

[59] P.J. Roache, *Computational Fluid Dynamics*, Hermosa, Albuquerque, 1972.

[60] C.W. Gear, *Numerical Initial Value Problems in Ordinary Differential Equations*, Prentice-Hall, New Jersey, 1971.

[61] L.N. Trefethen, A Course in Finite Difference and Spectral Methods, *Notes for Course 18.336*, Dept. Math., MIT, 1987.

[62] G.H. Golub and C.F. van Loan, *Matrix Computations*, Johns Hopkins Univ. Press, Baltimore, 1983.

[63] A.T. Patera, Computational Fluid Dynamics – Incompressible Fluid Flow with Heat Transfer, *Notes for Course 2.274*, Dept. Mech. Eng., MIT, 1986.

[64] Y. Maday and R. Munoz, Spectral Element Multigrid II. Theoretical Justification, *J. Sci. Comp.*, to appear.

[65] S.A. Orszag, Spectral Methods for Problems in Complex Geometries, *J. Comp. Phy.*, **37**:70, 1980.

[66] E.M. Rønquist, *Private Communication*, 1989.

[67] S. Richardson, A 'Stick-Slip' Problem Related to the Motion of a Free Jet at Low Reynolds Numbers, *Proc. Camb. Phil. Soc.*, **67**:477, 1970.

[68] R.E. Nickell, R.I. Tanner and B. Caswell, The Solution of Viscous Incompressible Jet and Free-Surface Flows Using Finite-Element Methods, *J. Fluid Mech.*, **65**:189, 1974.

[69] P.W. Chang, T.W. Patten, F.T. Adams and B.A. Finlayson, Galerkin and Collocation Finite Element Methods for Newtonian and Viscoelastic Fluids, in E. Hinton and R.L. Taylor, editors, *Recent Advances in Numerical Methods in Fluids*, **1**, Ch.4, Pineridge, Swansea, 1980.

[70] F.J. Solorio and M. Sen, Linear Stability of a Cylindrical Falling Film, *J. Fluid Mech.*, **183**:365, 1987.

[71] M. Johnson, *Private Communication*, 1989.

[72] R.D. Kamm and R.C. Schroter, Is Airway Closure Caused by a Liquid Film Instability ? , *Respir. Physio.*, **75**:141, 1989.

[73] S.L. Goren, The Instability of an Annular Thread of Liquid, *J. Fluid Mech.*, **12**:309, 1962.

[74] E.M. Rønquist and A.T. Patera, A Legendre Spectral Element Method for the Stefan Problem, *Int. J. Num. Meth. Eng.*, **24**:2273, 1987.

[75] J.C. Burns and T. Parkes, Peristaltic Motion, *J. Fluid Mech.*, **29**:731, 1966.

[76] A.H. Shapiro, M.Y. Jaffrin and S.L. Weinberg, Peristaltic Pumping with Long Wavelengths at Low Reynolds Number, *J. Fluid Mech.*, **37**:799, 1969.

[77] C.P. Yin and Y.C. Fung, Comparison of Theory and Experiment in Peristaltic Transport, *J. Fluid Mech.*, **47**:93, 1971.

APPENDIX A

CONSISTENT TREATMENT OF VARIABLE VISCOSITY

We presented in Chapter 3 and 4 a Newtonian fluid constitutive relation in which the full viscous stress tensor is employed; see, for example, Eq.(3.6a) and Eq.(4.27a). This constitutive relation is selected in order to provide a consistent treatment of inhomogeneous traction boundary conditions applied at general curvilinear Neumann boundaries (such as the free surface) in the variational formulation. We remark that even though we do not present any analysis of variable-viscosity fluid flow problems in this thesis, a consistent variable viscosity formulation is important since in many practical applications, the viscosity of the working fluid is sensitive to the fluid temperature.

In this appendix, we shall show that in the case of variable viscosity, the full viscous stress tensor must be used in the variational formulation even when inhomogeneous Neumann boundary conditions are not present. In the following discussion, we shall assume for simplicity of presentation that the domain Ω is fixed in time and Dirichlet condition is applicable on the domain boundary, and that the viscosity is a function of the spatial coordinates.

The viscous contribution in the variational statement when the full viscous stress tensor is used can be expressed as :

$$I_S = \int_\Omega v_{i,j}\, \mu\, (u_{i,j} + u_{j,i})\, dV \ , \tag{A.1}$$

where u_i is the fluid velocity, v_i is the test function, μ is the variable viscosity and $u_{i,j} \equiv \partial u_i / \partial x_j$. Applying integration by parts to Eq.(A.1) and using the incompressibility condition

$$u_{j,j} = 0 ,$$

we obtain

$$I_S = \int_\Omega -v_i[\, \mu_{,j} \, (u_{i,j} + u_{j,i}) \, + \, \mu \, u_{i,jj} \,] \, dV \, . \tag{A.2}$$

The viscous contribution in the variational statement using the Laplacian operator treatment of the viscous contribution can be expressed as :

$$I_L = \int_\Omega v_{i,j} \, \mu \, u_{i,j} \, dV \, . \tag{A.3}$$

Again, we apply integration by parts to Eq.(A.3) and we obtain

$$I_L = \int -v_i \, [\, \mu_{,j} \, u_{i,j} \, + \, \mu \, u_{i,jj} \,] \, dV \, . \tag{A.4}$$

A comparison of Eq.(A.2) and (A.4) shows that the term $\mu_{,j} u_{j,i}$ is missing in the Laplacian viscous formulation due to the elimination of the term $u_{j,i}$ in the strong form of the Navier-Stokes equation. Therefore, we conclude that the formulation given in Eq.(A.1) should be used to treat variable viscosity.

APPENDIX B

TEMPORAL DISCRETIZATION OF THE MODEL PROBLEM USING BD2/AB2 SEMI-IMPLICIT SCHEME

In this appendix we illustrate the application of higher-order semi-implicit integration formulas for the temporal discretization of the model problem given in Eq. (5.1). We remark that our goal is to formulate the discrete equations in the form of a linear algebraic eigenvalue problem, the solution of which can be obtained using standard eigenproblem solution packages such as EISPACK.

Applying the second-order backward differential (BD2) formula to Eq.(5.1a), we have

$$\frac{3}{2}v^{n+1} - 2v^n + \frac{1}{2}v^{n-1} = \Delta t\,(-k^2\,v^{n+1} - f^2\,\eta^{n+1})\,. \tag{B.1}$$

Similarly, applying the second-order Adams-Bashforth (AB2) formula to Eq.(5.1b), we obtain

$$\eta^{n+1} - \eta^n = \Delta t\,(\frac{3}{2}v^n - \frac{1}{2}v^{n-1})\,. \tag{B.2}$$

Next, we substitute the assumed solution given in Eq.(5.2) into Eq.(B.1) and (B.2) and after collecting terms, we obtain

$$2\hat{v} - \frac{1}{2}\hat{v}^* = e^{\gamma\Delta t}\,[\,(\frac{3}{2} + k^2\Delta t)\,\hat{v} + f^2\Delta t\,\hat{\eta}\,]\,, \tag{B.3}$$

and

$$\frac{3}{2}\Delta t\hat{v} - \frac{1}{2}\Delta t\hat{v}^* + \hat{\eta} = e^{\gamma\Delta t}\,\hat{\eta}\,; \tag{B.4}$$

where $\hat{v}^* = \hat{v}e^{\gamma\Delta t}$. We can now rewrite Eq.(B.3) and (B.4) as the following eigen-

value problem :

$$\begin{bmatrix} 2 & -1/2 & 0 \\ 1 & 0 & 0 \\ 3\Delta t/2 & -\Delta t/2 & 1 \end{bmatrix} \begin{bmatrix} \hat{v} \\ \hat{v}^* \\ \hat{\eta} \end{bmatrix} = e^{\gamma \Delta t} \begin{bmatrix} 3/2 + k^2 \Delta t & 0 & f^2 \Delta t \\ 0 & 1 & 0 \\ 0 & 0 & 1 \end{bmatrix} \begin{bmatrix} \hat{v} \\ \hat{v}^* \\ \hat{\eta} \end{bmatrix} . \quad \text{(B.5)}$$

We note that by expanding the eigenvector to include the solution variable which corresponds to a previous step, the quadratic eigenvalue problem that would have resulted from Eq.(B.1) and (B.2) is converted into a linear one which has the same form of Eq.(5.4). We remark that the same procedure is applicable to semi-implicit schemes of arbitrary number of steps.

TABLES AND FIGURES

TABLE 5.1 Critical step size for the model problem for the case $k^2 = 0.2$ and $f^2 = 100.1$ using : (a) Backward Differentiation (BD) and Adams-Bashforth (AB) formulas; (b) Adams-Moulton (AM) and Adams-Bashforth (AB) formulas; and (c) fully explicit Adams-Bashforth (AB) formulas.

SCHEME	AB1	AB2	AB3	AB4
BD1	0.2020	0.1424	0.1050	0.0778
BD2	0.0040	0.2010	0.1482	0.1098
BD3	0.0040	0.0341	0.1912	0.1417
BD4	0.0040	0.0396	0.0853	0.1792

(a)

SCHEME	AB1	AB2	AB3	AB4
AM1	0.2020	0.1424	0.1050	0.0778
AM2	0.0040	0.0425	0.1154	0.1179
AM3	0.0040	0.0401	0.1013	0.1024
AM4	0.0040	0.0420	0.0984	0.0927

(b)

SCHEME	Δt_{cr}
AB1	0.0020
AB2	0.0332
AB3	0.0720
AB4	0.0428

(c)

TABLE 5.2 Critical step size for the model problem for the case $k^2 = 12$ and $f^2 = 20$ using : (a) Backward Differentiation (BD) and Adams-Bashforth (AB) formulas; (b) Adams-Moulton (AM) and Adams-Bashforth (AB) formulas; and (c) fully explicit Adams-Bashforth (AB) formulas.

SCHEME	AB1	AB2	AB3	AB4
BD1	1.3483	0.7359	0.4488	0.2852
BD2	1.4718	0.8385	0.5322	0.3510
BD3	1.6132	0.9506	0.6204	0.4188
BD4	1.7944	1.0895	0.7273	0.5000

(a)

SCHEME	AB1	AB2	AB3	AB4
AM1	1.3483	0.7359	0.4488	0.2852
AM2	1.2000	0.6917	0.4761	0.3508
AM3	0.9746	0.5169	0.3352	0.2392
AM4	0.9045	0.4514	0.2791	0.1931

(b)

SCHEME	Δt_{cr}
AB1	0.2000
AB2	0.1000
AB3	0.0545
AB4	0.0300

(c)

TABLE 5.3 Critical step size for the discete Orr-Sommerfeld operator at $R = 0$ for the case $\alpha = 9.24$ and $Fe^2 = 10^0, 10^4, 10^7$ using : (a) Backward Differentiation (BD) and Adams-Bashforth (AB) formulas; (b) Adams-Moulton (AM) and Adams-Bashforth (AB) formulas; and (c) fully explicit Adams-Bashforth (AB) formulas.

SCHEME	$Fe^2 = 10^0$	$Fe^2 = 10^4$	$Fe^2 = 10^7$
BD1/AB1	0.5000	0.7540×10^{-3}	0.2241×10^{-4}
BD1/AB2	0.2573	0.5253×10^{-3}	0.1605×10^{-4}
BD2/AB1	0.5144	0.7490×10^{-4}	0.7349×10^{-7}
BD2/AB2	0.2704	0.7352×10^{-3}	0.2240×10^{-4}

(a)

SCHEME	$Fe^2 = 10^0$	$Fe^2 = 10^4$	$Fe^2 = 10^7$
AM1/AB1	0.5000	0.7540×10^{-3}	0.2241×10^{-4}
AM1/AB2	0.2573	0.5253×10^{-3}	0.1605×10^{-4}
AM2/AB1	0.4885	0.7334×10^{-4}	0.7349×10^{-7}
AM2/AB2	0.2580	0.2578×10^{-3}	0.2650×10^{-5}

(b)

SCHEME	$Fe^2 = 10^0$	$Fe^2 = 10^4$	$Fe^2 = 10^7$
AB1/AB1	0.4981×10^{-2}	0.3676×10^{-4}	0.3674×10^{-7}
AB2/AB2	0.2491×10^{-2}	0.1947×10^{-3}	0.2095×10^{-5}
AB3/AB3	0.1359×10^{-2}	0.2537×10^{-3}	0.8195×10^{-5}

(c)

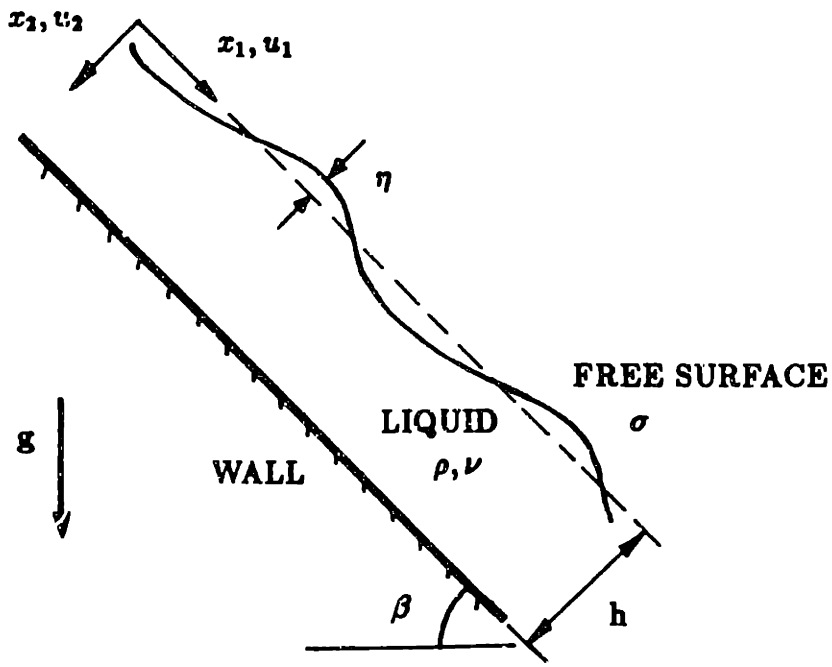

(a)

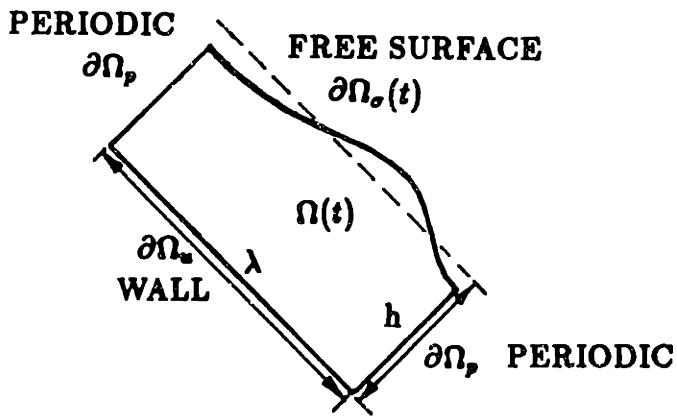

(b)

FIGURE 2-1 Flow of a thin film down an inclined plane :
(a) problem description; and
(b) computational domain.

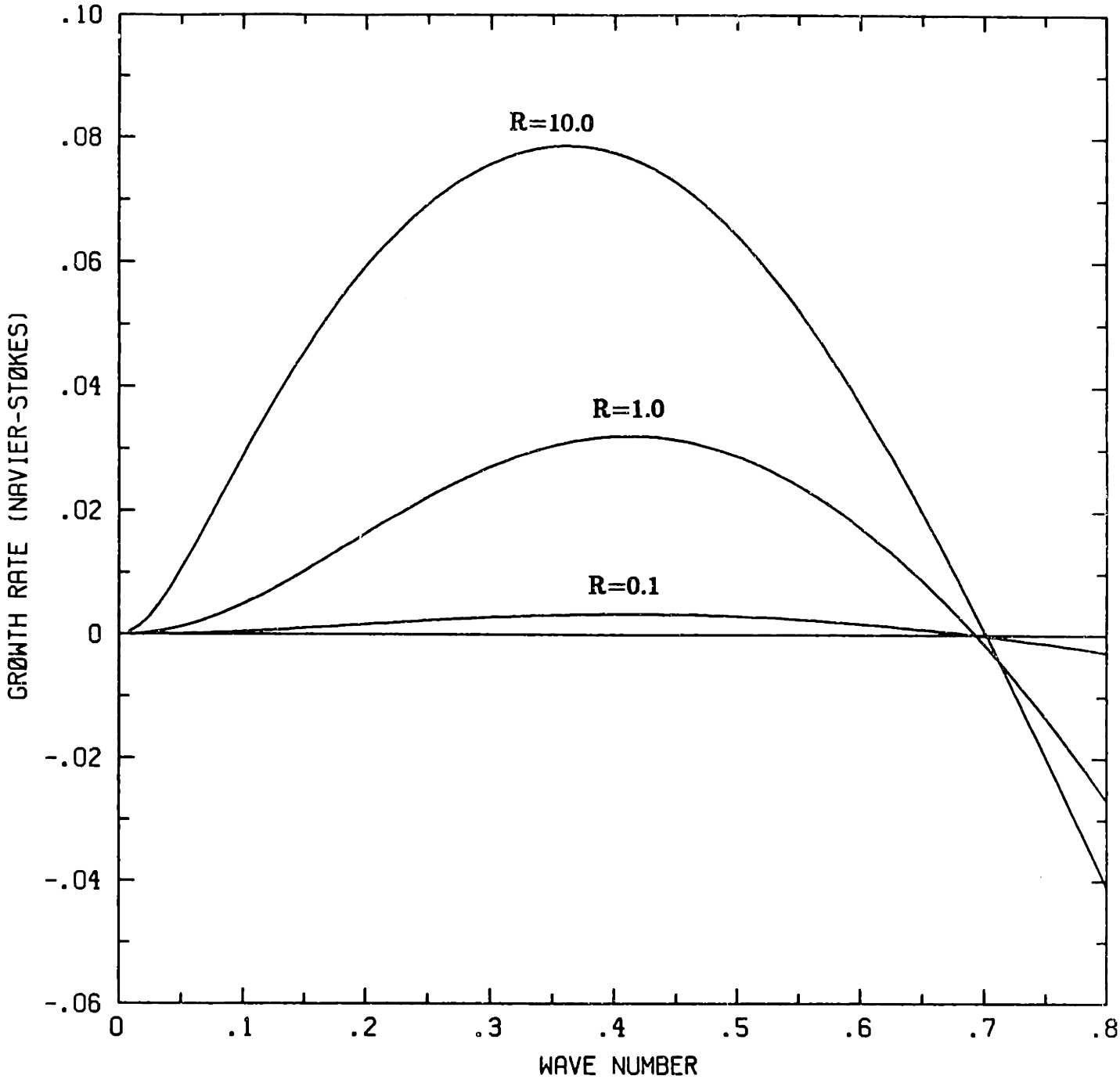

FIGURE 2-2 Linearized stability analysis of vertically falling films : growth rate versus wave number for W=1.0; R=0.1, 1.0, 10.0.

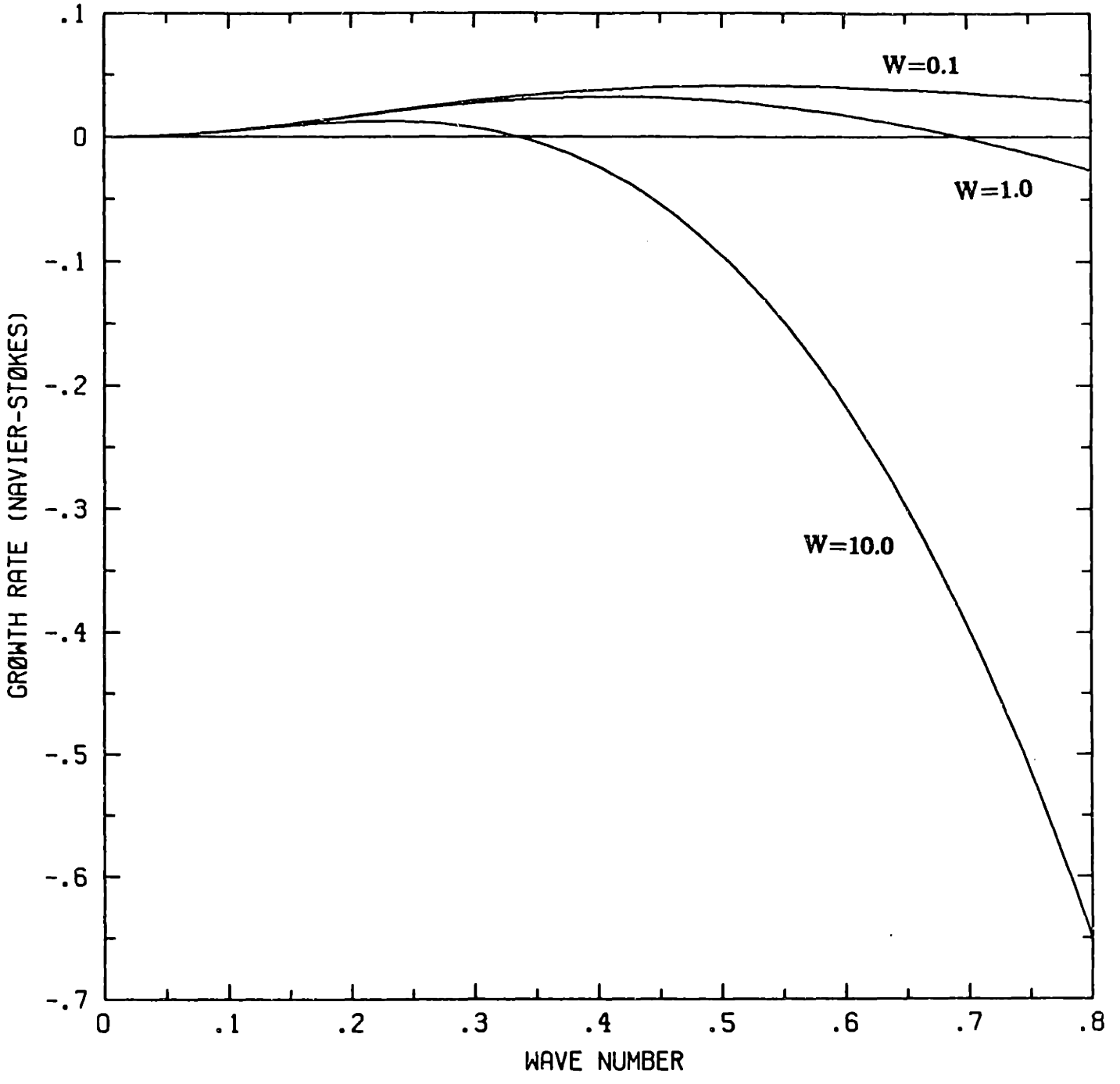

FIGURE 2-3 Linearized stability analysis of vertically falling films : growth rate versus wave number for R=1.0; W=0.1, 1.0, 10.0.

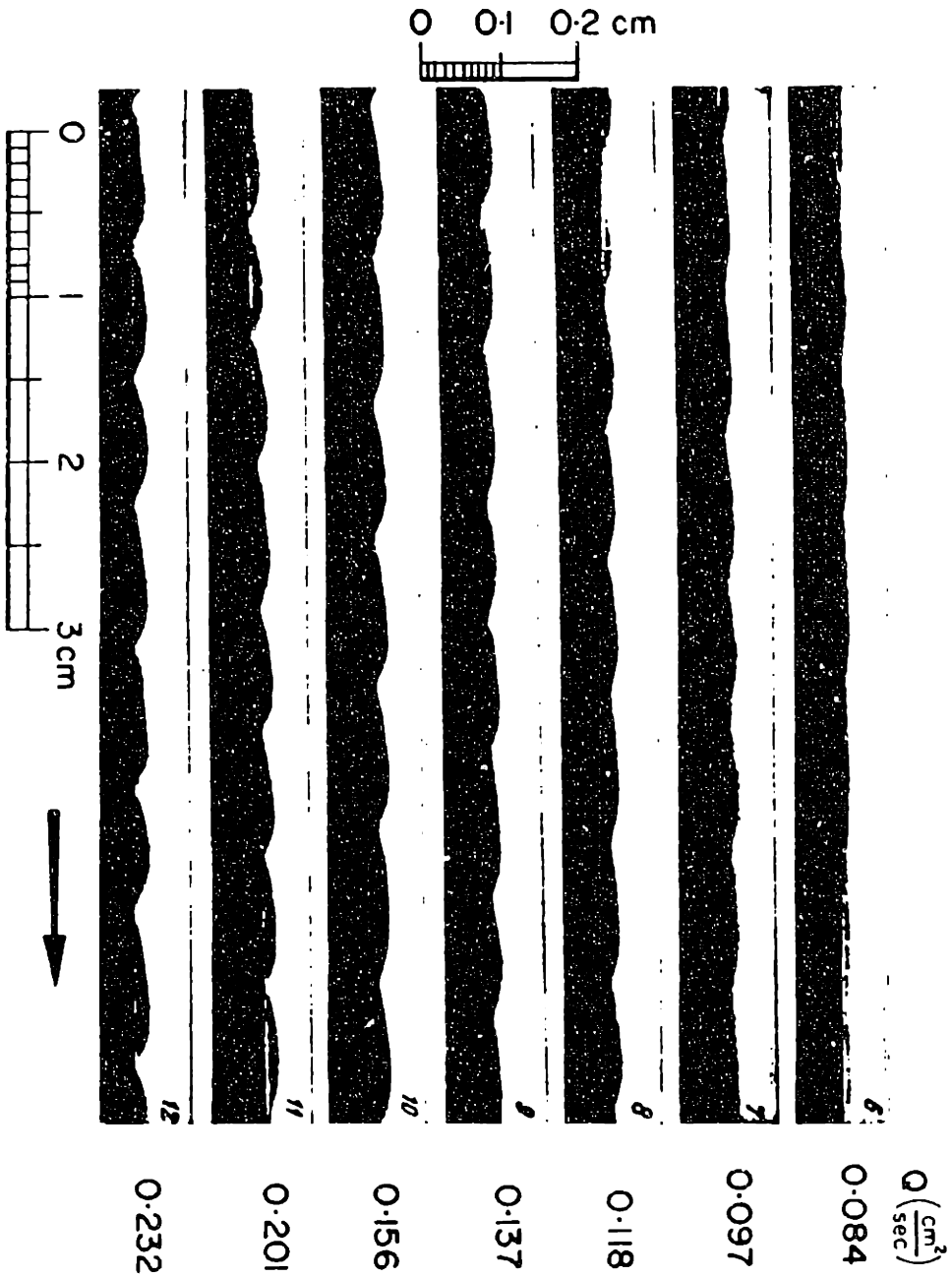

FIGURE 2-4 Supercritically stable steady-periodic waves in vertically falling films : periodic ripples.

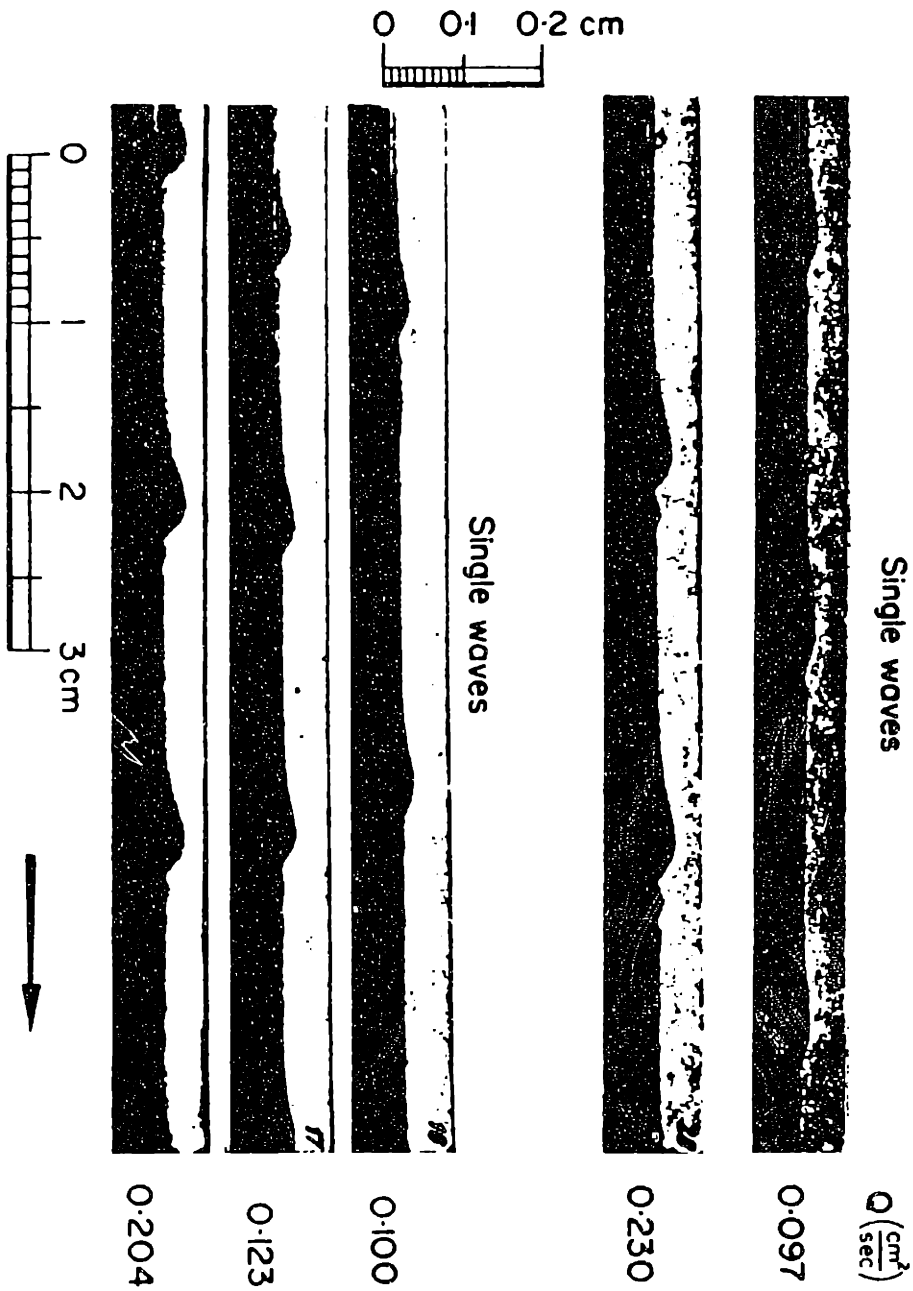

FIGURE 2-5 Supercritically stable steady-periodic waves in vertically falling films : single-waves.

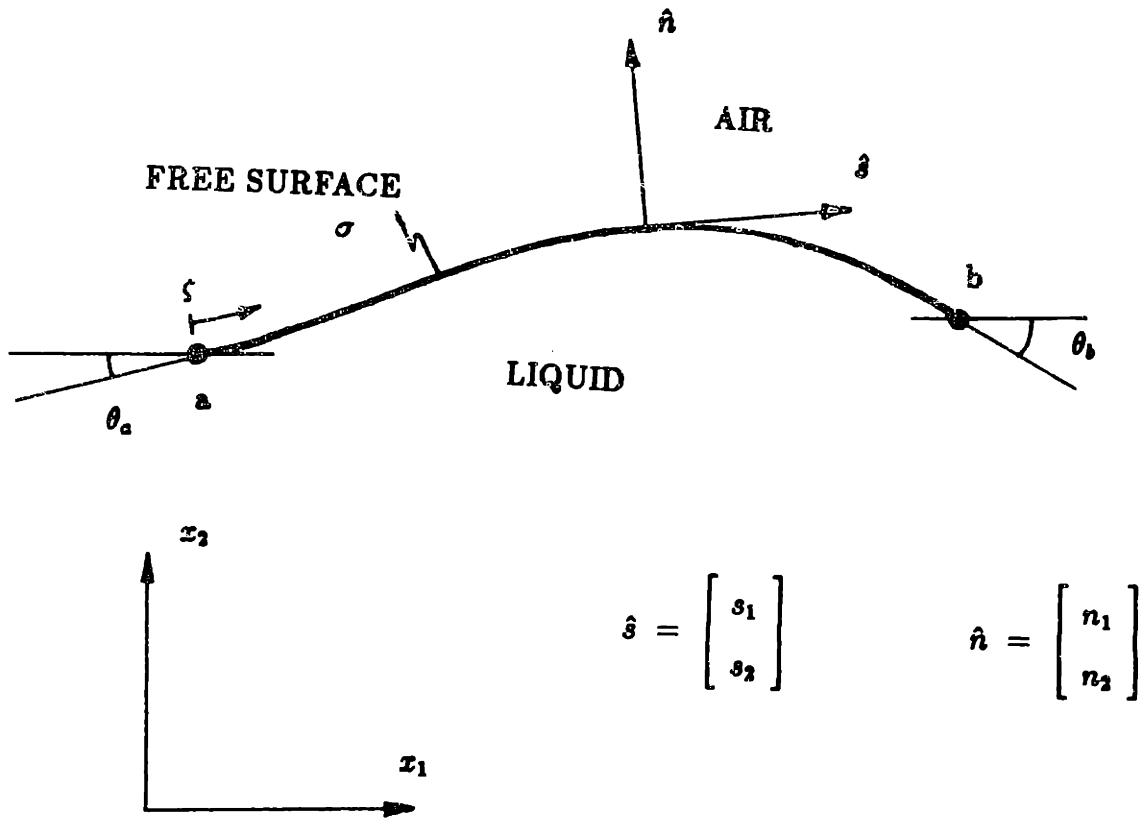

FIGURE 3-1 Planar free-surface geometry.

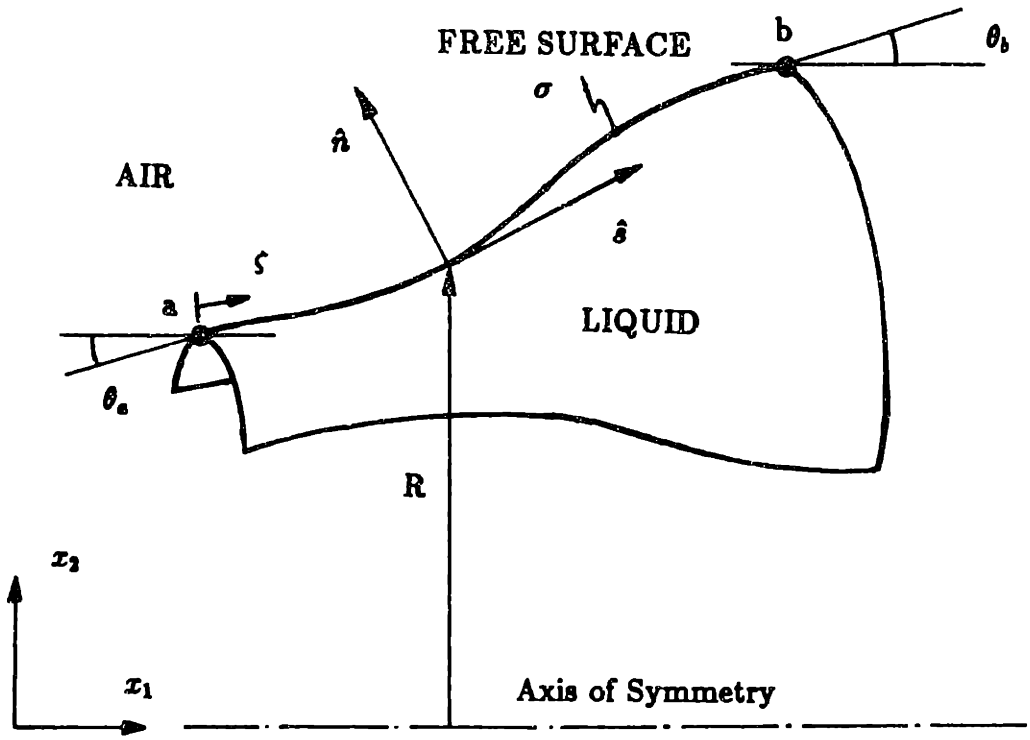

$$\hat{n} = \begin{bmatrix} n_1 \\ n_2 \end{bmatrix} \qquad \hat{s} = \begin{bmatrix} s_1 \\ s_2 \end{bmatrix}$$

FIGURE 3-2 Axisymmetric free-surface geometry.

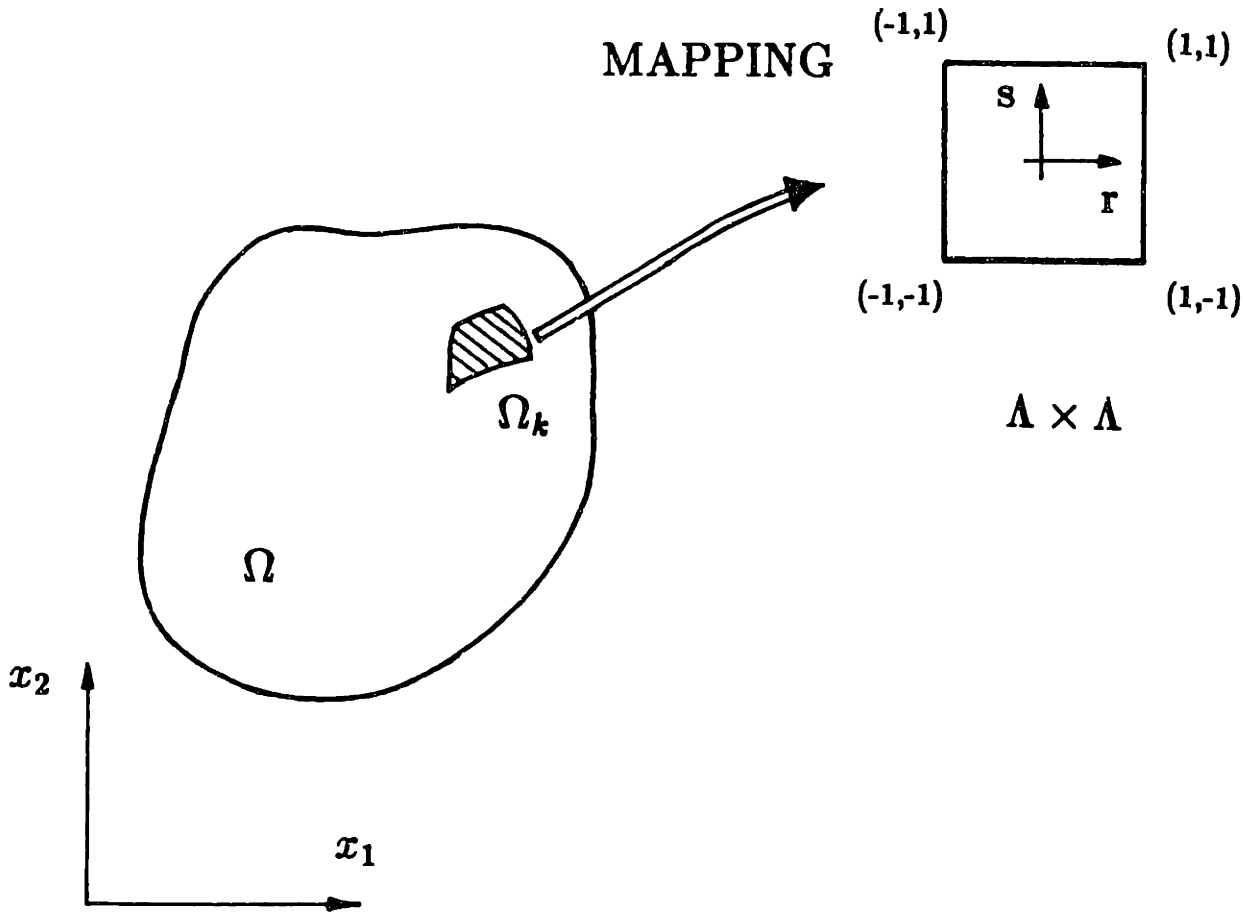

FIGURE 4-1 Mapping of the physical (x_1, x_2) coordinate system to a local (r,s) system.

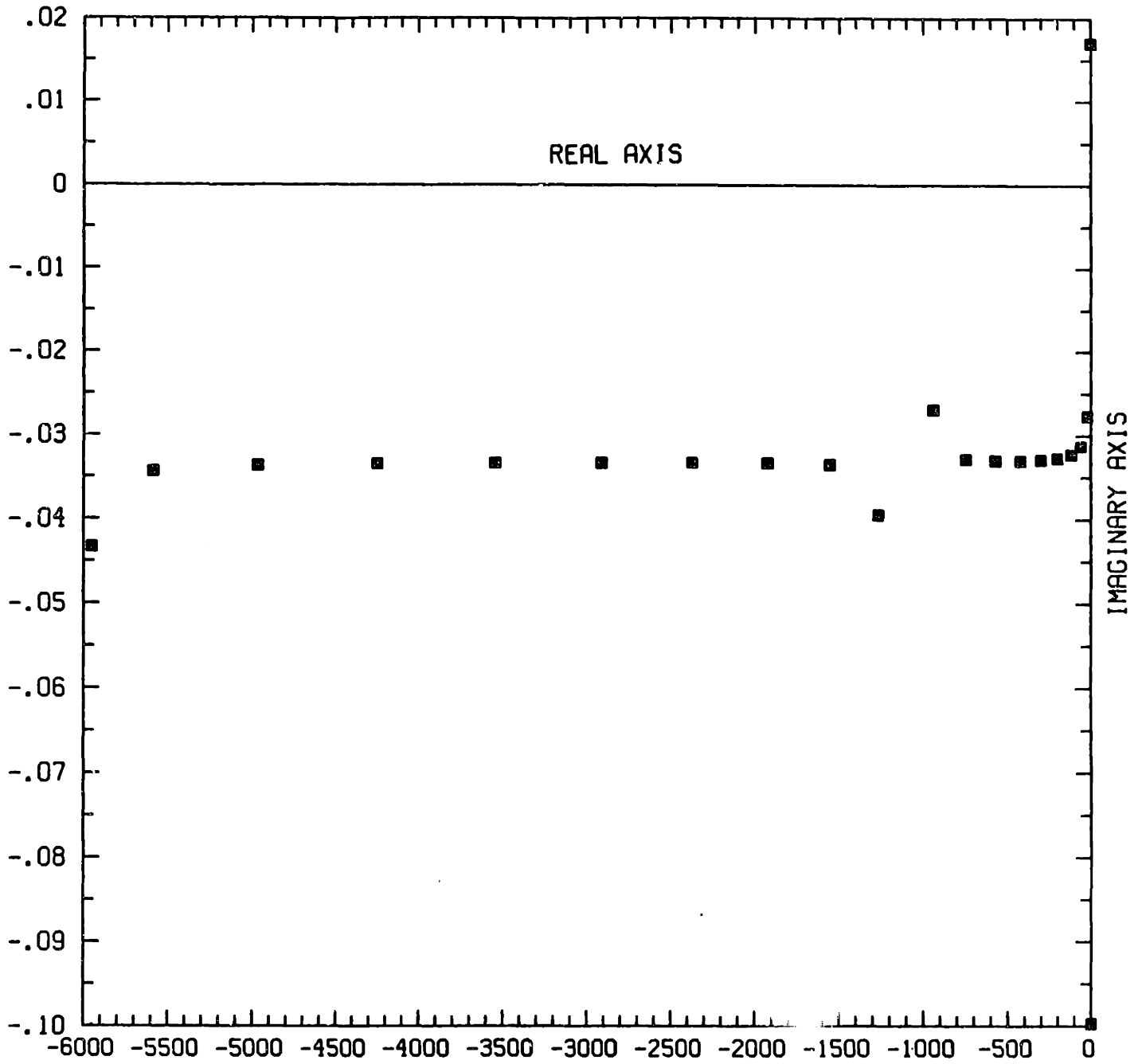

FIGURE 5-1 Eigenvalue spectrum of linearized stability analysis of vertically falling films : $\alpha = 0.05$, $R = 1.0$, $W = 100$.

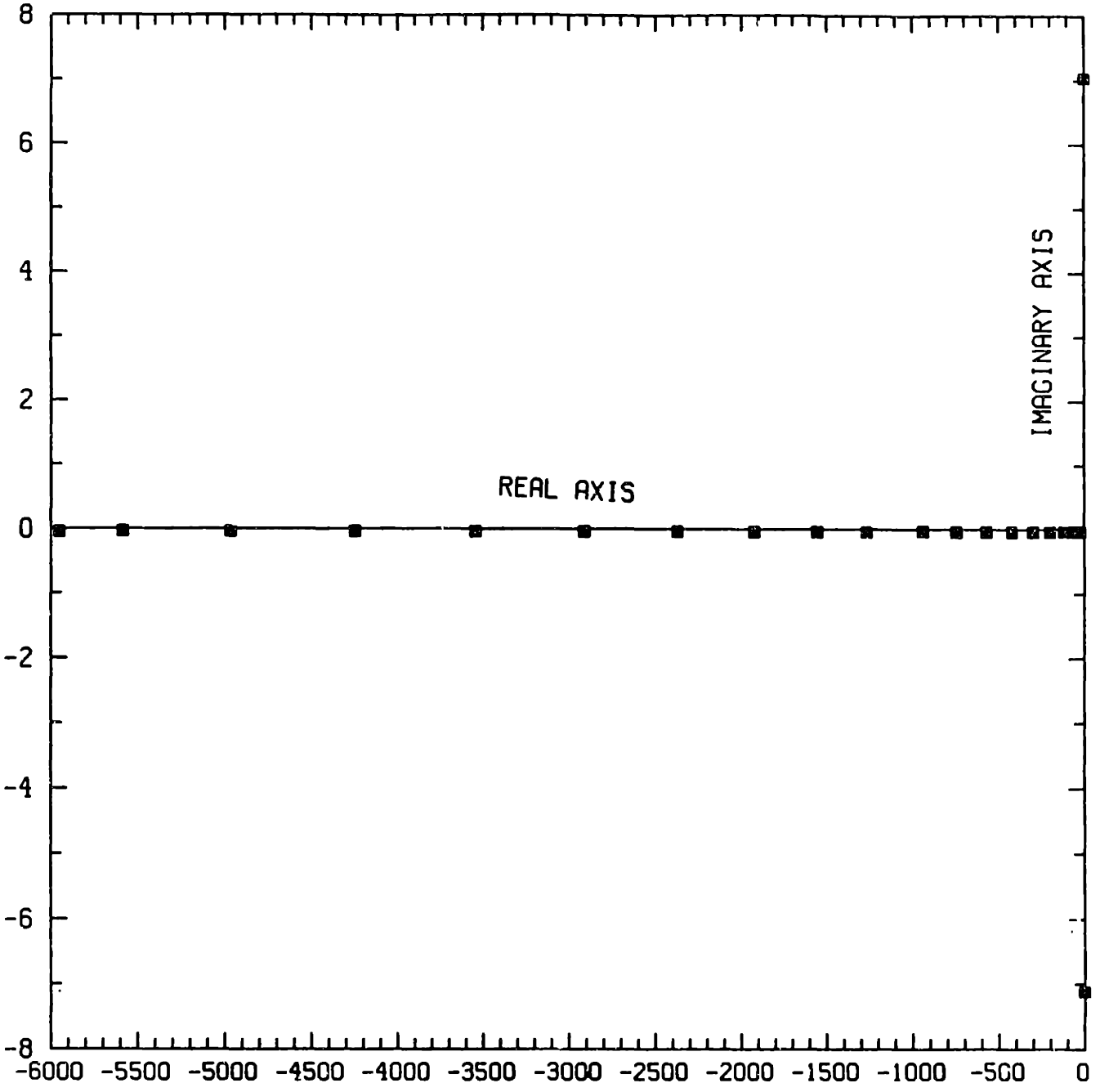

FIGURE 5-2 Eigenvalue spectrum of linearized stability analysis of vertically falling films : $\alpha = 0.05$, $R = 1.0$, $W = 10^7$.

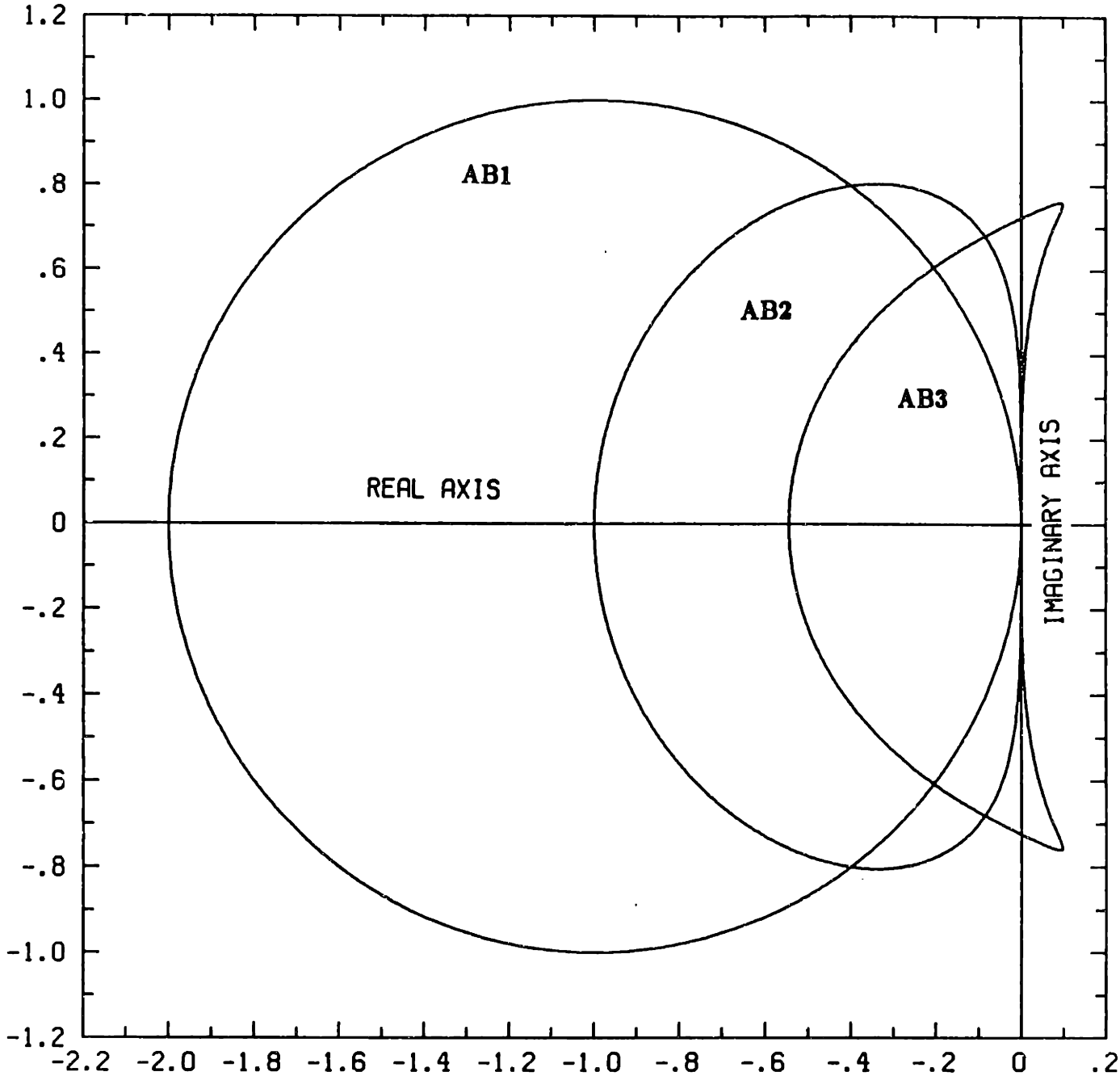

FIGURE 5-3 Stability regions for first-, second- and third-order Adams-Bashforth formulas.

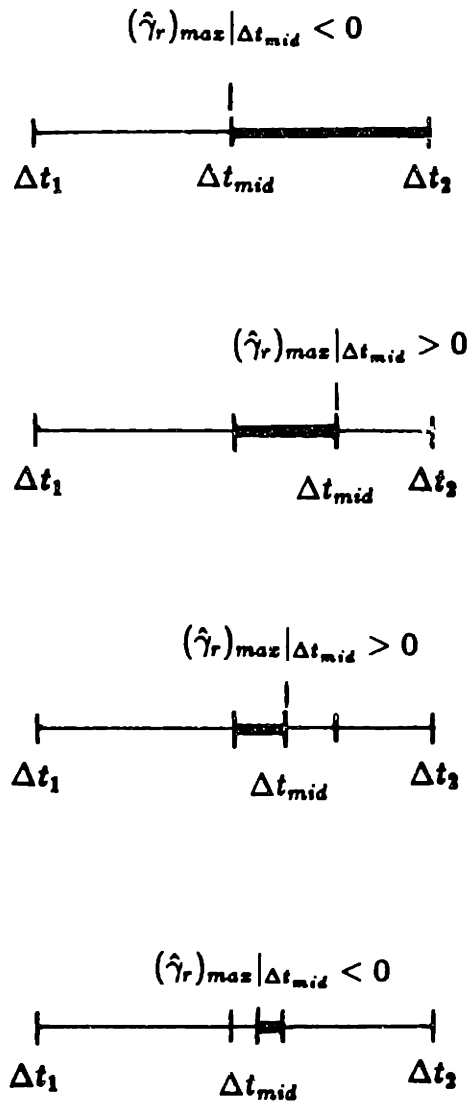

Initial interval is selected such that $\Delta t_1 < \Delta t_{cr} < \Delta t_2$

FIGURE 5-4 Illustrative example of critical step size evaluation using a bisection method.

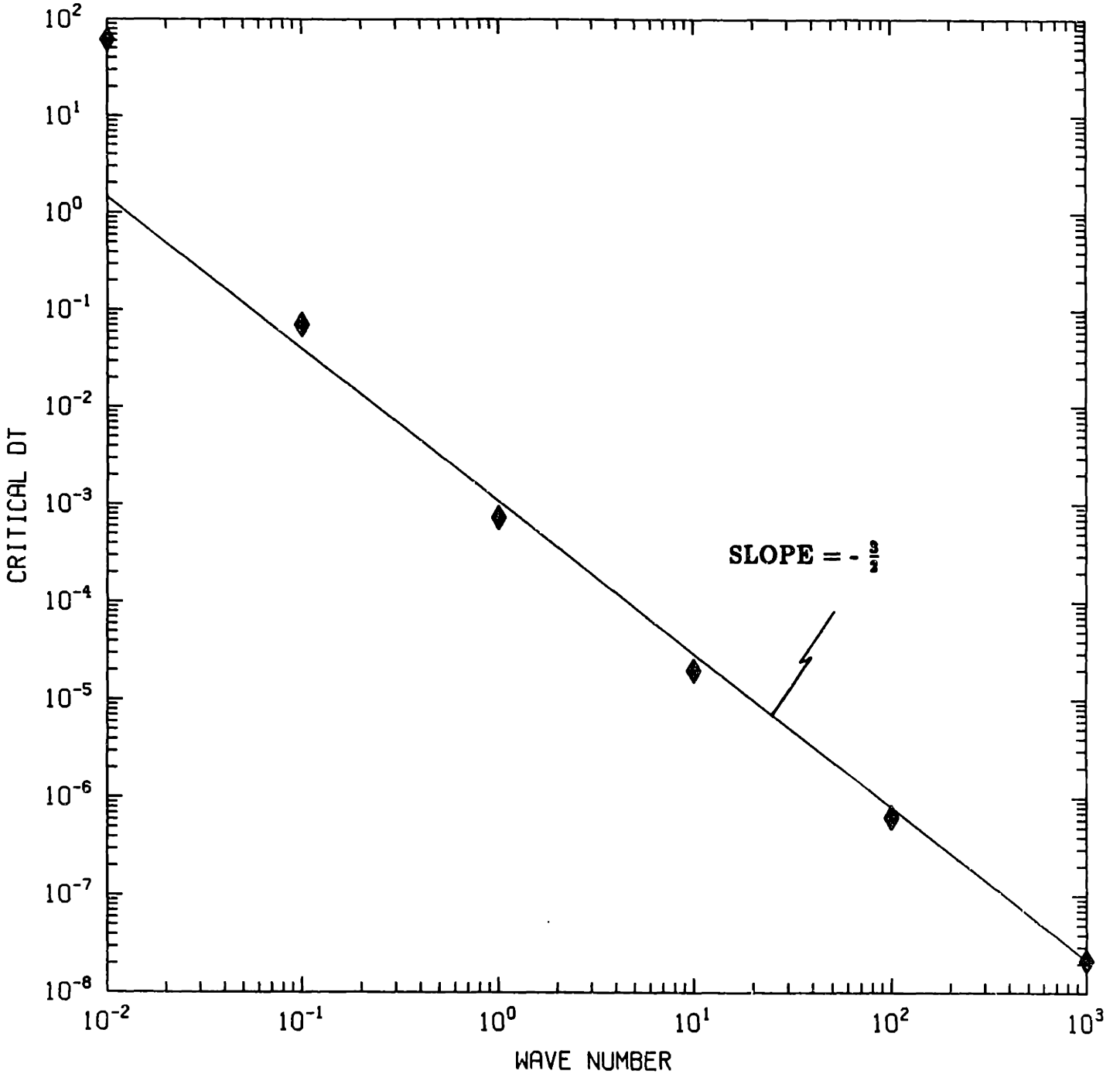

FIGURE 5-5 Discrete Orr-Sommerfeld Operator : Critical step size versus wave number for $Fe^2 = 10^7$.

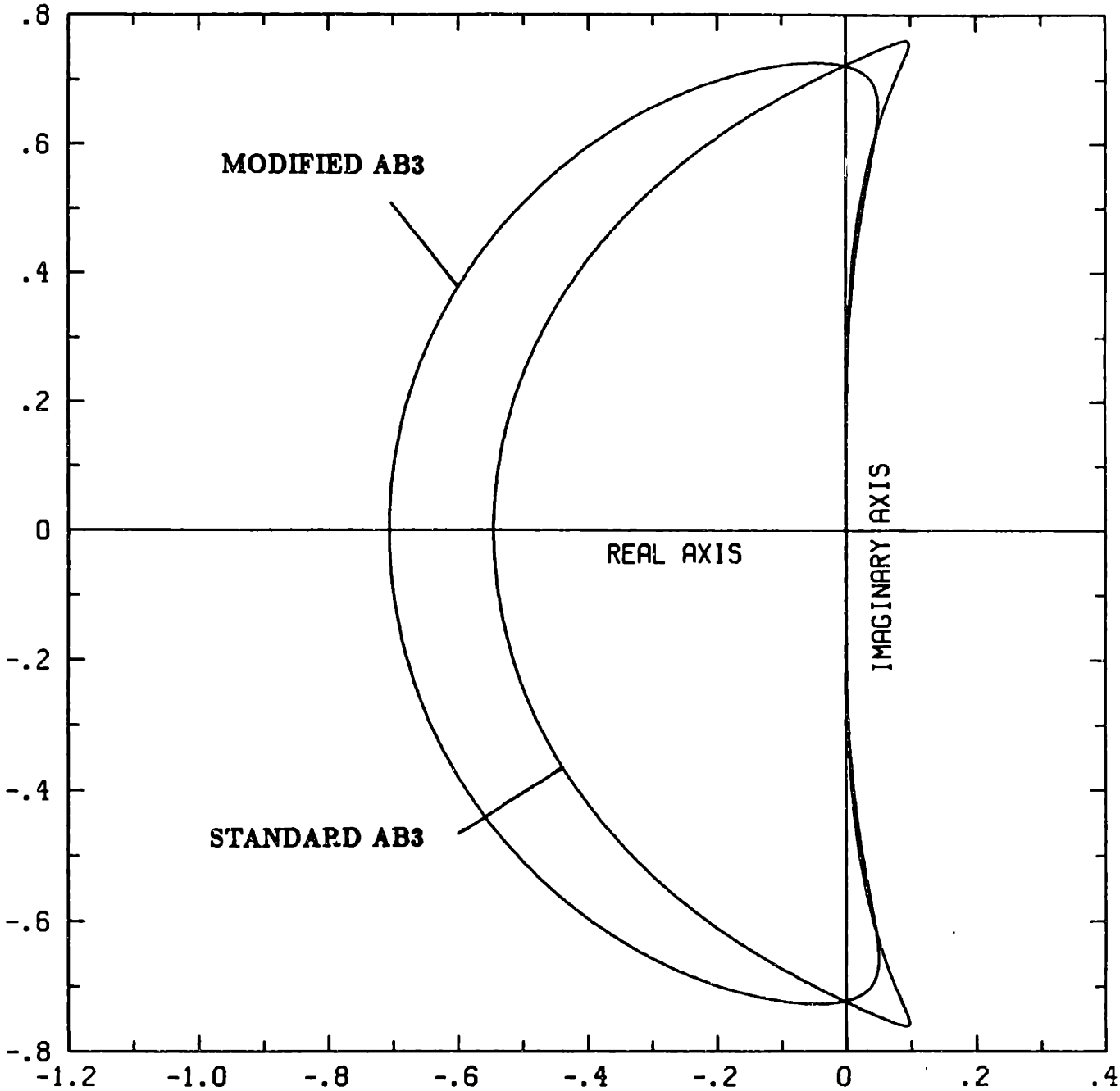

FIGURE 5-6 A comparison of the stability regions of modified and standard third-order Adams-Bashforth formulas.

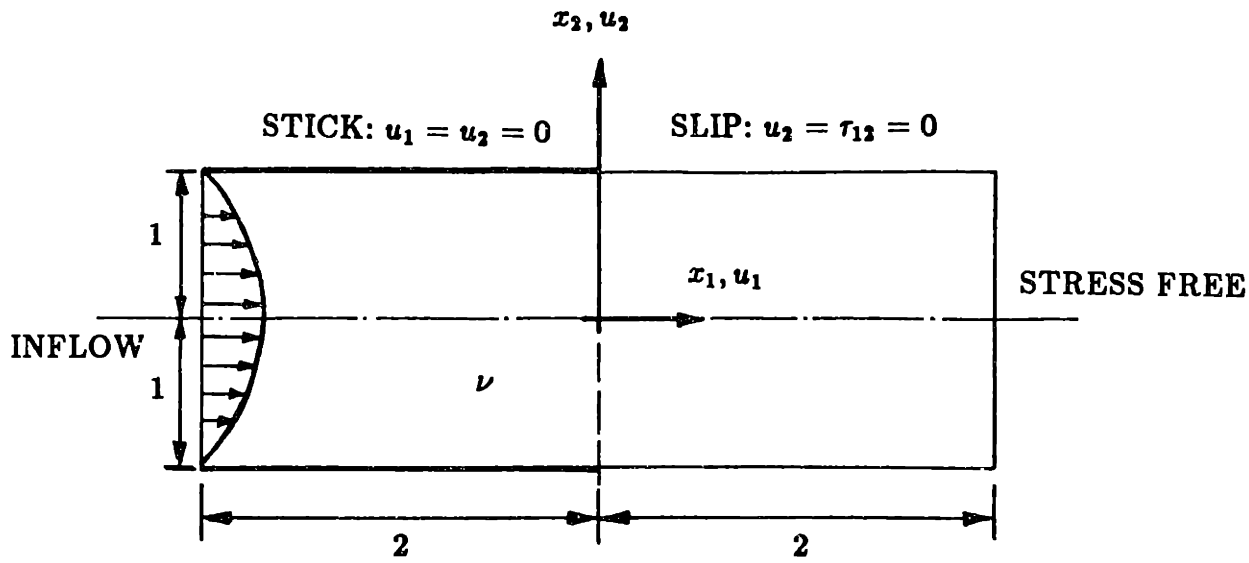

PROBLEM DESCRIPTION

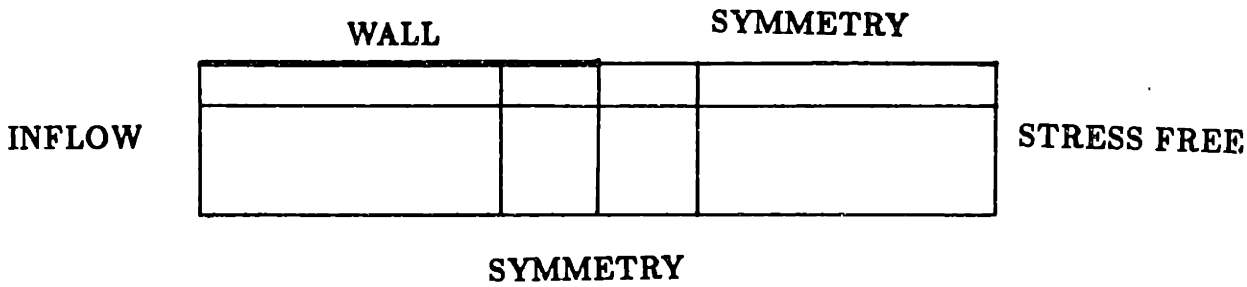

SPECTRAL ELEMENT MODEL (K=8,N=4)

FIGURE 7-1 The stick-slip problem : geometry, boundary conditions and spectral element model.

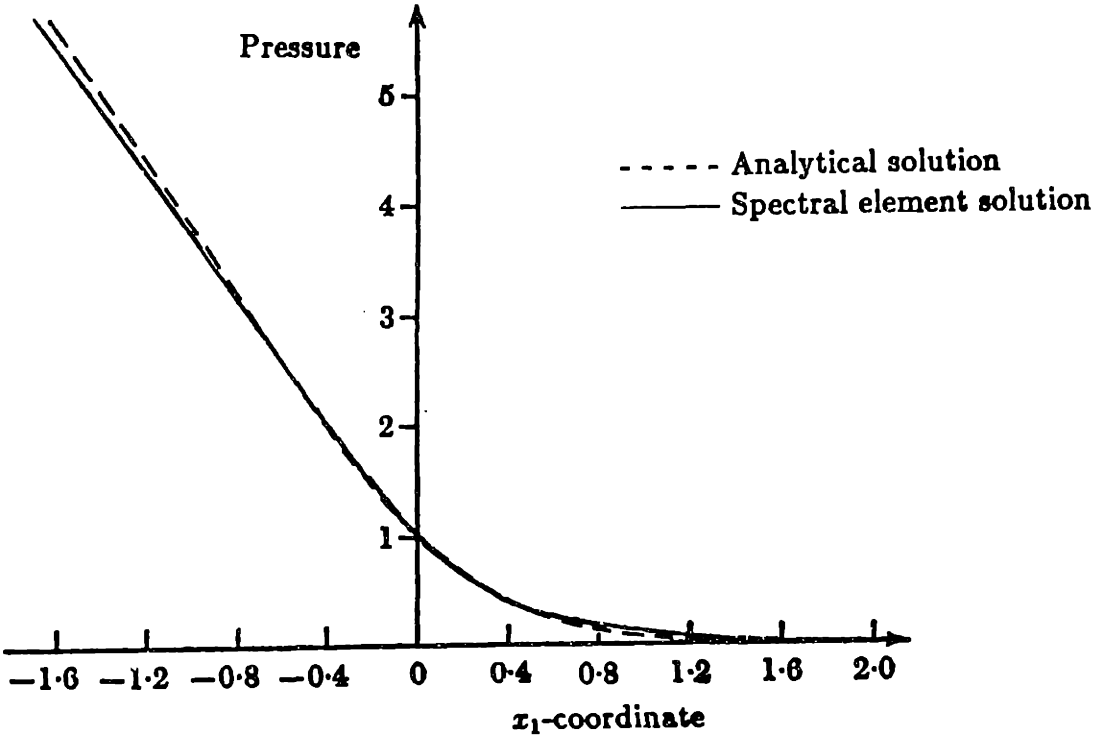

FIGURE 7-2 The stick-slip problem : pressure dustribution along the center line.

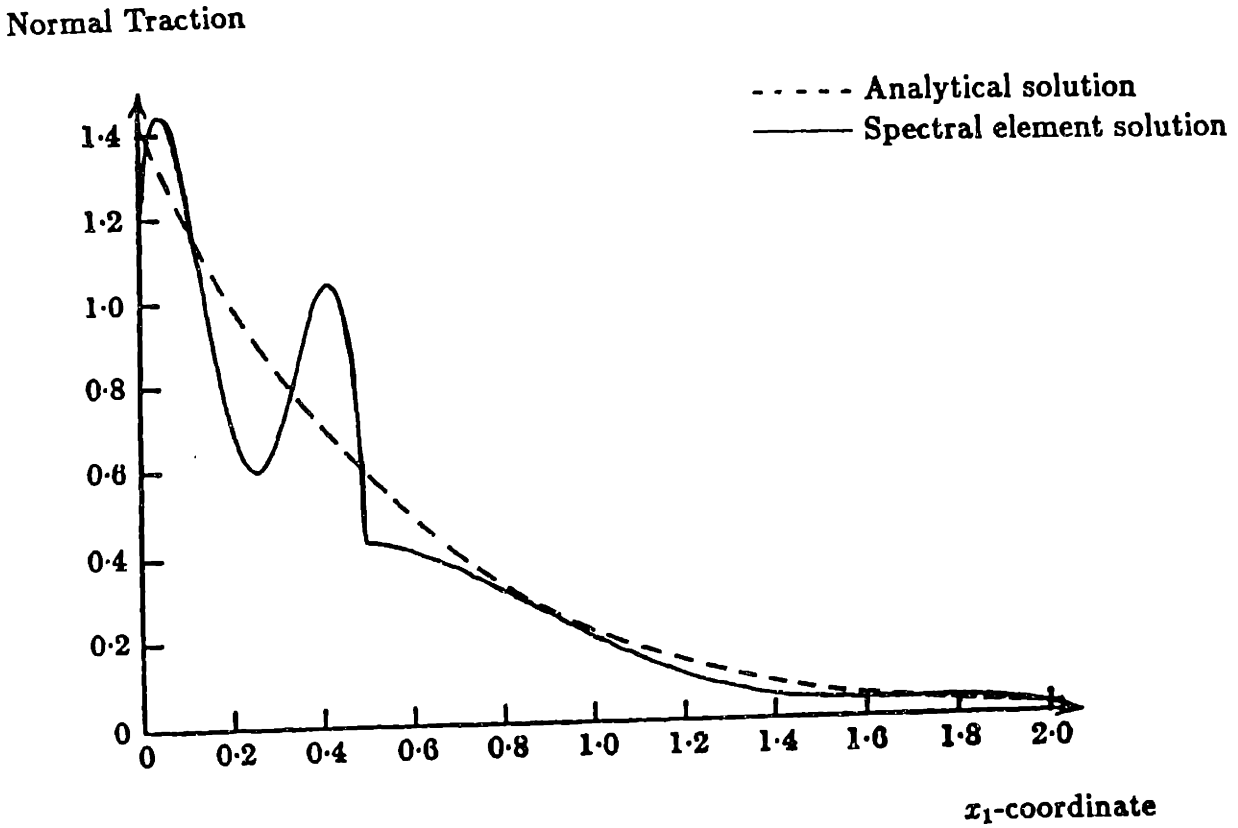

FIGURE 7-3 The stick-slip problem : normal-traction distribution along the slip boundary.

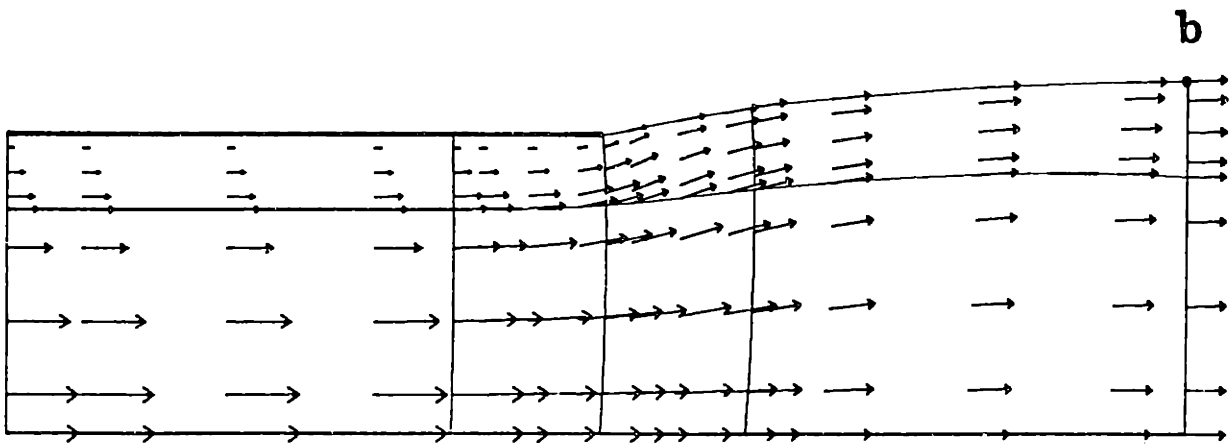

FIGURE 7-4 The die-swell problem : velocity field at steady-state.

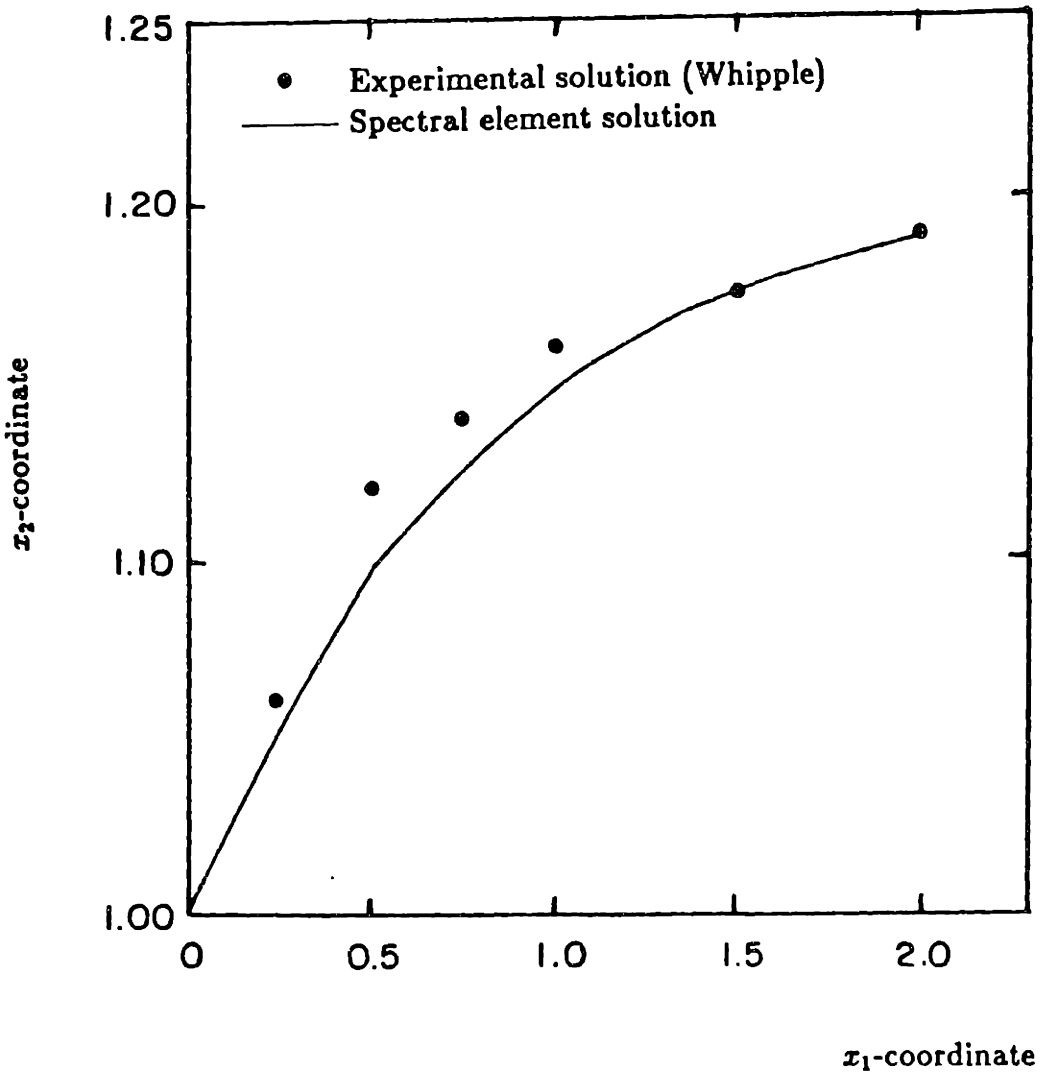

FIGURE 7-5 The die-swell problem : free-surface position at steady-state.

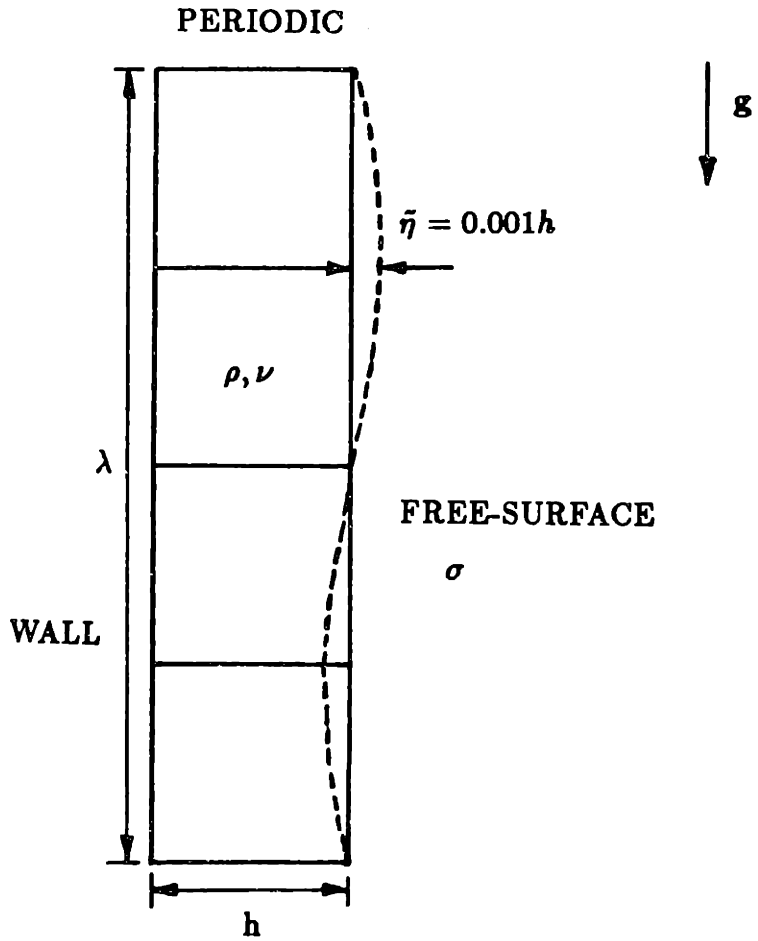

K=4, N=6

FIGURE 7-6 Vertically falling film : spectral element model for stability analysis under infinitesimal perturbation.

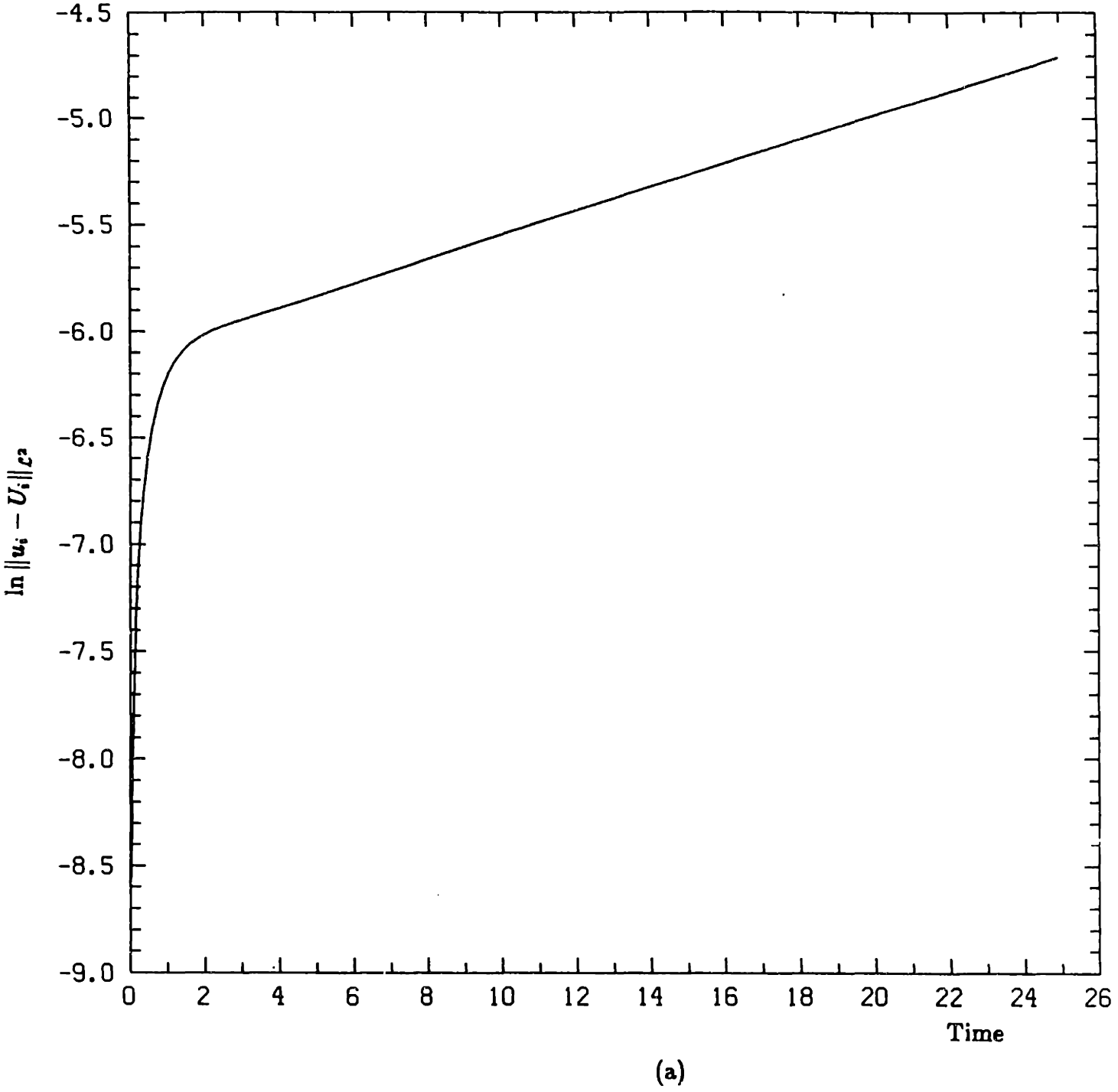

FIGURE 7-7 Spectral element linearized stability analysis of vertically falling films: (a) time-history plot of the logarithm of the $\mathcal{L}^2$-norm of the velocity perturbation; and (b) time-history plot of the x_2-coordinate of a typical point at fixed x_1-coordinate on the free surface.

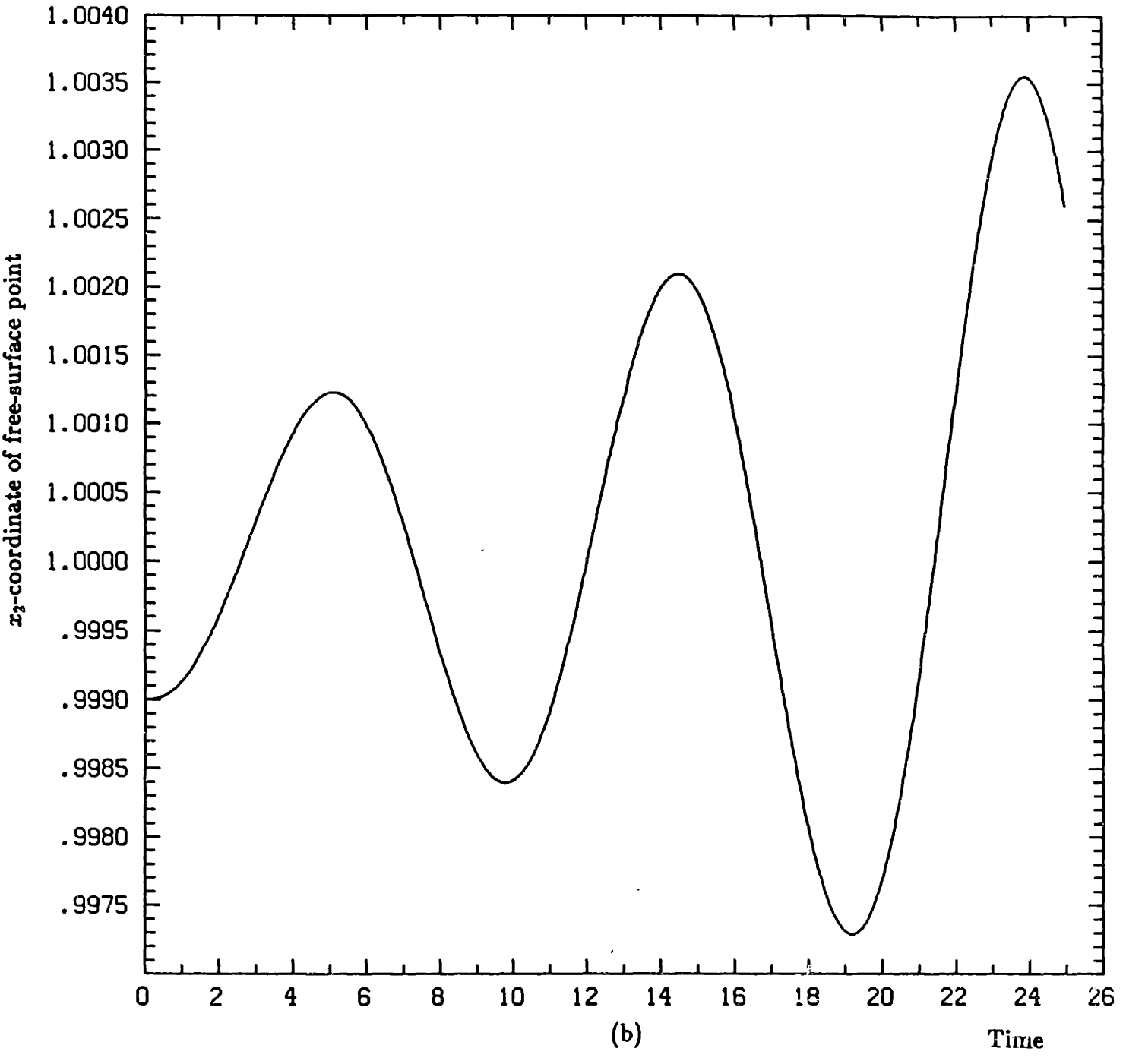

FIGURE 7-7 Continued.

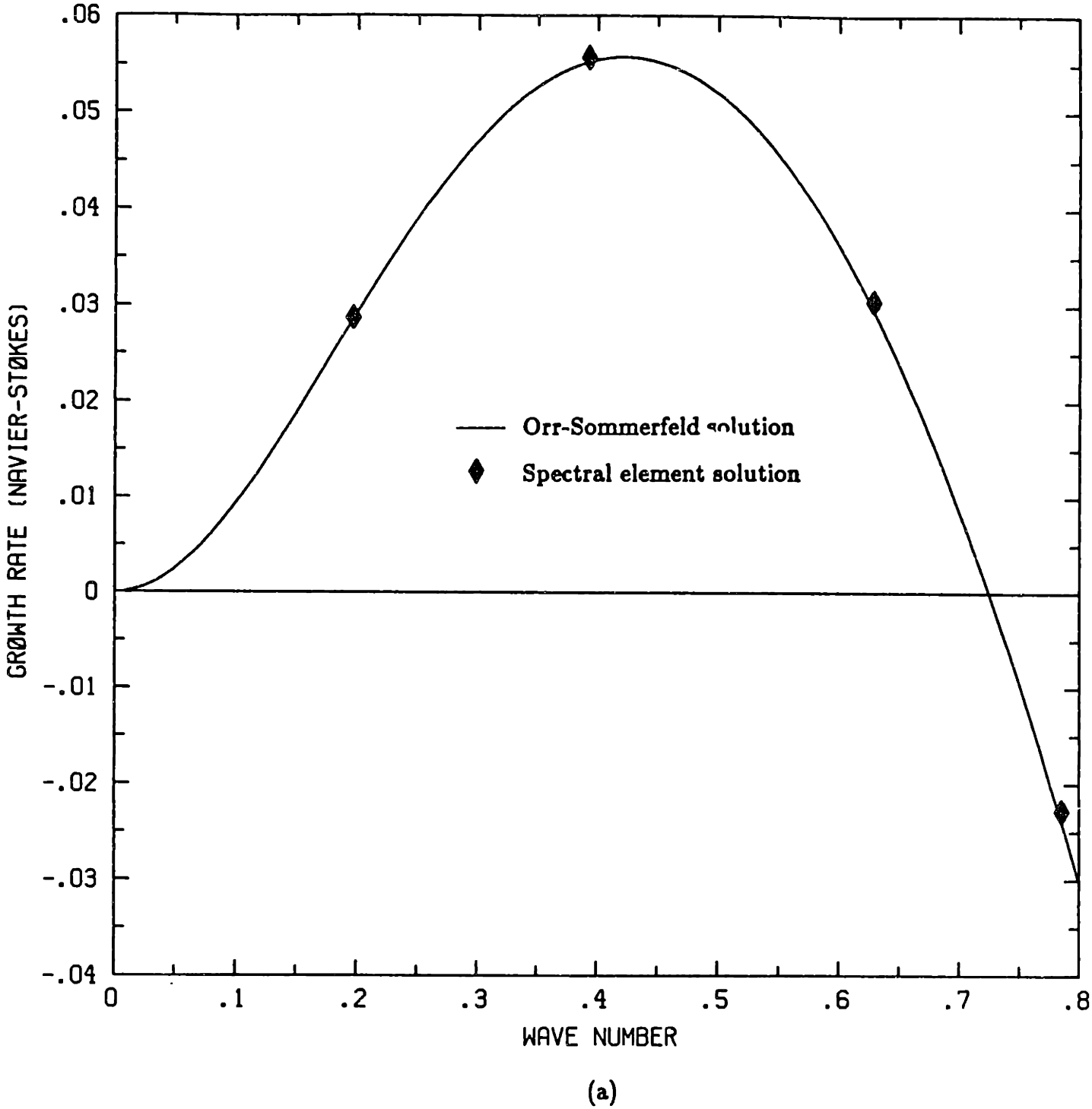

FIGURE 7-8 Spectral element linearized stability analysis of vertically falling films at R=1.935 and W=0.844 :
(a) growth rate versus wave number; and
(b) wave speed versus wave number.

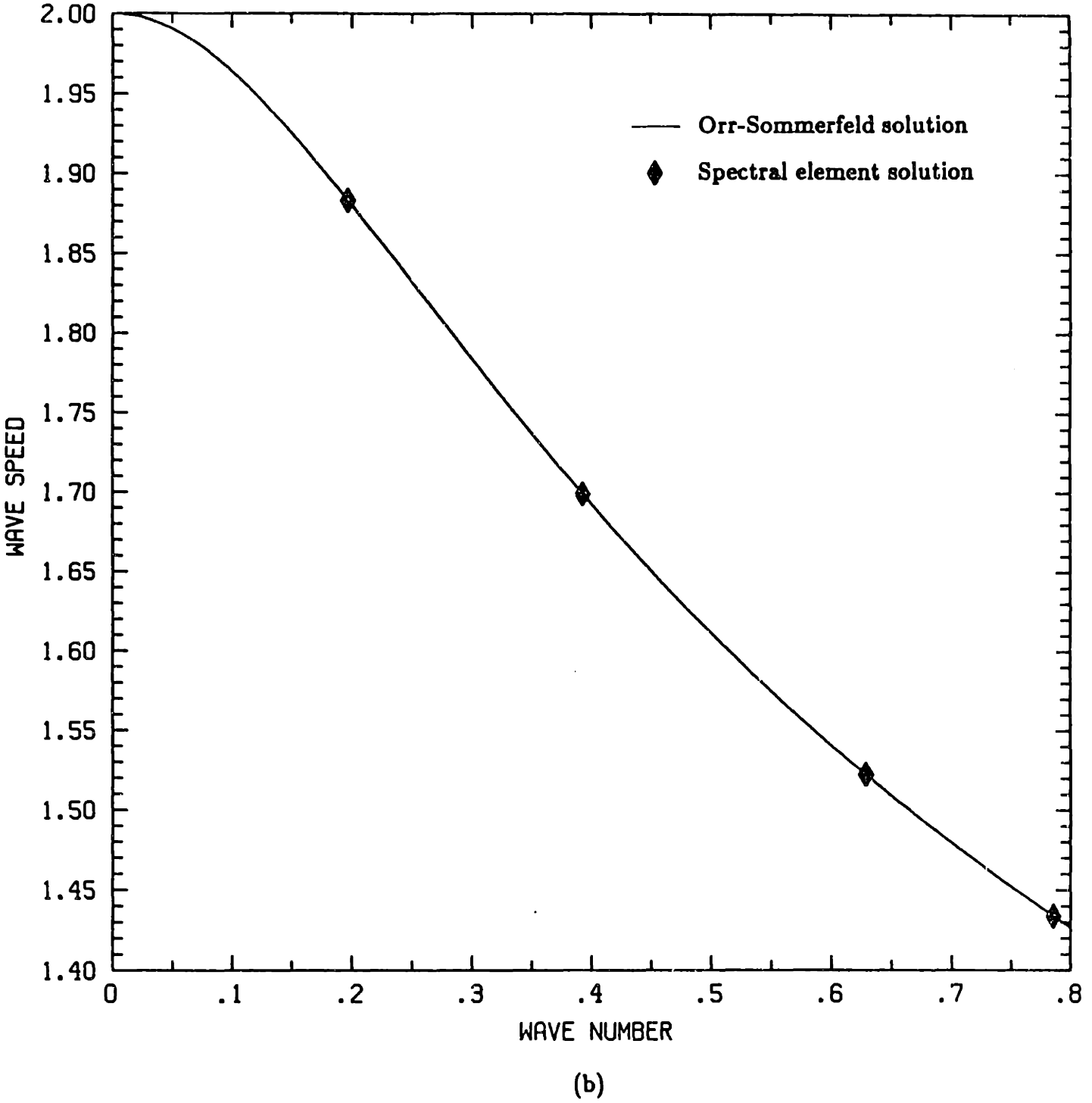

(b)

FIGURE 7-8 Continued.

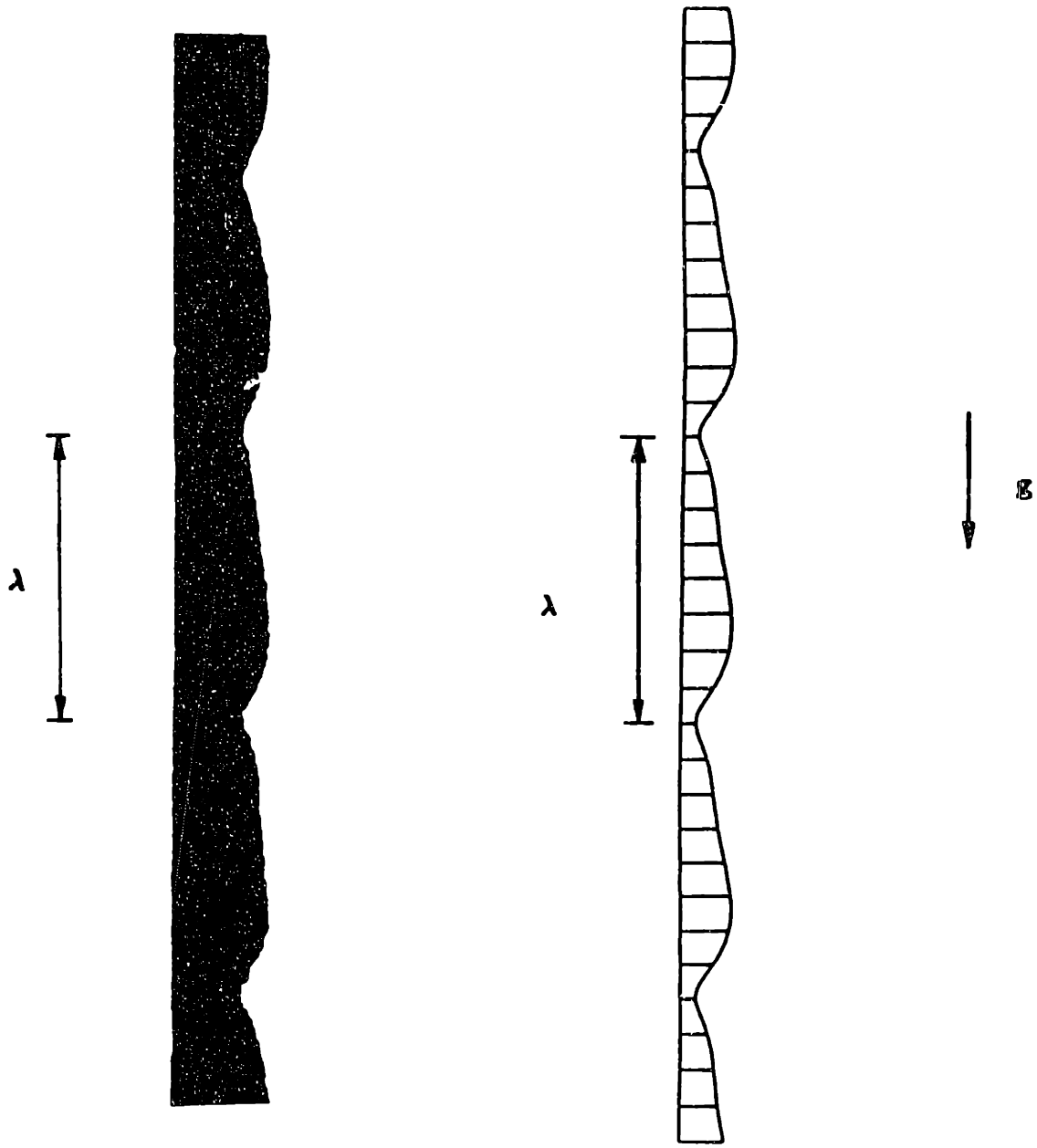

EXPERIMENTAL RESULT

NUMERICAL RESULT

FIGURE 7-9 Comparison of spectral element and experimental results of supercritically stable steady-periodic wave profile of vertically falling film: periodic ripples for $\alpha = 0.14$, R=30.0 and W=14.7.

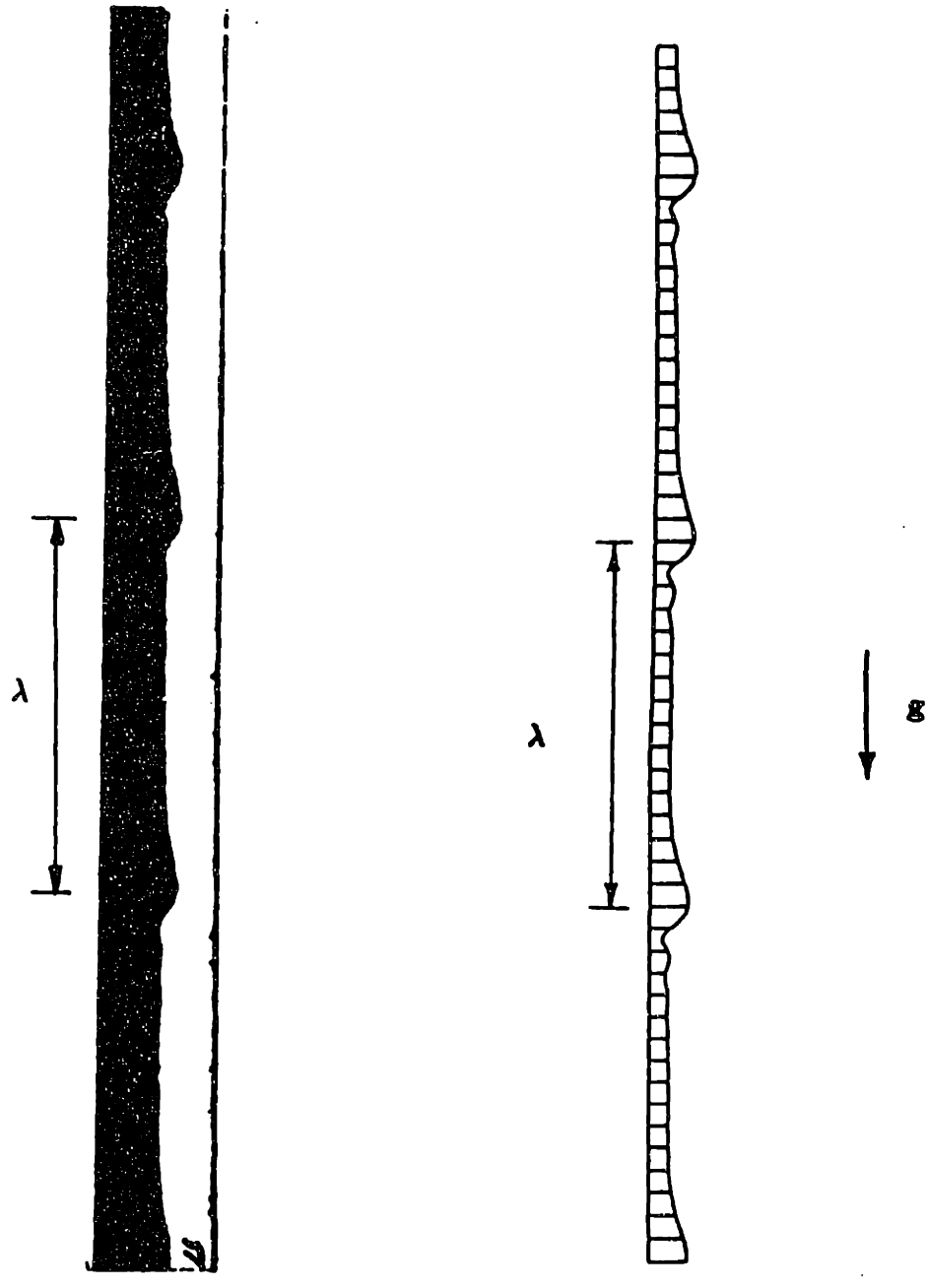

EXPERIMENTAL RESULT

NUMERICAL RESULT

FIGURE 7-10 Comparison of spectral element and experimental results of supercritically stable steady-periodic wave profile of vertically falling film: single-waves for $\alpha = 0.07$, R=9.1 and W=16.8.

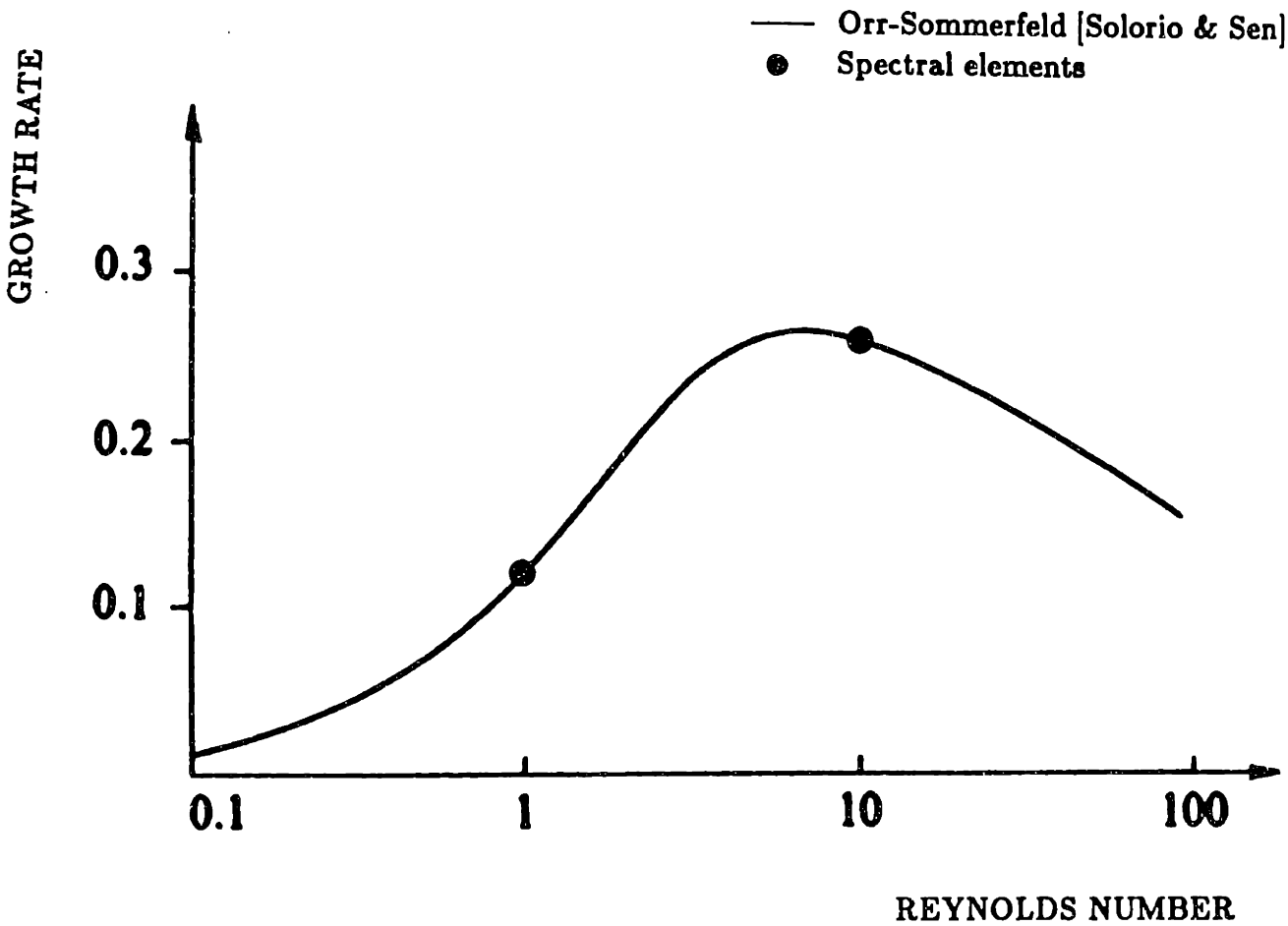

FIGURE 7-11 Spectral element linearized stability analysis of vertically falling cylindrical films: growth rate versus Reynolds number for Weber number W=1.

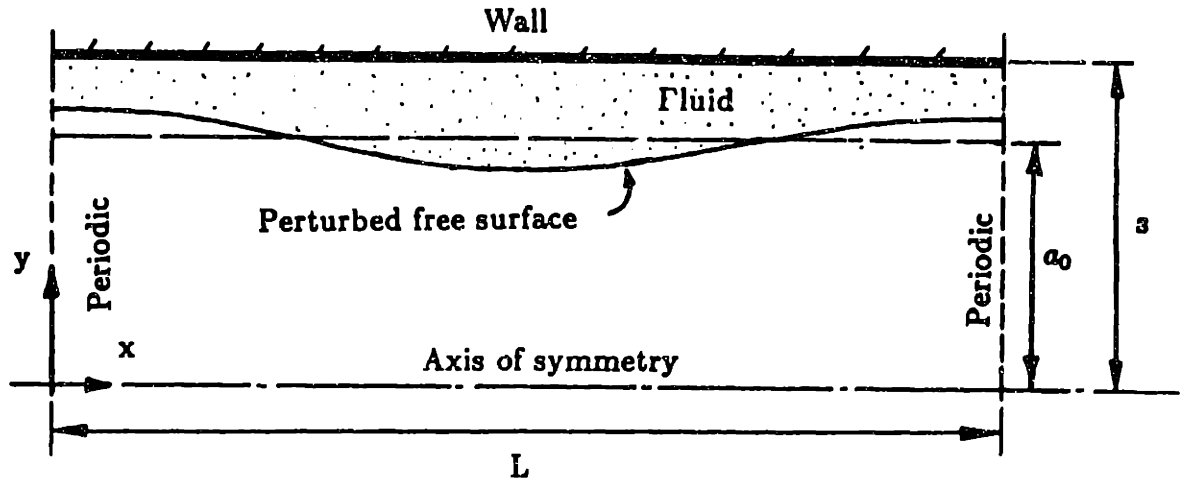

FLUID PROPERTIES

$\rho = 1.00\ g/cm^3$

$\sigma = 20.00\ dynes/cm$

$\mu = 0.01\ g/cm - sec$

DIMENSIONS

$L = 0.150\ cm$

$s = 0.025\ cm$

$a_0 = 0.020\ cm$

PERTURBATION

$$a\,|_{t=0} = a_0[1 + \varepsilon cos(\,2\pi x/L\,)]$$

$$\varepsilon = 0.01$$

FIGURE 7-12 Analysis of tube closure due to capillary instability : film geometry, boundary conditions and fluid properties.

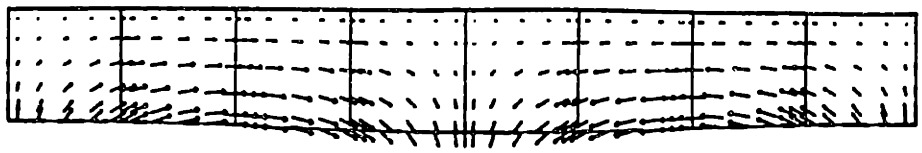

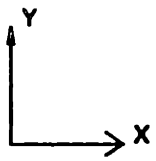

(a)

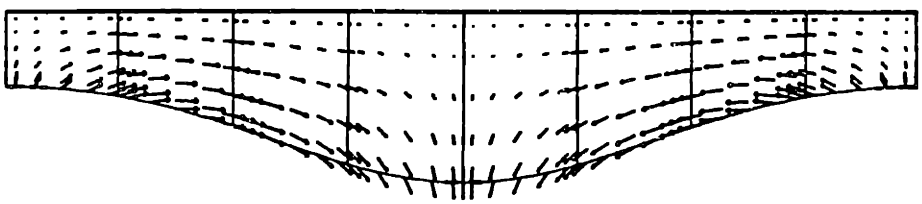

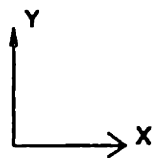

(b)

FIGURE 7-13 Spectral element solution of tube closure due to capillary instability: velocity plots for (a) t=2.00 × 10^{-3} s; (b) t=2.60 × 10^{-2} s; (c) t=4.20 × 10^{-2} s; and (d) t=4.51 × 10^{-2} s.

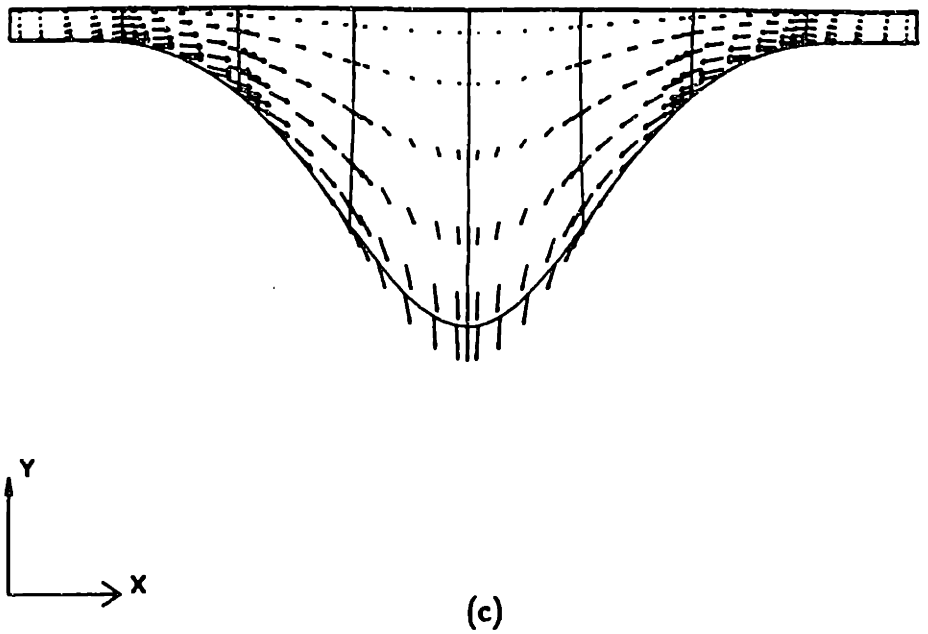

(c)

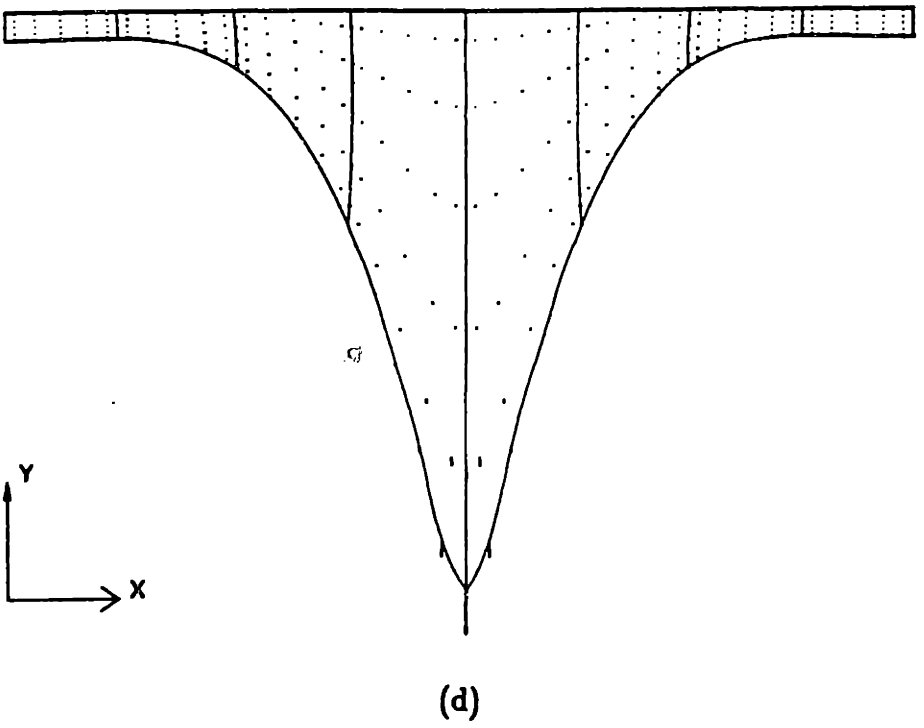

(d)

FIGURE 7-13 Continued.

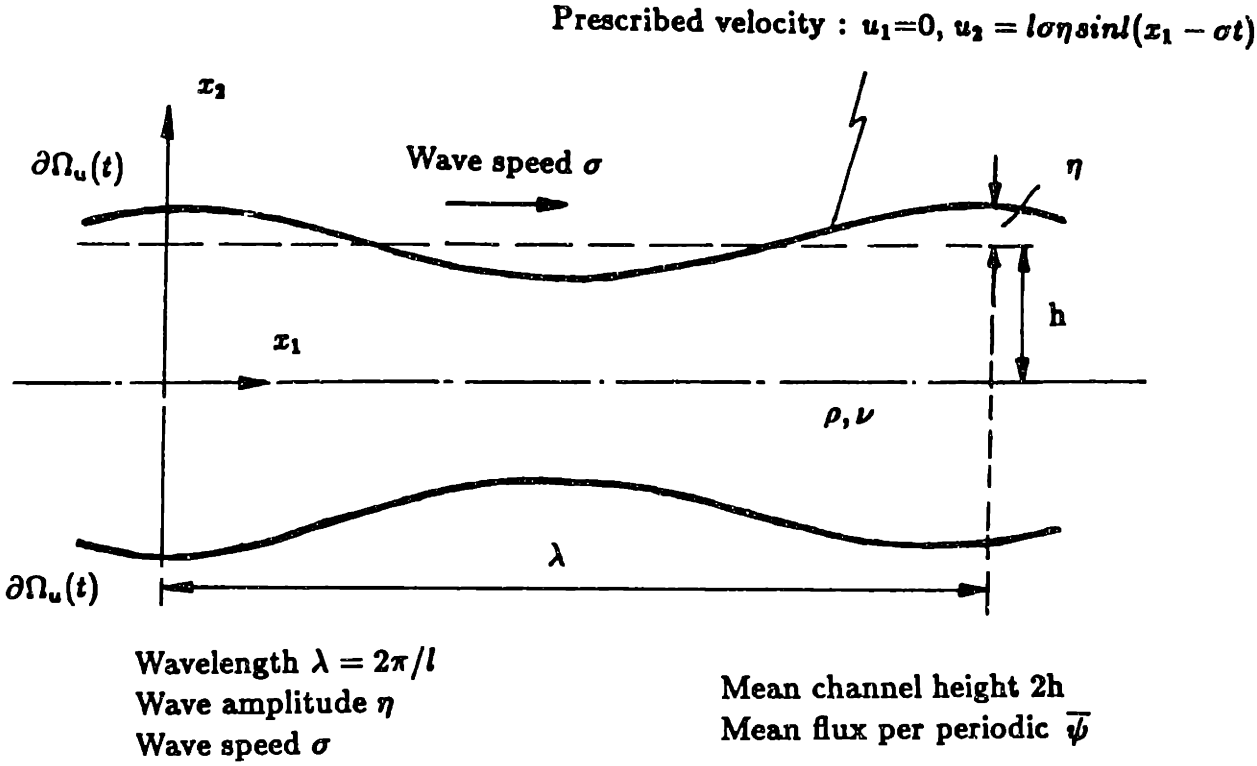

FIGURE 8-1 Planar peristaltic flow: (a) problem description; and (b) spectral element model.

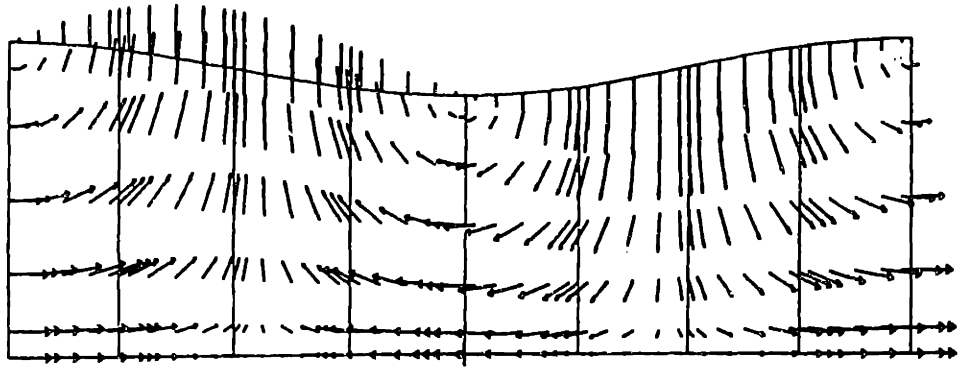

SPECTRAL ELEMENT SOLUTION

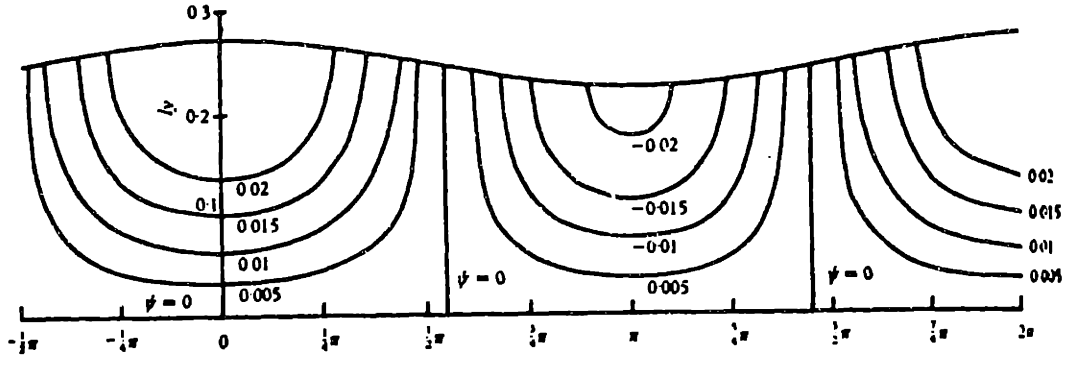

ANALYTICAL SOLUTION

FIGURE 8-2 Comparison of spectral element and analytical solutions of the steady-periodic velocity distribution for planar peristaltic Stokes flow.

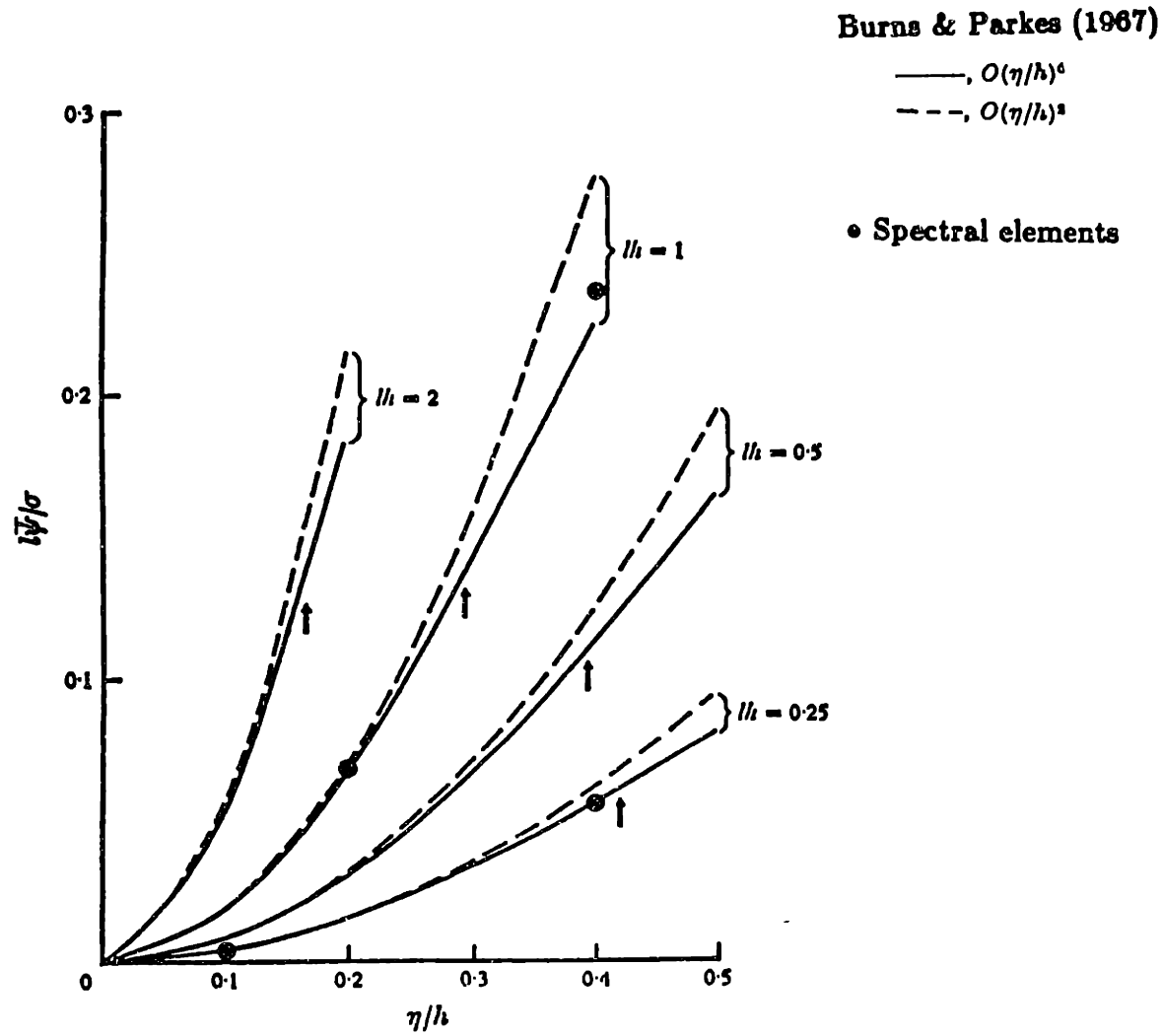

FIGURE 8-3 Comparison of spectral element and analytical solutions of the net flux per period for planar peristaltic Stokes flow.

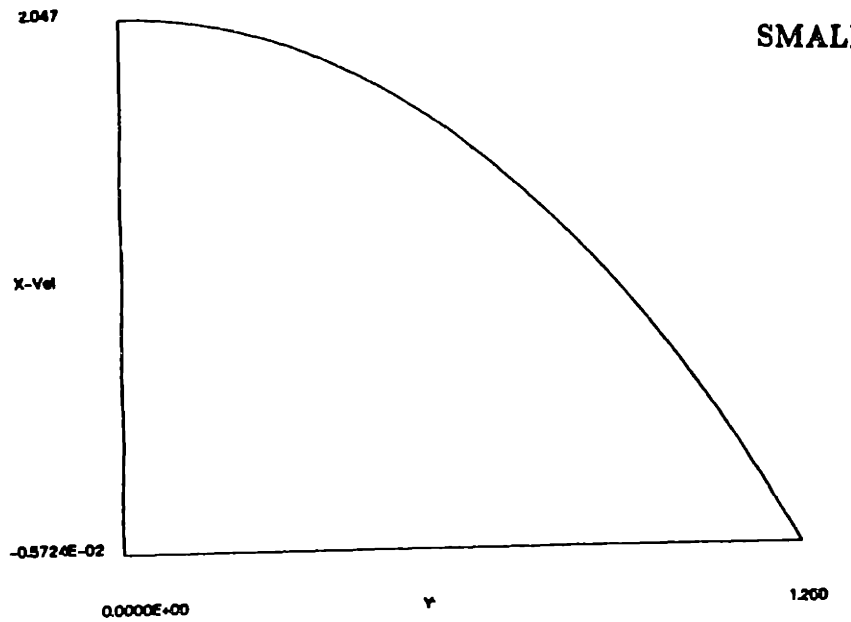

SMALL WOMERSELEY NUMBER

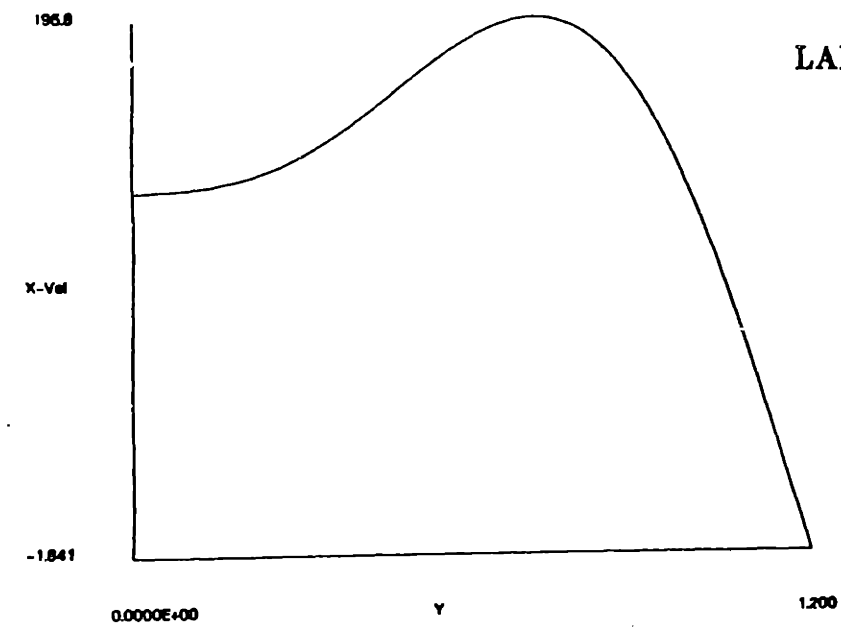

LARGE WOMERSELEY NUMBER

FIGURE 8-4 Comparison of streamwise velocity profiles at a typical section for small and large Womerseley numbers.

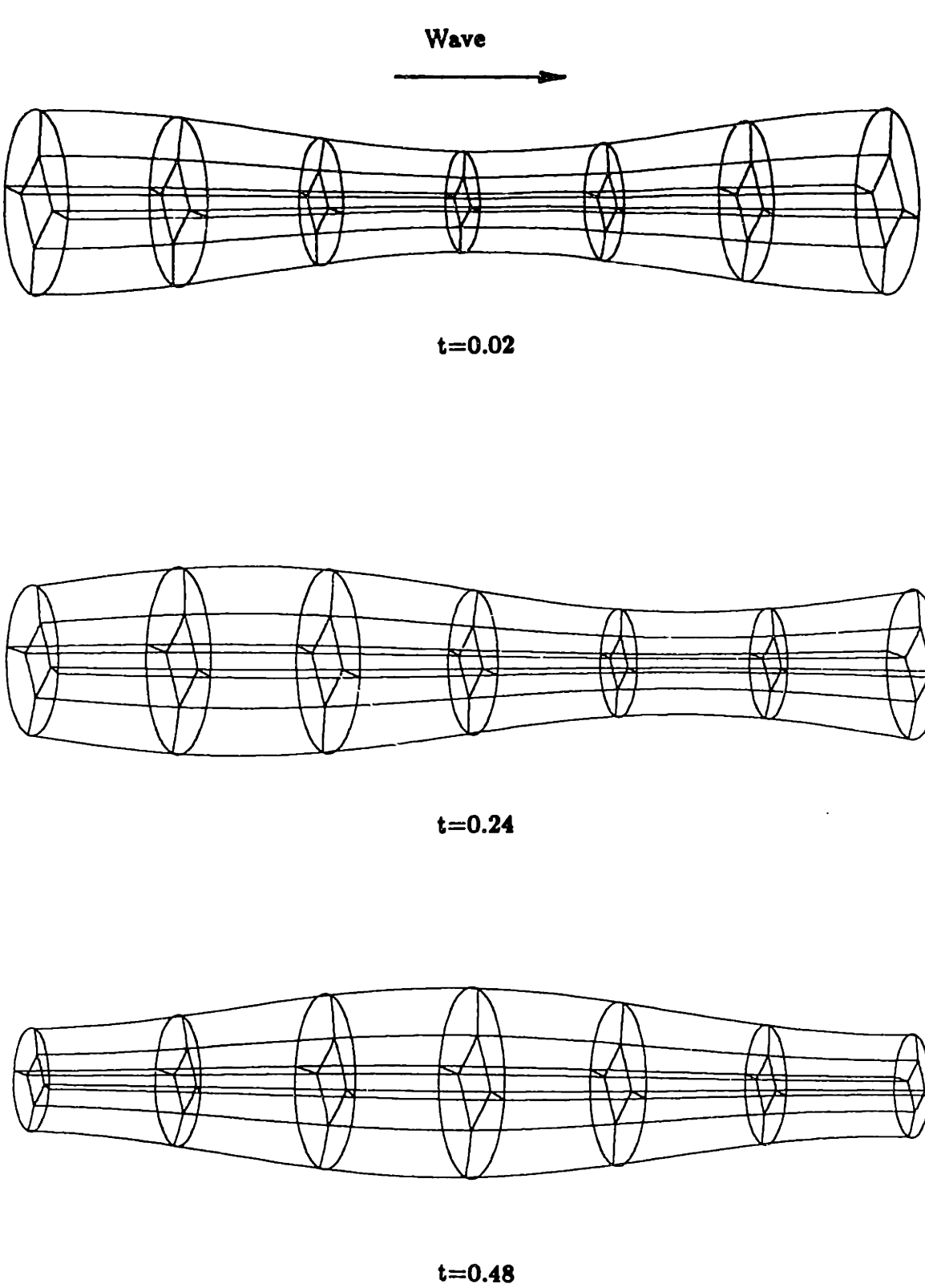

FIGURE 8-5 Spectral element solution of axisymmetric peristaltic Stokes flow : flow domain at three instants of time.

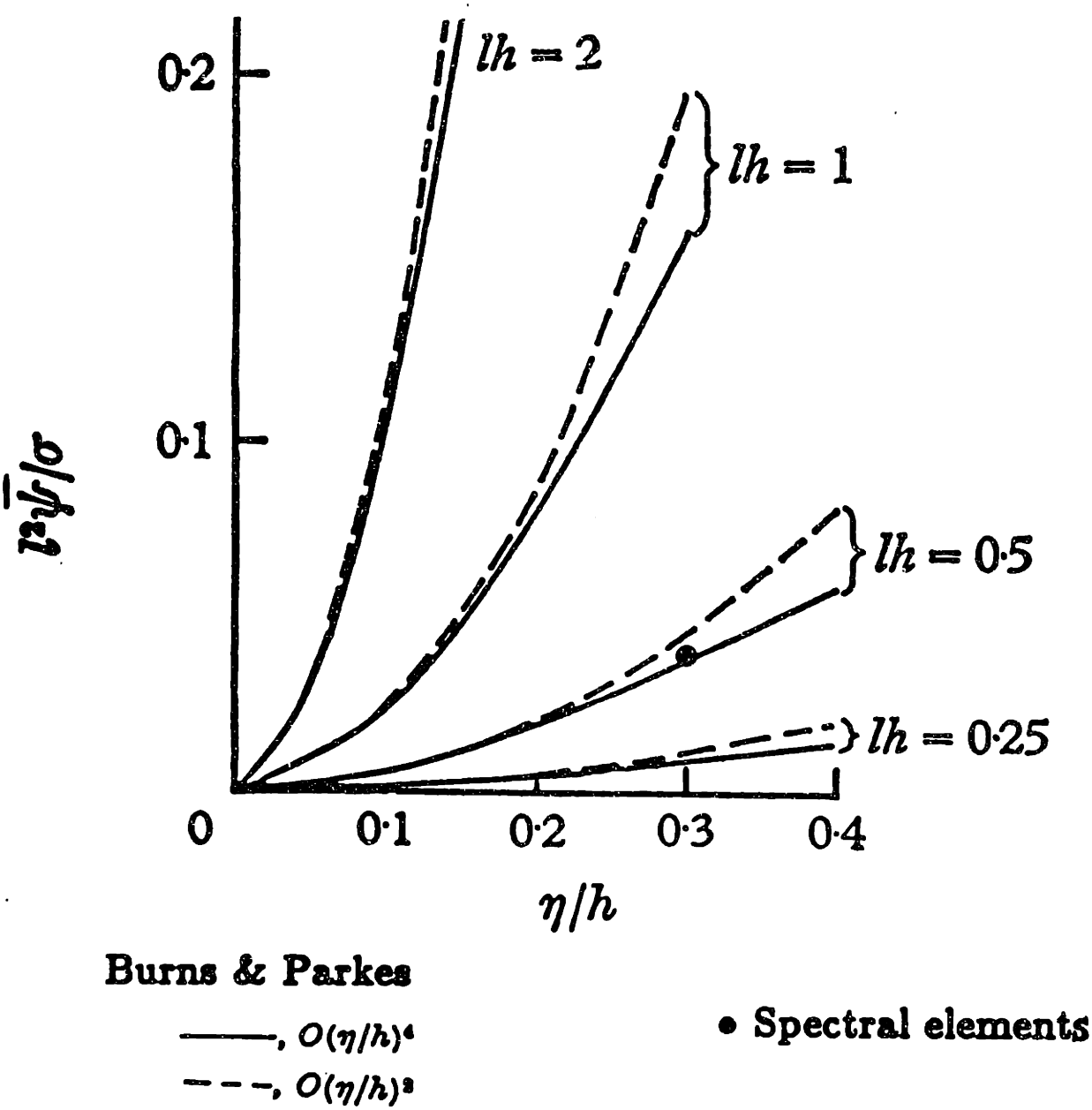

FIGURE 8-6 Comparison of spectral element and analytical solutions of the net flux per period for axisymmetric peristaltic Stokes flow.

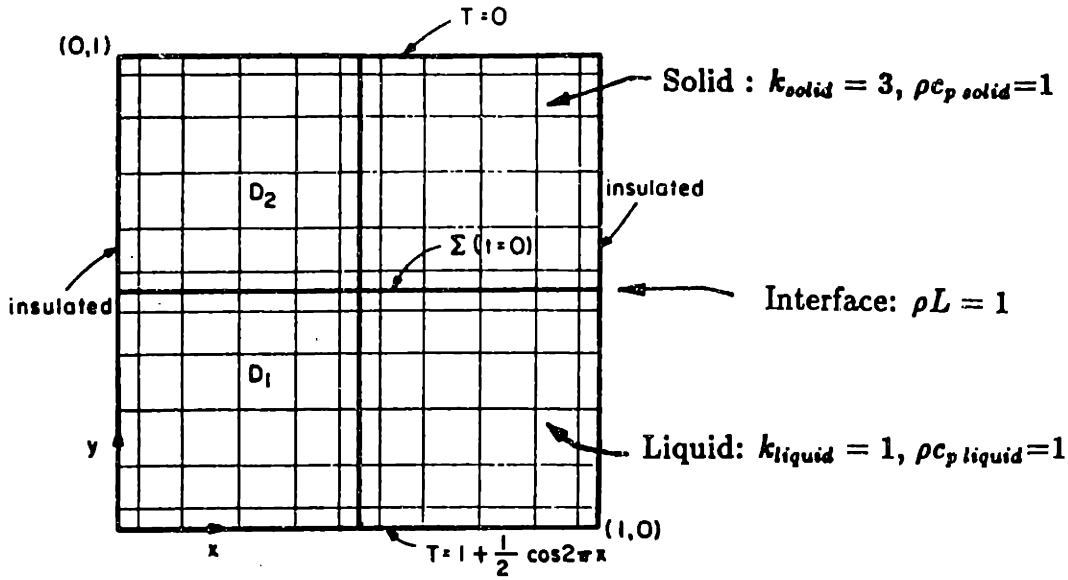

(a)

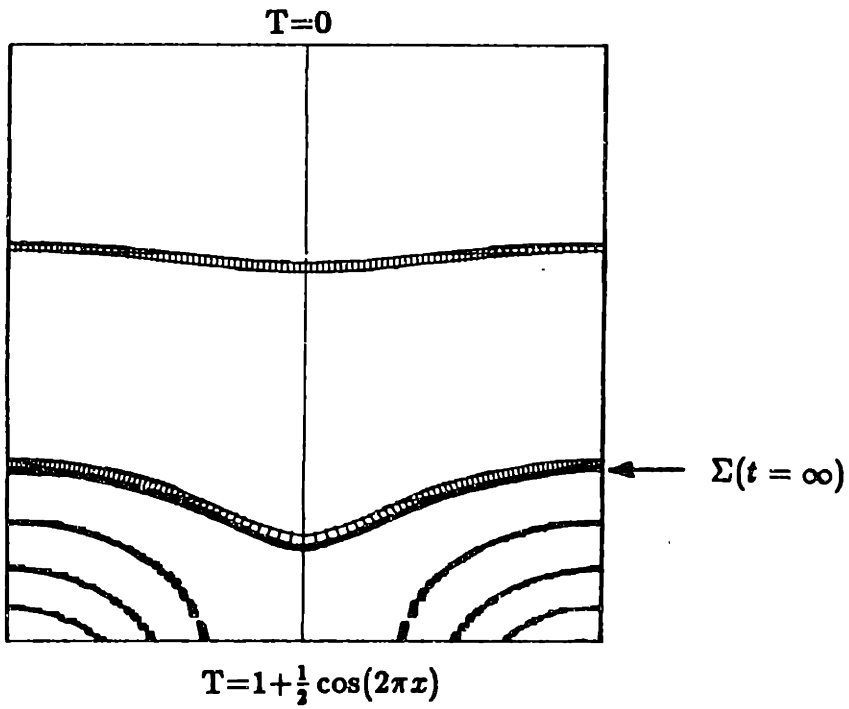

(b)

FIGURE 8-7 Analysis of a planar Stefan problem : (a) problem description; and (b) spectral element solution of temperature and position of solid-liquid interface at steady-state.